



ALADIN-HIRLAM Newsletter

No. 11, August 21st, 2018



Joint 29th ALADIN Workshop & HIR8LAM All Staff Meeting 2018
16-20/04/2018, Toulouse, France

CONTENT

Introduction	4
Editorial	5
Events announced for 2018(and later on)	7
Around the 28th ALADIN Wk & HIRLAM 2018 ASM	9
<ul style="list-style-type: none"> • Variational Constraints for Data Assimilation in ALADIN-NH Dynamics, Carlos Geijo, Pau Escribà 13 • VIEsion: Assimilation of Mode-S Data, Phillip Scheffknecht, Florian Meier, Christoph Wittmann, Lukas Strauss 27 • On the use of amateur weather observations in an operational nowcasting and NWP framework, Trygve Aspelien, Cristian Lussana, Thomas Nipen, Ivar Seierstad 31 • ALARO-1 Canonical Model Configuration Developments: shallow convection and surface roughness, Radmila Brožková, Ján Mašek 35 • A few thoughts about cloud reunification in Alaro, Luc Gerard 39 • Use of CAMS Aerosol Fields to Modify the Cloud Condensation Nuclei in HARMONIE-AROME, Daniel Martin-Perez 41 • Verification and Quality Assurance in HIRLAM-C 2018: - Status and Outlook - , Bent Hansen Sass 47 • AROME-SURFEX orographic parametrizations, Laura Rontu, Alexandre Mary, Clemens Wastl, Yann Seity 51 • Cycles, mitraille and the like ... , Claude Fischer 59 • Object Orientation in Post-processing, Ryad El Khatib 62 • CANARI model implementation using SYNOP for ALADIN Algeria ... Idir Dehmous, Mohand Ouali Ait Meziane 66 • Running AROME DUST 3km : Validation over new domain, Abdenour AMBAR, Mohamed MOKHTARI, Abdel Aziz KONSEIBO 73 • Verification of HARM-AROME model at 1.0 km over Spanish Harbour Areas, Inés Santos, Elena Padorno, José A. Ruíz, Isabel Martínez 77 • Visibility Prediction based on AROME Cy38t1 (2.5km) Outputs using Machine-Learning Regression, Driss BARI..... 88 • Background-error covariances for AROME-Morocco 3D-Var, Hdidou Fatima Zahra91 • IGB, the Upgrade to the Joint Operational HARMONIE by DMI and IMO in 2018, Xiaohua Yang et al93 	
Just graduated	97
	
Julie Berckmans.....	98
Jan Masek.....	101
ALADIN-HIRLAM Newsletters : previous issues	102

Introduction

Welcome to the combined 11th edition Newsletter of the HIRLAM and ALADIN consortia.

The “[28th ALADIN Workshop & HIRLAM All Staff Meeting 2018](#)” took place on 16-20 April 2018 in Toulouse (France).

This joint Wk/ASM obtained the label "[EuroScience Open Forum 2018 - TOULOUSE, EUROPEAN CITY OF SCIENCE](#) and the usual agenda was enriched with a beautiful public conference given by Laure Raynaud ([pdf of the presentation](#), [video of the presentation](#)), in French, title: "Vers une prévision des incertitudes en météorologie" [1]).

This summer 2018 edition is mainly dedicated to this “[28th ALADIN Workshop & HIRLAM All Staff Meeting 2018](#)”.

Therefore, we first like to thank all those that contributed to this Newsletter with their articles.

Please contact authors directly for any needed additional information on their article.

Please be also reminded that a full overview and all [presentations \(videos and pdf files\)](#) can be viewed from the ALADIN website.

Furthermore, a special focus is proposed on two [recent Doctors](#)

Last but not least, a [summary list of upcoming events, planned for the near future \(as from second semester 2018 and after\)](#) is available.

We hope you enjoy reading the eleventh ALADIN-HIRLAM Newsletter. Once again, thanks all authors for their contributions and hand it off first to the PMs for the Edito.

Patricia and Frank

Further consortia information needed?

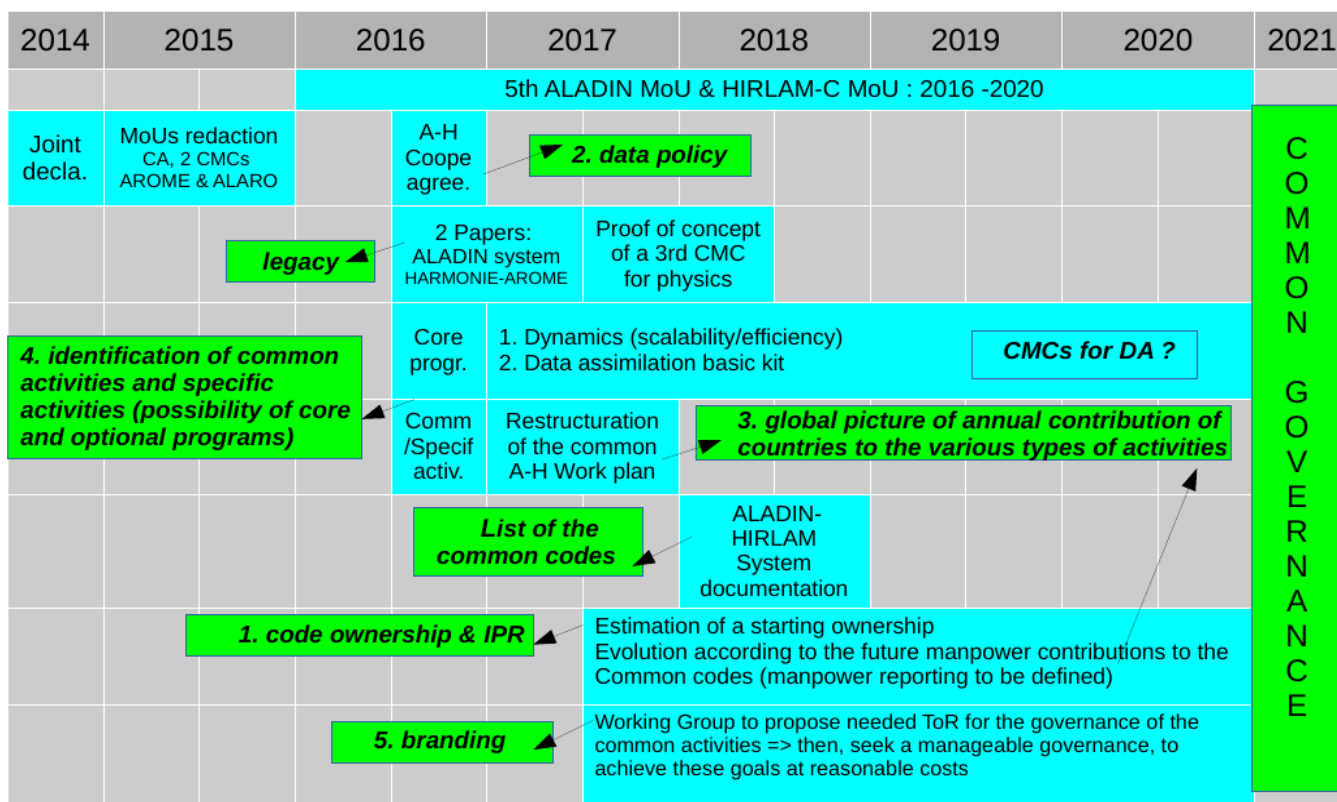
Please visit the [ALADIN](#) and [HIRLAM](#) websites or contact us.

Edito : The road towards a single consortium: the continuing story

[In their first joint meeting in December 2014, the ALADIN General Assembly and the HIRLAM Council made a joint declaration](#), proclaiming their ambition to aim towards achieving a single joint consortium by the end of the present MoU period (end 2020). The PM's were tasked to head towards this goal, and tackle five issues to be resolved:

1. Code ownership (software IPR)
2. Data policy
3. Global picture of annual contributions to the various types of activities
4. Identification of common activities and specific activities (incl the possibility of core and optional programs)
5. Branding

The analysis of these issues is being executed according to the roadmap steps below (as was already announced in the [Edito of NL9](#)).



Convergence roadmap : status in April 2018

The planned steps have been executed so far.

The challenging issue of [data policy \(2\)](#) was already addressed in the [ALADIN-HIRLAM Cooperation Agreement](#) (December 2016).

Canonical model configurations have been defined for Arome-France, ALARO and Harmonie-Arome, and papers have been published describing for the first time the Harmonie-Arome configuration (Bengtsson et al, 2017), together with its legacies from both ALADIN and HIRLAM, and the ALADIN system (Termonia et al., 2018, [see the Edito of NL10](#)). The code of all three CMC's now can be taken from the central code repository at Meteo-France.

A major step towards the identification of common and specific activities (4) was undertaken with the definition of a new process and [setup of the joint Rolling Work Plan in 2017](#). In this new setup, a much closer link was made between research activities and the common code expected to arise from them. Also, two strategic core programmes were formulated and kicked off, for the evolution of the dynamical core and for the introduction of a basic data assimilation configuration in all member services.

The new work plan for 2018 gave a first indication of the [planned annual contributions by all members to the common activities \(3\)](#) (that is, the activities contributing to the development and maintenance of the common code). These will need to be compared to actual contributions, which are monitored in a commonly agreed manner. In the first half of 2018, therefore, [a joint web-based monitoring system has been developed and agreed upon](#), and this new common way of monitoring activities is being introduced in all member services. [In the HMG-CSSI meeting following the 2018 Workshop/All Staff Meeting](#), the lessons learned in the process of constructing the work plan were reviewed, and a first brief assessment was made on the status of the planned work. It is intended that from the beginning of 2019 onwards, a more thorough comparison between the annual plans and their realization can be made on the basis of the new joint monitoring.

The next big step forward which is being prepared in 2018, is to achieve [agreement on a common mission and scope for the new joint consortium](#): what do we intend to achieve together, and what will be the range of activities that we will jointly engage in from 2021 onwards? A working group has been preparing a proposal for this, which, [after constructive comments from the joint HAC-PAC meeting in May in Dublin](#), has been distributed to all members for comments and suggestions. It is hoped that at the next joint Assembly-Council meeting, in November in Zagreb, a common view can be established on the mission and scope of the joint consortium. As a next step, the working group can then consider and prepare proposals for [an appropriate common governance for the single consortium](#). This is expected to be a main goal in the convergence process for 2019.

The PMs



Events announced for 2018 (and later on)

The Newsletters only give a static overview (twice a year) with upcoming meetings for the (near) future time frame. Actual information (year round) is available through the [ALADIN / HIRLAM](#) websites. You might find also events of interest through the [LACE](#) website.

1 **ALADIN/HIRLAM related meetings**

- [40th EWGLAM and 25th SRNWP meetings, 1-4 October 2018](#), Salzburg, Austria
- 7th joint HAC/PAC meeting, 22-23 October 2018, Prague, Czech Republic
- 4th joint ALADIN GA/HIRLAM Council, 19-20 November 2018, Zagreb, Croatia
- [Joint 29th ALADIN Wk/HIRLAM ASM 2019, will be hosted by AEMET in Madrid, 1-4 April 2019](#)
- [41th EWGLAM and 26th SRNWP meetings](#), end September – beginning October, Bulgaria (dates and exact location, t.b.c.)

2 **ALADIN/HIRLAM Working Weeks / Days**

Following topics through working weeks/days will be addressed:

- Data Assimilation algorithms
- Use of Observations : May, Spain
- Radiation, clouds, aerosols: March, at ECMWF
- Surface (related to modelling as well as DA)
- EPS, 19-23 November 2018, SMHI Norrköping
- HARP
- System, Dublin, late autumn 2018
- Hi-Res modelling
- Training/webinar for developers: to be scheduled in Jan/Febr. 2019

3 **Regular group video meetings**

Roger Randriamiampianina took the initiative to organize regular group video meetings (via google hangouts) for Data Assimilation staff (from both ALADIN and HIRLAM) and this was followed by Daniel Santos Munoz (for System and Scalability) and Patrick Samuelsson (for Surface). Outcome is noted as very valuable.

They will be happy to help if you plan to set up your own group video meeting.

4 About the past joint events

Please check the on-line information on the dedicated ALADIN webpages for past ALADIN-HIRLAM common events such as:

- [joint ALADIN Workshops & HIRLAM All Staff Meetings](#),
- [minutes of the HMG/CSSI meetings](#),
- [minutes of HAC/PAC meetings](#),
- [minutes and presentations fo the joint ALADIN General Assemblies and HIRLAM Councils](#)

During the first semester of 2018, besides the big Workshop/ASM (see the links and the articles in this Newsletter), the HMG and the CSSI met on April 20 in Toulouse and the HAC and PAC met on May 23 in Dublin. The minutes of these meetings have been validated and are on-line. (click on the photo below for direct access to the minutes).



© Christophe Ciais - Météo-France

HMG/CSSI meeting, Toulouse, 20 April 2017



HAC-PAC meeting, Dublin, 23 May 2018



28th ALADIN Wk & HIRLAM 2018

Hosted by Météo-France
April 16-20, 2018 in Toulouse



In the Agenda below, click on the title of a presentation to get access to the corresponding slides (pdf), or on the title of a poster.

“**article in this Newsletter**” indicates that there is a dedicated article in this newsletter around the presentation/poster.

Click on “**Video**” to get access to the video of the sessions (plenary sessions only).

1 [Agenda with link to the presentations \(videos and pdf files\)](#)

- Plenary opening session. [Video of the opening session](#)
- Opening of the Meeting & Welcome speech
 - Piet Termonia: [ALADIN status overview](#)
 - Jeanette Onvlee: [HIRLAM highlights of the past year](#)
 - Balazs Szintai: [Status of the EUMETNET C-SRNWP project](#)
- Plenary session 1: Data Assimilation. [Video of the data assimilation session \(first part\)](#)
 - Yann MICHEL: [The future EnVar scheme for the AROME model](#)
 - Roger RANDRIAMAMPINANINA: [Upper-air data assimilation in HIRLAM, status and plan](#)
 - Jelena BOJAROVA: [Flow-dependent data assimilation in HARMONIE forecasting system](#)
 - Wafa KHALFAOUI: [Impact of an improved background-error covariance matrix with an AROME 3DVAR system over Tunisia](#)
 - Carlos GEIJO: [Balancing Initial Conditions with Variational Constraints. First Results with 3D-Var and LETKF](#) **article in this Newsletter**
 - Jean-Francois MAHFOUF: [Ongoing developments on the use of observations in the AROME 3D-Var](#)
- Plenary session 1 (cont.): Data Assimilation. [Video of the data assimilation session \(second part\)](#)
 - Isabel MONTEIRO: [ASC2AT Assimilation Experiments with HARMONIE-AROME mesoscale model over Iberian Peninsula](#)
 - Sigurdur THORSTEINSSON: [Use of low peaking channels from AMSU-A and AMSU-B over ice](#)
 - Phillip SCHEFFKNECHT: [Assimilation of Mode-S Data for High Resolution Simulations](#) **article in this Newsletter**
 - Benedikt STRAJNAR: [Impact of Mode-S EHS observations in ALADIN](#)
 - Trygve ASPELIEN: [On the use of amateur weather observations in an operational nowcasting and NWP framework](#) **article in this Newsletter**
 - Xiaohua YANG: [C3S Copernicus Arctic Regional Reanalysis system](#)
- Plenary session 2: Physics. [Video of the physics session \(first part\)](#)
 - Yann SEITY: [Recent work on AROME physics](#)
 - Sander TIJM: [HARMONIE-AROME forecast model developments](#)
 - Radmila BROZKOVA, Neva PRISTOV: [ALARO-1 Canonical Model Configuration developments and tests](#) **article in this Newsletter**
 - Luc GERARD: [Reconnecting cloud representations in Alaro-1](#) **article in this Newsletter**
- Plenary session 2 (cont.): Physics. [Video of the physics session \(second part\)](#)
 - Eric BAZILE: [What can we learn from GABLS4 ?](#)
 - Benoit VIE: [Evaluation of the 2-moment scheme LIMA and recent developments](#)
 - Daniel MARTIN-PEREZ: [Modification of cloud condensation nuclei in HARMONIE-AROME microphysical parametrization using CAMS outputs](#) **article in this Newsletter**
 - Bjorg Jenny ENGDAHL: [Improved representation of supercooled liquid water in HARMONIE-AROME](#)
 - Kristian Pagh NIELSEN: [Testing the snow albedo sensitivity in HARMONIE-AROME](#)
- Plenary session 3: Dynamics. [Video of the dynamics session](#)
 - Petra SMOLIKOVA: [Dynamics in LACE](#)
 - Fabrice VOITUS: [Exploring some alternatives to improve the robustness of mass-based SI Spectral NH system](#)
 - Karim YESSAD: [An alternate way to treat Melmholtz equation in the NHEE model](#)
 - Daan DEGRAUWE: [The mass-based non-hydrostatic dynamics dwarf](#)
 - Martina TUDOR: [LBC files - make and use](#)

- WG on Climate
- Side meeting on surface physics and data assimilation
- Plenary session 4: Verification. [Video of the verification session \(first part\)](#)
 - Christoph ZINGERLE: [HARP Status and Plans](#)
 - Andrew SINGLETON: [The future for point verification in HARP](#)
 - Bent SASS: [HIRLAM-C activities on verification: Status and Plans](#) **article in this Newsletter**
 - Garcia-Moya JOSE A.: [Verification of hourly precipitation using OPERA dataset](#)
 - François BOUYSSSEL: [Preliminary results with upgraded horizontal resolution in ARPEGE](#)
- Plenary session 4 (cont.) : Verification. [Video of the verification session \(second part\)](#)
 - Angeles HERNANDEZ: [Simulated MSG SEVIRI imagery from the HARMONIE-AROME model](#)
 - Joel STEIN & Fabien STOOP: [New neighborhood-based contingency tables](#)
 - Ines SANTOS ATIENZA: [Assessment of HARM-AROME model at 1.0 km over the Spanish coast for wind forecast](#)
 - Danijel BELUSIC: [Large spatial spin-up at inflow boundaries in HCLIM-AROME](#)
 - Discussion (side-meeting announcement)
- Plenary session 5 : Surface. [Video of the surface session](#)
 - Patrick LE MOIGNE: [SURFEX](#)
 - Patrick SAMUELSSON: [Overview of HIRLAM surface activities](#)
 - Camille BIRMAN: [Meteo-France operational land surface analysis for NWP: current status and perspectives](#)
 - Ekaterina KURZENEVA: [Performance of FLake in HARMONIE](#)
 - Laura RONTU: [Status of subgrid-scale orography parametrizations ororad and orotur in HARMONIE-AROME](#) **article in this Newsletter**
 - Margarita CHOULGA: [Anthropogenic influence to continental land surface stocks and fluxes](#)
 - Patrick LE MOIGNE: [ECOCLIMAP Second Generation](#)
- Plenary session 6: EPS. [Video of the EPS session](#)
 - Inger-Lise FROGNER: [HarmonEPS developments](#)
 - Martin BELLUS: [LAM-EPS activities in LACE](#)
 - Yann MICHEL: [The AROME EDA: formulation and impact on the deterministic AROME 3DVar](#)
 - Yong WANG: [Seamless ensemble forecasting from minutes to days](#)
- Plenary session 7: System [Video of the system session](#)
 - Claude FISCHER: [Cycles, mitraille and the like](#) **article in this Newsletter**
 - Daniel SANTOS MUNOZ: [HARMONIE-AROME system progress and evolution](#)
 - Roel STAPPERS: [OOPS progress at ECMWF](#)
 - Ryad EL KHATIB: [Object orientation in post-processing](#) **article in this Newsletter**
- Plenary closing session. [Video of the closing session](#)
- Side meeting on HARP verification
- System side meeting

2 Posters

- Andrae Ulf : [MetCoOp activities](#)
- Azad Roohollah : [ALERTNESS project: Advanced models and weather prediction in the Arctic](#)
- Eric Bazile, Rachid Abida, Antoine Verrelle, Patrick Le Moigne, Cornel Soci, C. Szczypta: [A 55 year surface analysis over Europe at 5.5km within the UERRA project](#)
- Bojarova Jelena : Relevance of climatological background error statistics for meso-scale data assimilation

- Calvo Javier : [The NWP system at AEMET](#)
- Cedilnik Jure : [ALADIN in Slovenia - 2018](#)
- Clancy Colm : Operational NWP at Met Eireann
- Darcy Ronan : Operational NWP at Met Eireann
- Deckmyn Alex : [National poster Belgium](#)
- Derkova Maria : [ALADIN related activities @SHMU](#)
- Dumitru Alina : [ALADIN Activities in Romania](#)
- Feddersen Henrik : [COMEPS - DMI's short-range ensemble prediction system](#)
- Gleeson Emily : [Radiation Experiments using the ALADIN-HIRLAM System](#)
- Gleeson Emily : [Met Eireann's high resolution experiments](#)
- Guser Alper : [Aladin Related Activities at TSMS](#)
- Hdidou Fatima Zahra : [Moroccan National poster](#) **article in this Newsletter**
- Hdidou Fatima Zahra : [GPS data assimilation in Morocco](#) **article in this Newsletter**
- Horvath Kristian : [Using spectral evaluation to assess the added value of higher resolution modelling](#)
- Imrisek Martin : [Data assimilation activities at SHMU](#)
- Kolonko Marcin : [Aladin in Poland](#)
- Korpinen Annina : [Simulated effects of land-sea contrasts in Southern Finland](#)
- Kovacic Tomislav : [Radar data assimilation in Croatia](#)
- Martínez-Sánchez Mauricia : [AEMET-gammaSREPS: current operational status](#)
- Medeiros Paulo : New Developments in OBSMON
- Monteiro Maria : [ALADIN - Portuguese Technical and Scientific Activities](#)
- Odak Plenkovic Iris : [Deterministic post-processing of ALADIN NWP in Croatia](#)
- Pottier Patricia : [NMW systems at Meteo-France](#)
- Randriamampianina Roger : Radar for Improving Precipitation Estimates and Optimization of Hydropower Energy Production (RadPrO)
- Ricard Didier : Impact of turbulence representation on deep convection
- Santos Atienza Ines : [Verification of HARM-AROME model at 1.0 km over Spanish harbour areas](#) **article in this Newsletter**
- Szucs Mihaly : [NWP at the Hungarian Meteorological Service](#)
- Trojakova Alena : NWP activities at CHMI
- Tsenova Boryana : Status of NWP in Bulgaria
- Tudor Martina : [Operational forecast using ALADIN System in Croatia in Spring 2018](#)
- Valkonen Teresa : [Physiographic data sets in AROME-Arctic](#)
- Wafa Khalifaoui : NWP Activities in Tunisia
- Whelan Eoin : [SAPP: Evaluation for Operational NWP](#)
- Wittmann Christoph : NWP related activities in Austria

3 Working groups, side-meetings, LTM meeting, HMG/CSSI meeting, ...

More information on the 28th Wk&ASM 2018 ([agenda](#) and [participants](#), photos) and the side events (WG discussions, LTM meeting, HMG/CSSI meeting) are available on [the dedicated page on the ALADIN website](#).

Variational Constraints for Data Assimilation in ALADIN-NH Dynamics

Carlos Geijo, Pau Escribà, Spanish Meteorological Agency (AEMET)

1 Introduction

Balances among analysed meteorological variables in the data assimilation process can be effectively introduced by means of the well-known method of variational constraints (VC) [1], [2], [3]. In the case of the ALADIN-NH dynamics, its semi-implicit linear system for the non-hydrostatic fully compressible Euler equations (SI) appears as a convenient way of giving a precise definition to these constraints. This approach is non-statistical and in principle flow-dependent. Non-isotropic and non-homogeneous aspects in the analysis increments cannot however be fully introduced by these constraints because SI deals only with rotation invariants and the base-state used in its formulation is one at rest and on a flat orography. The spatial structure in the analysis will then come only from the spatial structure of the observation increments forcing. In this respect, the situation is similar to the current ALADIN 3D-Var algorithm [4], although now these restrictions stem not from assumptions on the statistical properties of the model error fields, but from the definition of the SI itself. A new interesting feature of this method is the integration in the analysis algorithm of the vertical velocity field, which clearly must be important in convection permitting NWP. Another main point is that SI is a time-step forward operator, and this property gives to this algorithm a nudging-like functionality making it well suited for DA continuous-in-time, also an indispensable feature for NWP of intrinsically short-time predictability weather.

SI can be solved using Greens functions (GF) [5]. Because of the assumptions behind its formulation, SI can be reduced to an ODE boundary value problem whose GF is easy to calculate and permits the solution to be found by quadratures. This GF algorithm has the appealing feature of doing the mathematics very transparent (in particular the treatment of upper and lower boundary conditions), avoids staggering along the vertical and also goes around the problem of the algebraic constraints among discrete local and non-local operators. In this work this GF method is pursued further and it is shown that the analysis with variational constraints can be found by a similar numerical algorithm, although now involving GFs for higher order operators.

VC has been tested in three different contexts. First it is applied to increments obtained from the alignment of radial wind HARMONIE-AROME fields with Doppler radar pseudo-images employing a position error correction algorithm known as Field Alignment (FA) [6]. This FA is a fully flow-dependent algorithm, but it introduces imbalances which have a detrimental impact in subsequent forecasts. VC can effectively reduce these imbalances. The VC method was conceived with this first application in mind, in the scope of the development of new NWP tools for Now-Casting (NWP-NWC). Second, it is applied to LETKF analysis [7] generated from a small ensemble. The lack of overlap in observations used by the analysis in neighbouring points causes discontinuities in the analysed fields that VC can filter according to the dynamics described by SI. Third, a comparison between VC and the statistical balances implemented in the current 3D-Var algorithm [8] was conducted in order to get a first estimate of the impact of this new approach, in particular of including in the initialization the vertical wind.

2 Variational Constraints for ALADIN-NH Dynamics

In the spirit of the GF algorithm, we will consider the minimization of a functional J on functions of a given degree of smoothness in the vertical coordinate ξ and see whether or not the problem can be solved in this framework. Let as usual J consist of an observation forcing term and a constraint, weighted by w_o and w_c respectively:

$$2J(x^k) = \int_0^{\xi} w_o^k \|x^k - x_o^k\|^2 + w_c^k \|Mx^k - x_\bullet^k\|^2 \quad Eq 2.1$$

where the upper index k indicates that the problem is stated in wavenumber space. The module bars $\|\cdot\|$ come in because the x 's are complex numbers. M stands here for the SI system, it encodes the set of constraints and is a real operator, what makes the introduction of these complex module bars unnecessary after all (M does not mix real and imaginary parts of x_k). This conclusion is apparent from simple inspection of Eq2.1, but in case of non correspondence between model and obs spaces (i.e. when an obs operator is necessary) it takes some algebra to conclude that it is also possible to dispense with the complex module bar notation (see [9]). The symbol “ \bullet ” is introduced to keep in mind a subtle difference with the similarly looking 3D-Var cost function, where one would write x_b instead of x_\bullet . M is a time-step advancing operator, x_\bullet and x_b correspond then to model states at different times (differing by one time step). In principle the weights w_o and/or w_c could vary along the ξ coordinate, but this would complicate the calculation of the GF used by the numerical method that it is wanted to show in this paper. Therefore it is not considered here. Also these weights could take different values for different wavenumbers, this does not really complicate things, but at this stage it is considered a refinement of secondary importance. Therefore the weights w_o and w_c are just two real numbers and their ratio ($w = w_o/w_c$) is the only free parameter in the scheme.

One first obstacle in the calculation proposed in Eq2.1, is the determination of x_o^k . The problem arises because the observation fields will unavoidably be irregularly distributed in space and display void areas. To go around this difficulty let us restrict to an incremental formulation of the problem, that is, search for a solution in the vicinity of the background x_b

$$x^k = x_b^k + \Delta x^k \quad ; \quad x^k - x_o^k = -d^k + \Delta x^k \quad ; \quad d^k = x_o^k - x_b^k \quad ; \quad Mx^k - x_\bullet^k = M\Delta x^k \quad Eq 2.2$$

the last equation follows because the background is, of course, balanced. The difference field d does not have holes and it can readily be DFT transformed back and forth. Dropping the k upper index, Eq2.1 becomes:

$$2J(\Delta x) = \int_0^{\xi} w (\Delta x - d)^2 + (M \Delta x)^2 \quad Eq2.3$$

The condition that the increments Δx are balanced is seen to translate into the condition that they belong to the kernel of M , but in this weak-constraint approach, this condition will only be approximately satisfied. Take now functional variations of J (δJ) and disregard the boundary terms that results in the calculation. This can be done because we leave the values of Δx and $\partial \Delta x$ at the top and bottom boundaries out of the data assimilation problem, they will not be considered as control variables, that is, take $\delta \Delta x = \delta(\partial \Delta x) = 0$ on the boundaries (which does not mean that $\Delta x = \partial \Delta x = 0$ there necessarily, they can be given other values if non-homogeneous BC are specified, see below). Equating to zero the first variation gives

$$M^+ M \Delta x + w \Delta x = w d \quad w \equiv \frac{w_o}{w_c} \quad Eq 2.4$$

where M^+ is the adjoint of M with regard to the inner product used in the definition of J . It turns out that this problem can be reduced to an ODE boundary value problem which can be solved with homogeneous or non-homogeneous boundary conditions (BC) on Δx by means of the corresponding GF (see [9] for a detailed derivation of this result).

2.1 Formulation of the Balances

The SI system consists of set of linear equations with local and non-local vertical operators. The non-local operators arise because it is written in a mass-based vertical coordinate [12]. By decoupling the different horizontal wavenumbers, it becomes a very efficient time-stepping algorithm. Different formulations of it have been considered depending on the choice of prognostics. These formulations are all consistent within the linear approximation of the so-called “state equation” and geopotential equation (i.e. they can be transformed into each other by using Eq2.6 below). It is very convenient to go to non-dimensional variables by using the scales for T , π_s and the time-step Δt , and also to use a “depth ξ ” coordinate (runs downwards from 0 to ξ_s , see [5],[9] for all details). The choice in this work is the GEO-GW formulation, which after time discretization and before vertical discretization reads

$$\begin{aligned}
 D - K^2 (T + (\partial+1)\Psi) &= D^\bullet & K^2 &= (kH)^2 \omega_b^2 & \omega_b^2 &= \frac{g \Delta t^2}{H} = \frac{g^2 \Delta t^2}{RT^*} & ; & D = D' \Delta t \\
 gw - \omega_e^2 ((\partial+1)T + (\partial+1)\partial\Psi) &= gw^\bullet & \omega_e^2 &= \frac{g^2 \Delta t^2}{RT_e^*} & gw &= gw' \Delta t / RT_e^* \\
 T + \frac{R}{c_v} (D - \chi \partial gw) &= T^\bullet & T &= T' / T^* & \chi &= \frac{T_e^*}{T^*} & & Eq\ 2.5 \\
 \pi_s + N[D] &= \pi_s^\bullet & \pi_s &= \frac{\pi_s'}{\pi_s^*} \\
 \Psi - \chi gw + S[D] &= \Psi^\bullet & \Psi &= (\Phi_s + \Phi') / RT^* + \pi' / \pi^*
 \end{aligned}$$

The time step Δt includes numerical factors that depend on the choice of the time discretization scheme. The primed variables denote the perturbation (i.e. departure from base-state). For the wind (D and gw) they actually are the full variable as the base-state is at rest. The differentiation and integration operators are ∂ , $S[]$ and $N[]=S[]$ ($\xi=\xi_s$). In this notation, the state equation and geopotential equation read ([9])

$$PD = \partial\Psi + T = \partial\Phi + \partial\pi + T; \quad \Phi(\xi) - \Phi(\xi_s) = -G[\partial\Phi] = -G[PD] + G[T] + \pi_s - \pi \quad Eq2.6$$

With PD the pressure departure ($PD = \ln(p/\pi)$, p =total pressure, π =“hydrostatic pressure”) and $G[]$ another integration operator. In Eq2.5 two different T scales are employed, and their ratio is denoted as χ . This duplicity of T scales is considered here because it has been reported that it has impact on the stability of the vertical finite differences (FD) numeric scheme [10]. In fact, $\chi=1/5$ in the FD solver implemented in the HARMONIE-AROME system and used for this work.

As mentioned in the introduction, Eq2.5 can be reduced to an ODE boundary value problem. A vertical discretization based on splines is used for this purpose [5]

$$\begin{aligned}
 (-\lambda + \partial(\partial+1))[\chi gw] &= -\frac{(1+K^2\gamma)}{\omega_e^2 \chi \gamma} \chi gw^\bullet + \left(\frac{R}{c_p} + \partial\right) D^\bullet - \frac{1}{\gamma} (\partial+1+K^2) T^\bullet - \left(\frac{1}{\gamma} \partial - \frac{R}{c_p} K^2\right) (\partial+1) \Psi^\bullet \\
 (1+K^2\gamma) D - K^2 (1+\gamma\partial) \chi gw &= D^\bullet + K^2 ((\partial+1)\Psi^\bullet + T^\bullet) \\
 T + \frac{R}{c_v} (D - \chi \partial gw) &= T^\bullet & \lambda &= \frac{1+K^2\gamma(1+\omega_e^2\chi R/c_p)}{\omega_e^2 \chi \gamma} & Eq2.7 \\
 \pi_s + N[D] &= \pi_s^\bullet \\
 \Psi - \chi gw + S[D] &= \Psi^\bullet & (*) & \omega_e^2 \chi = \omega_b^2
 \end{aligned}$$

This re-arrangement of the equations can be referred to as $M[x_b + \Delta x]$ in Eq2.3 notation. It needs to be complemented with BC on Δgw (or perhaps on $\partial\Delta gw$ or both) at $\xi=0$ and $\xi=\xi_s$. It is interesting to see that, because of the relation indicated in Eq2.7 as (*), the double T -scaling has no effect on the free-mode unbounded spectrum of M , obtained by setting $M[x]=0$ with periodic BC (e.g. $gw(0)=gw(\xi_s)=0$).

2.2 A Numerical Solution to VC using GF

Eq2.7 shows a set of five constraints that are implied in SI. Of the five prognostics (gw, D, T, π_s , Ψ), the last one Ψ will hardly ever be accessible to observations. As the equation of state Eq2.6 shows, it is closely connected to PD, a variable that is defined by a rather arbitrary partition of the total true pressure p. As in addition to this it also happens that leaving this Ψ -constraint out of the common treatment of the other four greatly simplifies the mathematics of the problem, we will consider just the set of the first four (vertical velocity, horizontal divergence, T-compressibility and surface pressure tendency). With $\chi=1$ we can write for M and its adjoint M^+

$$M = \begin{bmatrix} L & 0 & 0 & 0 \\ -K^2(1+\gamma\partial) & (1+K^2\gamma) & 0 & 0 \\ -\beta\partial & \beta & 1 & 0 \\ 0 & N[] & 0 & 1 \end{bmatrix} \quad M^+ = \begin{bmatrix} L^+ & -K^2(1-\gamma\partial) & \beta\partial & 0 \\ 0 & (1+K^2\gamma) & \beta & N^+[] \\ 0 & 0 & 1 & 0 \\ 0 & 0 & 0 & 1 \end{bmatrix} \quad Eq2.8$$

where $\beta=R/c_v$, $\gamma=c_p/c_v$, K^2 defined in Eq2.5 and

$$S[X] = e^{-\xi} \int_0^{\bar{\xi}} e^z X \quad S^+[X] = e^{\xi} \int_{\xi}^{\bar{\xi}} e^{-z} X \quad N[X] = e^{-\xi} \int_0^{\bar{\xi}} e^z X \quad N^+[X] = e^{\xi-\bar{\xi}} \int_0^{\bar{\xi}} X \\ L[X] = (\partial^2 + \partial - \lambda)X \quad L^+[X] = (\partial^2 - \partial - \lambda)X + BT_L \quad \partial[X] = \partial X \quad \partial^+[X] = -\partial X + BT_o \quad Eq 2.9$$

with BT meaning “boundary term”. As explained above, the BT vanish because the BC are not considered control variables. The adjoints of the integral operators can be found by application of the defining property of adjoints (i.e. $\langle O^+X, Y \rangle = \langle X, OY \rangle$). At difference to the local operators L or ∂ , these non-local operators do not give boundary terms (see [9] for all details).

With these ingredients, it happens that Eq2.4 leads to another ODE boundary value problem as it happened for M (Eq2.7). However, now the operator involved is of 4th order instead of 2nd order

$$\hat{O}_\xi [\Delta gw] = F_{gw}^o(\xi) + F_D^o(\xi) + F_T^o(\xi) + F_{\pi_s}^o(\xi) (d_{\pi_s} + N[\Delta D]) \quad Eq2.10$$

The F^o 's on the r.h.s denote functions of the differences between observations and background for the corresponding variable ($d = x_o - x_b$), which are functions of ξ . They also depend on the relative weights “w” between obs forcing terms and constraints. It is possible to keep the possibility of these weights being different for each constraint

$$F_{gw}^o(\xi) = w_{gw} d_{gw}(\xi) \quad ; \quad F_D^o(\xi) = \frac{1}{X} (F_k K^2 (1-\gamma\partial) - \beta^2 \omega_T \partial) [w_D d_D(\xi)] \quad Eq2.11 \\ F_T^o(\xi) = -\frac{\beta}{X} ((F_k + w_D) \partial + F_k K^2) [w_T d_T(\xi)] \quad ; \quad F_k = 1 + \gamma K^2 \quad X = F_k^2 + w_D + \omega_T \beta^2 \\ F_{\pi_s}^o(\xi) = \frac{1}{X} (F_k K^2 \beta + \omega_T \beta^2) \omega_\pi e^{\xi-\bar{\xi}} \quad ; \quad \omega_i = \frac{w_i}{1+w_i} \quad i = gw, D, T, \pi_s$$

and the 4th operator for which we have to find the GF is (λ is defined in Eq2.7)

$$\widehat{O}_\xi = \partial^4 - a \partial^2 + b \quad ; a = (2\lambda + 1) + \frac{1}{X} (K^4 \gamma^2 w_D + (1 + w_D) \omega_T \beta^2) \quad ; b = w_{gw} + \lambda^2 + \frac{1}{X} (\omega_T \beta^2 + w_D) K^4 \quad Eq2.12$$

and as boundary conditions for the analysis increments Δgw we choose (non-homogeneous BC can also be incorporated if wanted).

$$\Delta gw(0) = \Delta gw(\underline{\xi}) = \partial \Delta gw(0) = \partial \Delta gw(\underline{\xi}) = 0 \quad ; \quad Eq2.13$$

The last term on the r.h.s of Eq2.10 is the obs forcing due to surface pressure increments. It shows up as proportional to a quantity $N[\Delta D]$ that at the time of performing quadratures with O_ξ^{-1} (i.e. GF) is still unknown. However, this unknown is not a function of ξ , is just a number, and the quadratures can be carried out without more trouble giving us back a solution parametrized by this quantity $N[\Delta D]$.

$$\Delta gw(\xi) = P(\xi) + Q(\xi) (F_{\pi_s} + N[\Delta D]); \quad P(\xi) = \sum_{i=1}^3 \int_0^{\xi_i} \widehat{O}^{-1}(\xi, z) F_i^o(z) \quad , \quad Q(\xi) = \int_0^{\xi_1} \widehat{O}^{-1}(\xi, z) F_{\pi_s}^o(z) \quad Eq2.14$$

This remaining d.o.f is fixed by performing the calculation $N[]$ on the second constraint with the solution found as in Eq2.14. How to do this accurately is also shown in [9]. It is then straightforward to substitute back in the rest of the constraints and so obtain finally the complete VC solution.

Eq2.11 shows that the analysed vertical velocity field (and therefore all the other analysed fields) is given by the ob - fg increments low-pass and high-pass filtered (K^2 dependency of the coefficients). These filters are not defined at will (aside from the values arbitrarily given to the weights “w”), but determined by SI. The vertical structure of the ob - fg increments (∂ dependency of the coefficients) also enters in the determination of the analysis. Horizontal and vertical structure of the analysis are then intertwined as dictated by SI.

The determination of the GF for the problem Eq2.12, Eq2.13 is one key element in this scheme. The high amount of symmetry in the problem (only even powers of ∂ , constant coefficients and hermiticity) makes it an accessible one, and makes also the whole scheme practical. The solution is worked out in [9]. Some examples of the GF kernels are shown in figure 1.

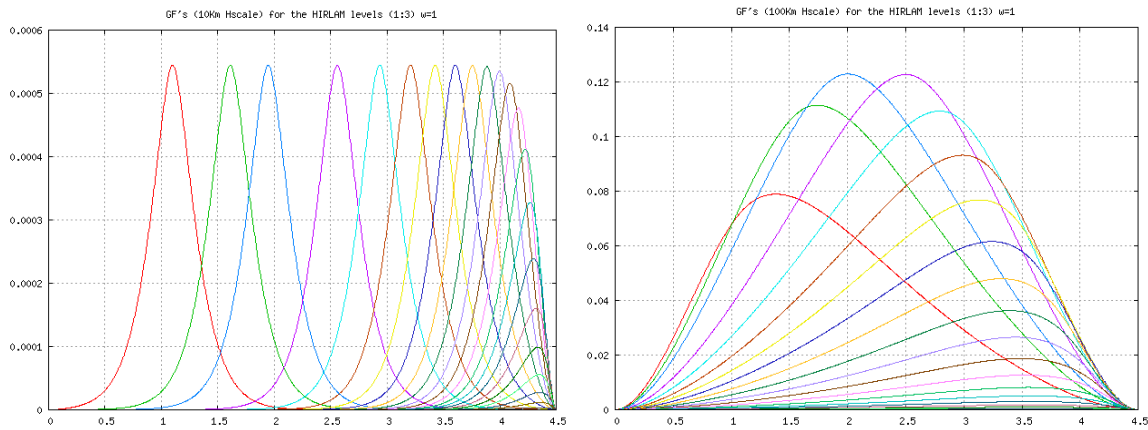


Figure 1 Aspect of the GF kernels for the problem Eq2.12, Eq2.13 corresponding to horizontal scales of 10 km (left) and 100km (right) with $w=1$ and HIRLAM 65-levels (only 1,3,5,etc... shown). The x-axis runs top-down (left-right) along the ξ coordinate. The max value ξ (about 4.5) corresponds to SI parameters $T^*=270K$, $\chi=1$ and $\pi_s^*=1000hPa$. These kernels are positive, show vertical spread dependent on the horizontal scale and they are also symmetric in the sense that $GF(x,y)=GF(y,x)$. This last property cannot be captured in this 1-D plot, where the dependency on the first argument of the GF that corresponds to the HIRLAM level is not displayed.

The different properties of the GF kernels described in the caption of Figure 1 are also those of a covariance matrix. In fact, it is not difficult to establish analogies between this scheme and the standard 3D-Var that clearly suggest that it is possible to think of the GF as a covariance function for the vertical velocity [9].

3 Tests of the Variational Constraints Method

3.1 Tests with Synthetic Observations

Two HARMONIE-AROME runs are prepared for a period of two days (2013/12/05-06) over a domain 800x800xL65 at nominal horizontal resolution of 2.5 Km. The runs setup are identical (defaults v40h1.1) except for the use of boundary conditions. The reference run or “truth” employs ECMWF analysis (“analysis_only” strategy), while the experiment is nested to closest in time ECMWF forecasts (“simulate_operational” strategy). The reference cycles every 6 hours (coincident with availability of ECMWF analyses), and generates forecasts every hour up to six hours, just what is necessary to carry over information from one cycle to the next, while the experiment operates in a similar configuration but with a shorter 1 hour cycle. No data assimilation is done for any run. For the run acting as truth, we pick up the +3H forecast from cycle 2013/12/05 12 UTC (12 hours after beginning of the experiment), and extract a cube 100x100xL[15-55] situated about the (400,400) point. Fields of wind, vertical divergence, temperature, surface pressure and pressure departure are read off the FA file and compared with their counterparts for the 2013/12/05 14 UTC +1H experiment forecast. The differences (ref-exp) provide the experimenter with “d-fields” ($x_o - x_b$) for horizontal divergence, vertical wind, temperature, surface pressure and pressure departure. We can now make use of these fields to study the congruence between analysed increments by the VC method and “true” increments. For instance, we can compare analysed and “ref-exp” vertical wind increments if we input horizontal divergence “ref-exp” increments to the VC algorithm. In other words, to what extent VC is able to reconstruct vertical motions from horizontal divergence information? Other similar tests can be carried out.

The tests are satisfactory albeit some mismatch in magnitude is found. For instance, Figure 2 shows that the analysed vertical velocity increments (contours) are in good agreement with those expected (shaded) when synthetic HD observations are utilised (i.e. in Eq2.10 notation $F^o_{gw} = F^o_T = F^o_\pi = 0$, $F^o_{HD} = (\text{ref-exp})$). The plot on the left is for $w=1$ and that on the right $w=10$. The bigger the value of w , the tighter the fit to obs as expected. However, the plot on the left also indicates that the analysed w fields come out about one order of magnitude smaller than expected. Due to linearity, it is not difficult to introduce an overall scale in the scheme that achieves an impressive match between actual and expected results (plot on the right includes this scale correction). However, this “fine-tuning” resource might not give in practice better verification scores (preliminary results in fact point in this direction). The method should be able to “nudge” towards the right magnitude by frequent updates. One question naturally arises here, is this disparity due to the rather different numerics employed in the VC analysis and in the forecast?

Figure 3 shows on the left the correspondence between horizontal divergence and vertical divergence for analysed fields. On the right, the counterpart for the reference is displayed. This reference is obtained by plotting the VD and HD fields from a +3H forecast. The almost exact out-of-phase relation between these two fields is striking. The analysed fields clearly keep this balance!

Figure 4 illustrates which is the situation for pressure departure PD. This field is analysed from the vertical momentum equation and indeed there is a clear connection between PD and vertical velocity W . However, again a mismatch in magnitude between analysed PD increments and those expected (shaded) is apparent. The mismatch is about one order of magnitude, analysed fields now bigger than

reference. Also the analysed PD lacks some fine scale features. This may be due to how the vertical momentum equation is integrated. Again, also the different numerics employed may be responsible for this mismatch.

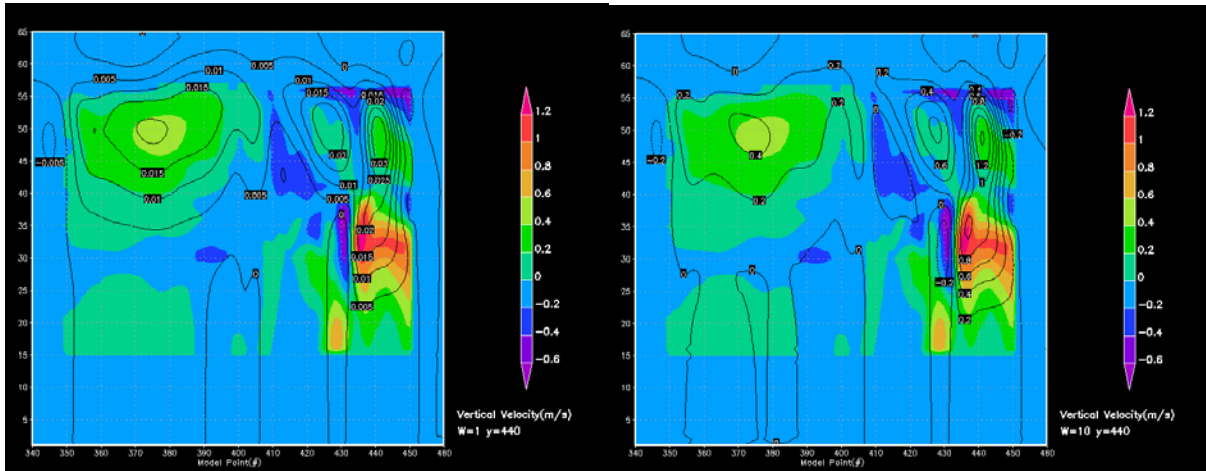


Figure 2 Analysed vertical velocity W from horizontal divergence data HD by means of VC . Left $w=1$, contours are about 10^{-1} smaller than shaded values (colour scale on plot). Right $w=10$, contours capture more structure from the shaded field. The plot on the right includes an overall scale correction which makes agreement between “exp” and “ref” truly remarkable.

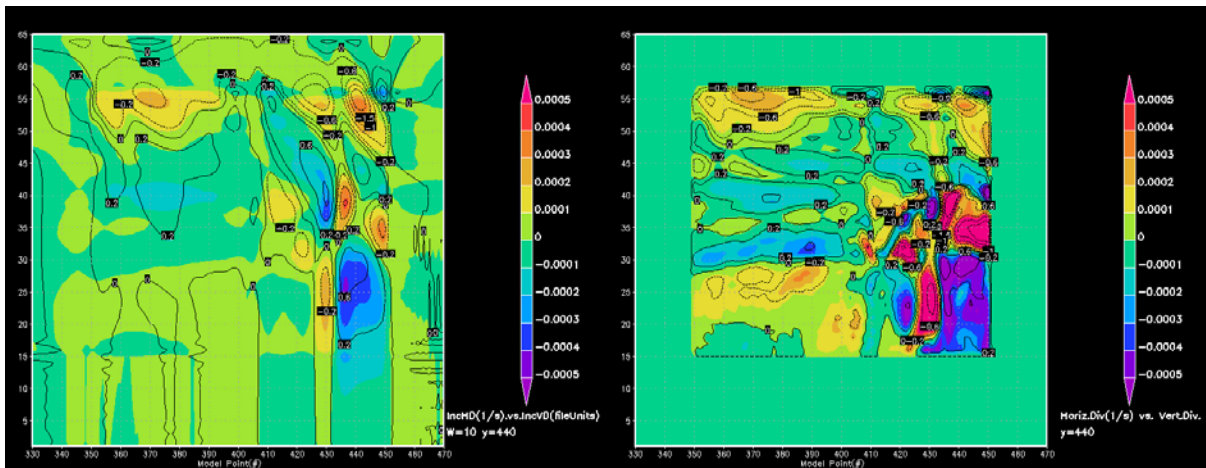


Figure 3 Analysed fields of VD and HD (left) keep the out-of-phase relation that these fields have in mature forecasts (right). Shaded is for HD and contour for VD in both plots.

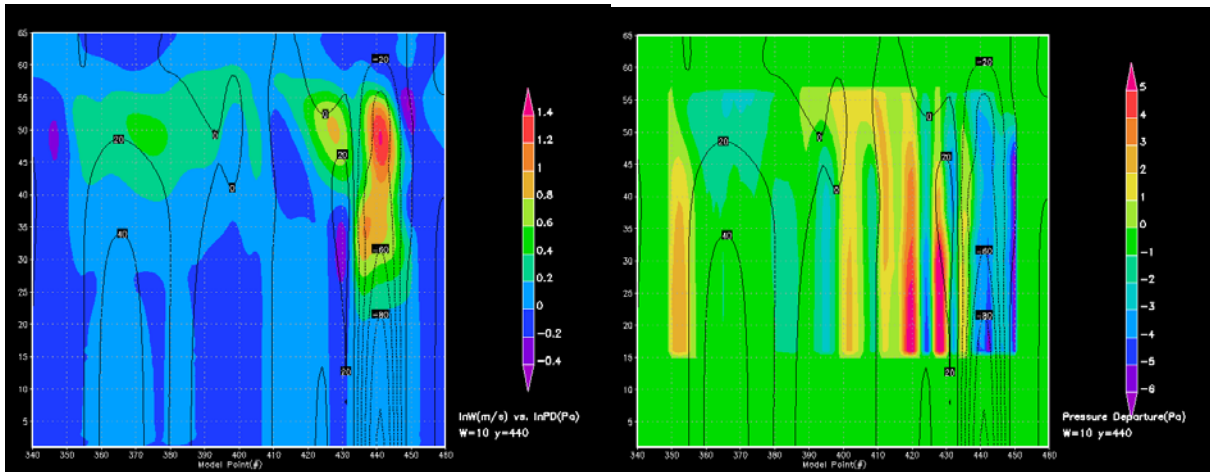


Figure 4 On the left an example of Analysed PD (contour) and W fields (shaded). The pattern shows a clear connection between both, as dictated by the vertical momentum equation. On the right the same PD field displayed on the shaded PD reference. Qualitative agreement is good, but there is a mismatch in magnitude of about one order of magnitude, with analysed PD bigger than reference PD.

3.2 Tests with Model Fields Aligned with Radar Pseudo-Images

If we add a third HARMONIE-AROME run to the previous set of simulations, identical in configuration to the 1-hour cycle run, but with the only difference that we assimilate in this new run Doppler Wind (DOW) radar pseudo-images by means of the field-alignment (FA) technique, we obtain a dataset that can be used to check the impact of assimilating these pseudo-images on short-range HARMONIE-AROME forecasts. We can call these three simulations NAT, TW0 and TW1 respectively. The procedure goes then as follows. From NAT we produce radar pseudo-images of reflectivity and DOW, although only the last ones will be used. The location and scan elevations correspond to a fictitious radar at 400,400 with two elevations at 0.5 and 1.5. We utilize these images to correct +1H forecasts in TW1 for 20 consecutive hourly cycles (2013/12/05 15UTC – 2013/12/06 23 UTC). We also use these pseudo-images as verification data for +1H forecasts by computing DOW differences (NAT-TW0) and (NAT-TW1) for that period.

The FA technique and some experiments with it have been presented elsewhere [11]. The alignment process generates imbalances that can be ameliorated if they are “up-scaled” with the covariance matrix B [11]. In this new test, the up-scaling is substituted by the VC method. Figure 5 (left) shows, somewhat disappointingly, that most of the impact is gone by the first hour. This could be due to FA corrections moving fast out of the radar range and therefore not showing up in the verification. In fact, the area chosen was swept by very strong winds (about 30-40 m/s) during most of the experiment period. In the figure one can indeed identify a dependency of the impact with mean error magnitude (first cases of the series show better impact). Also, it turns out that VC is by itself not able to spread increments significantly in the horizontal (Figure 5 right). VC is mostly about vertical dynamics and balances. It is expected that further enhancements of the algorithm to deal with this problem will improve its performance.

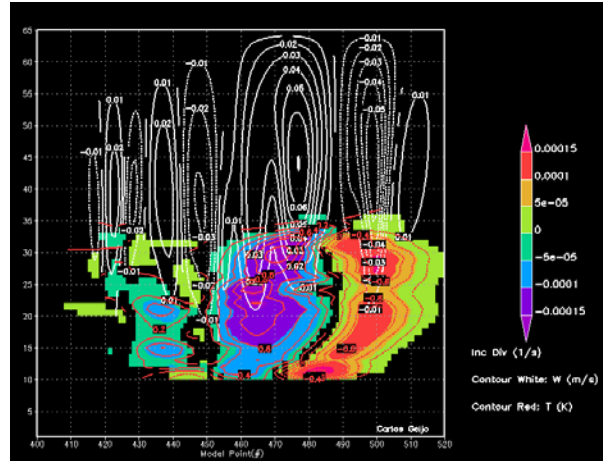
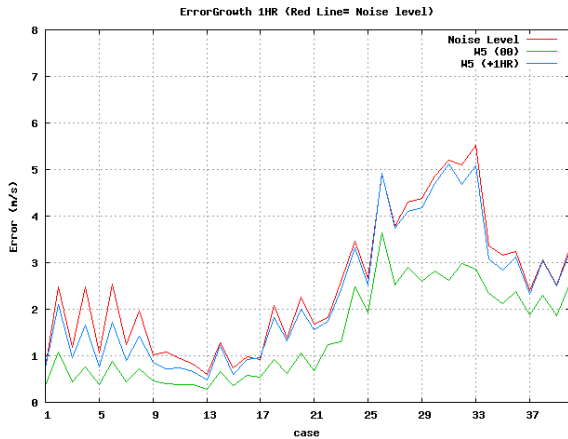


Figure 5 On the left, the impact on 1H forecasts of assimilating DOW data by FA technique, plus additional balancing with the VC method ($w=5$) is shown. The green curve corresponds to $(NAT-TW1)_0$ for all the cases included in the experiment. This parameter is DOW averaged for each elevation. As two elevations are considered, the total number of cases is 20×2 . The blue curve is $(NAT-TW1)_{+1}$ and the red curve is $(NAT-TW0)$ for the same time (i.e. null impact). When the blue curve reaches the red one, the impact has either dissipated or moved away of the radar range. On the right, a vertical cut showing the balanced increments of horizontal divergence (shaded), vertical velocity (white contours) and T (red contours).

3.3 VC as filter for LETKF Analyses

The Local Ensemble Transform Kalman Filter (LETKF) is an efficient ensemble-based variant of the Kalman Filter algorithm [7]. As pointed out in [7], localization may imply the need for some balancing before using these analyses as initial conditions. The goal of this test is to check whether VC can be used in an effective way for this task. A small 10 member ensemble generated by the SLAF method is used to run a 3H assimilation cycle LETKF experiment during a period of ten days (2012/09/20-2012/09/30). The domain is $576 \times 480 \times L65$ big at a nominal horizontal resolution of 2.5Km. Only conventional in-situ observations were utilized ($\sim 10^3$ obs/cycle). As the focus is on upper-air analyses, no surface data assimilation was done. To measure the impact on balance in the first hours of the forecast, a surface pressure tendency metric was used. Standard verification of mean-ensemble forecast and ensemble RMSE and Spread for lead times up to 12H were also carried out.

First we compare the surface pressure tendency evolution for a forecast initialized with the mean LETKF analysis x^a , and that initialized with this same analysis filtered as follows

$$(x^a)^* = x^b + VC [x^a - x^b] \quad \text{Eq 3.3.1}$$

Where the second term on the r.h.s denotes the application of the VC scheme to the (mean) analysis increments. In the notation of Eq2.10, we then have F^o_D , F^o_T , F^o_π given by LETKF (mean) increments and $F^o_w = 0$ (as our LETKF does not consider analysis of vertical velocity). In Figure 6 the result of this test is shown. The difference between the green and red lines indicates that indeed in this case localization has produced imbalances. The red line corresponds to an integration started from a 3H forecast and it marks the “0-noise” situation. The thin blue, purple and cyan lines correspond to runs initiated from filtered analysis with VC for three different w parameter values, 10, 5 and 1 respectively, that is, with increasing weight for the variational constraints. The case $w=1$ achieves reasonably good performance, while the other two cases show poor results. This problem has been traced down to the analysis of pressure departure (PD) and the issue of mismatch in order of magnitude between forecasted PD fields and VC analysed PD fields mentioned above. In the following results, an ad-hoc PD dumping factor ($\sim 1/10$) has been used to minimize these oscillations in pressure tendency for big values of w .

With respect to forecast verification, the skill of the mean forecast is equivalent with and without VC as far as the standard verification method can tell (not shown). Also in the standard verification of the mean forecast, there was no evidence that the scaled version of VC gives better scores than the no scaled version (not shown). To assess the impact on ensemble RMSE and Spread, an experiment with VC filter applied to all ensemble members was conducted and the results compared to those obtained with a non-filtered ensemble or “raw” ensemble.

$$(x^{a(i)})^* = x^b + VC [x^{a(i)} - x^b] \quad i=1,2,\dots,10$$

As one would expect, in general the filtered ensemble has less spread, but this decrease in spread does not produce worse RMSE scores. Figure 7 picks up two verifications to illustrate this discussion. On the left we have the verification for surface pressure. It is noticeable that the peak in spread for +1H forecast is reduced by VC. The aspect of the curve “spread vs. forecast range” casts doubts about this spread being spurious. It is clear then that VC has in this case been able to filter noise rather than removing genuine uncertainty measure. On the right, the verification for wind speed at 10m is shown. Here the spread vs. lead time curves are smooth but the one for the filtered case shows a clear increase with forecast range, as one would expect if uncertainty builds up as forecast develops in time. This increase is not seen in the “raw” case, where spread remains at a nearly constant value during the whole integration. As mentioned, RMSE scores are indistinguishable. In these experiments it was found that results with $w=10$ are to be preferred to smaller values of w , if there is much concern with the loss of spread.

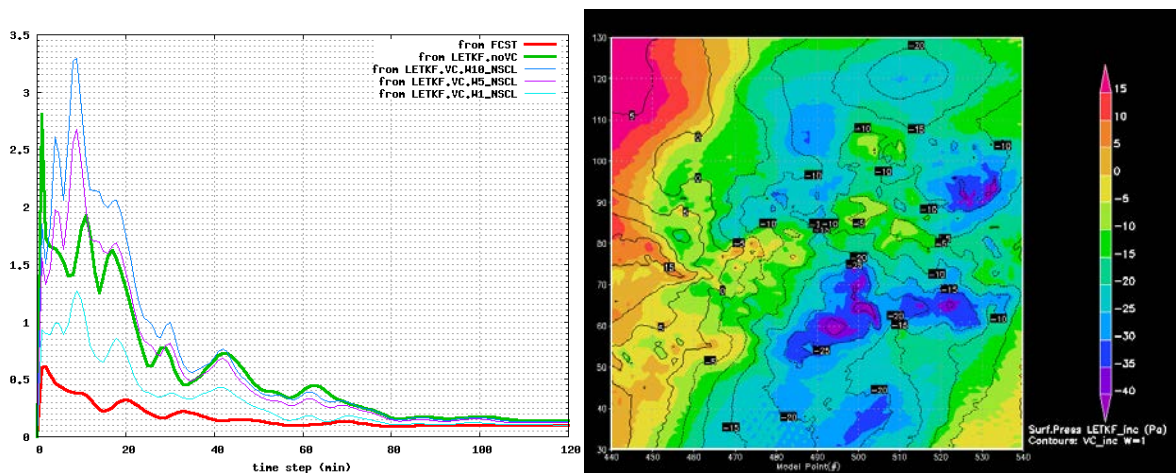


Figure 6 On the left evolution at time step resolution of a surface pressure tendency based metric. The green line corresponds to a run with mean LETKF analysis as IC, the red one is for the same case but with a 3H forecast as IC. Imbalances are present in the LETKF analysis. The thin lines correspond to this LETKF analysis filtered by VC for three different values of w (see text). On the right a snapshot of the Ps analysis as produced by LETKF (shaded) and after VC filtered (contours).

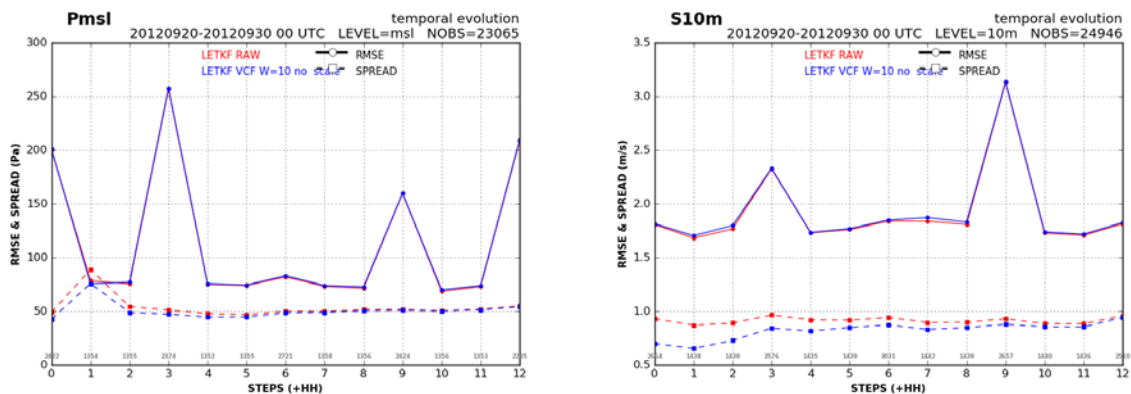


Figure 7 Ensemble RMSE and Spread vs forecast range for the experiment whose settings are presented in the text. Left surface pressure, right wind speed at 10m. See text.

3.4 Comparison between VC and 3D-VAR Statistical Balances

The last test in this first set of investigations on the issue of VC for DA in ALADIN-NH dynamics, aims at comparing the performance of these VC constraints versus the statistical balances encoded in the current 3D-VAR algorithm [8]. To this end, experiments for the same period, domain, assimilation cycle (3H), and observation usage as those employed in the LETKF test were performed. The control now is a standard 3D-VAR, while the experiments consist of univariate 3D-VAR followed by analysis increments filtered by VC to account for inter-dependencies among analysed variables, that is, processed as indicated by Eq 3.3.1 but now with x^a denoting one univariate 3D-VAR analysis instead of one (mean) LETKF analysis. Different values and options for the VC “tunable parameters” were considered (i.e. w weight, scale vs. no scaled, etc...). The following two panels, and the text at the foot, summarize the results obtained in this exercise.

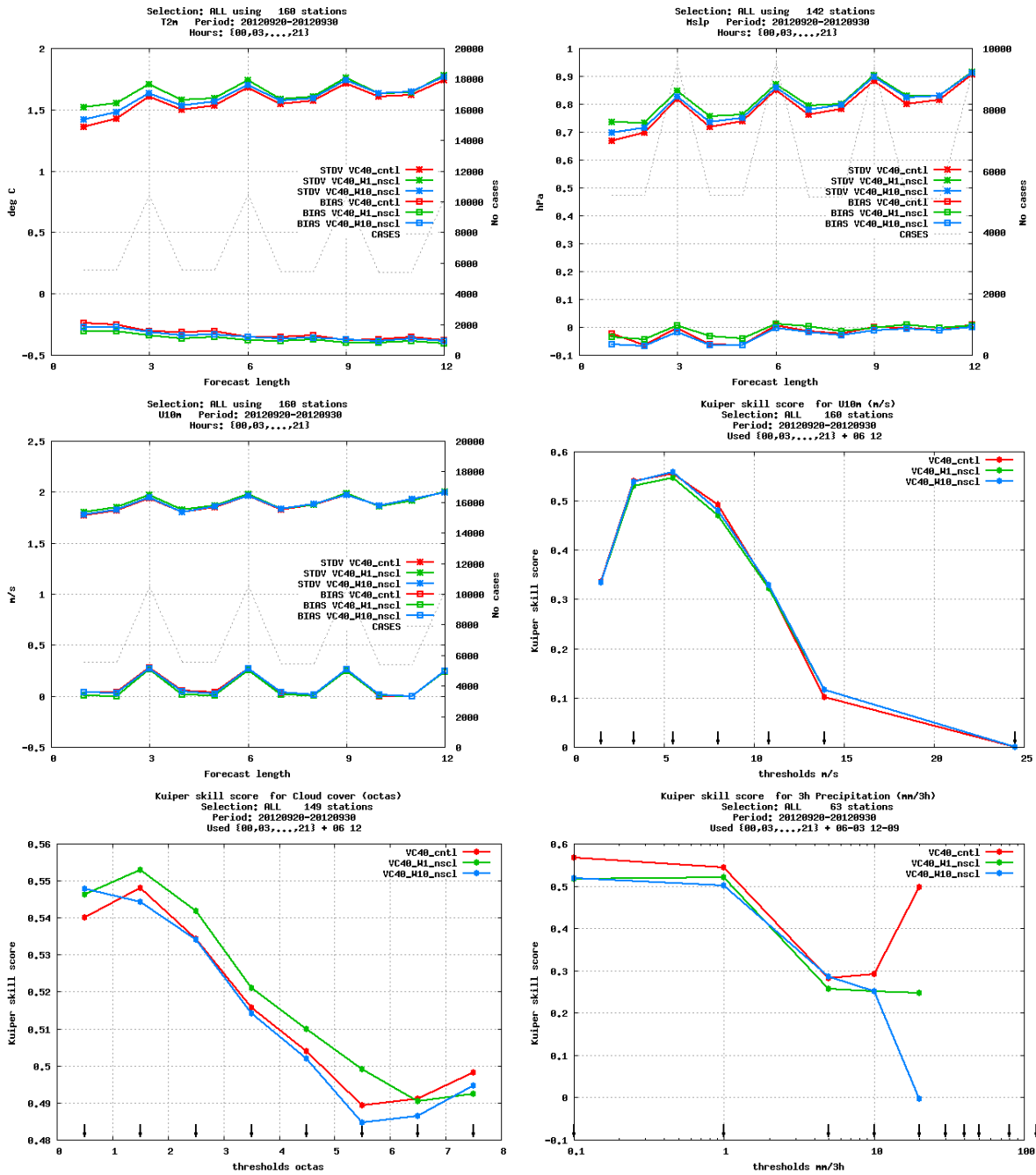


Figure 8 Some verification scores for the VC vs StatBal comparison. This set of plots corresponds to a “minimal VC tuning” with all the active w 's (i.e. for HD, T and π_s) equal to 1 (green lines) or 10 (blue lines). The red lines are for CNTL (3D-VAR with StatBal). On the first row we have T_{2m} and mslp. VC degrades these scores, with a tighter fit to increments ($w=10$) being closer to CNTL. The middle row corresponds to near surface wind (error vs lead time left and Kuiper Skill Score by thresholds to the right). Here the impact can be judged as neutral. The bottom row is for Cloud Cover (Kuiper Skill Score by thresholds) on the left and 3hours precipitation intensity (also Kuiper Skill Score by thresholds) on the right. Most constrained experiment ($w=1$) gives now somewhat better scores. In all cases the “no-scaled” version is shown. The “scaled” version turns out to give equivalent results (not shown)

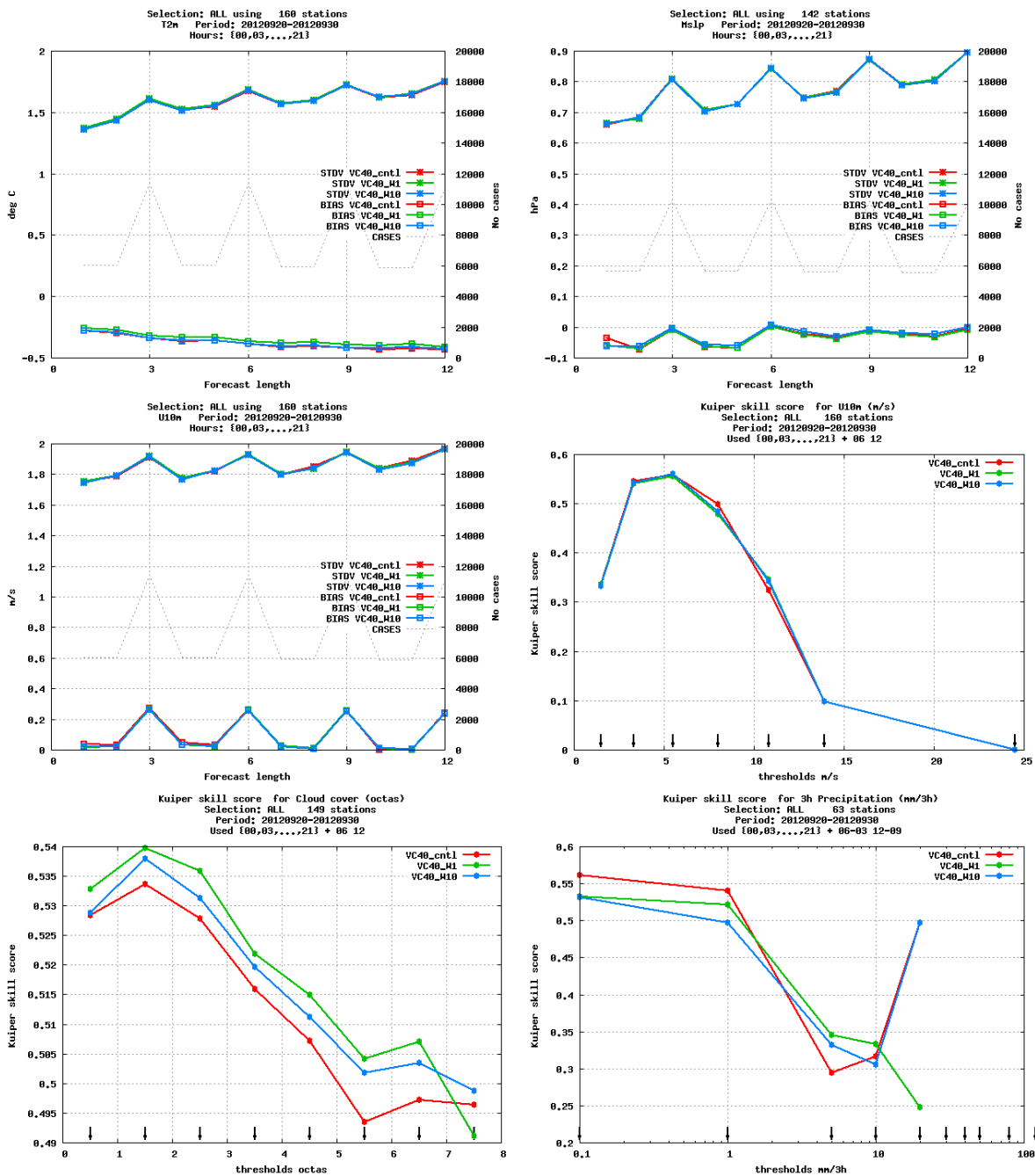


Figure 9 This panel has the same lay out as the previous figure (#8). In this instance the verification scores correspond to “Fine-tuned VC”, where weights for T and π_s are now given a big value ($w=100$), and w for HD equal to 1 (green lines) or 10 (blue lines). In this experiment, VC was applied to analysis increments with StatBal also incorporated. The red line again corresponds to CNTL (again, 3D-VAR with StatBal). The deterioration in T_{2m} and π_s is now gone, and there is virtually no change for near surface wind. The interesting point in this case is the improvement in cloud cover and 3H precipitation intensity, with still the strong constrained case ($w=1$ vs. $w=10$) giving the best results. One would like to conclude that this improvement is caused by inclusion of vertical velocity in the analysis.

4 Conclusions

The SI equations define dynamic relations among several variables that can be used in DA. A new algorithm that implements this idea is given by the solution to a variational (weakly) constrained

problem. The solution is obtained using Greens Functions. The SI system is a time-step forward operator, and this property gives to this new algorithm a nudging-like functionality, which makes it well suited for “continuous-in-time” DA. It also brings to the DA process the vertical velocity and PD fields.

A first implementation of this method has demonstrated its capacity to provide good equilibrium among horizontal and vertical momentum analysed fields. However, some mismatch in magnitude between analysed and forecast vertical velocity and PD fields has been observed. This will be the object of more investigation.

The method has also demonstrated its potential to improve vertical balances of assimilated wind fields generated by FA with radar DOW pseudo-images. First results so far can however be surely enhanced with further treatment of the FA increments (horizontal up-scaling).

First experiments with the LETKF DA algorithm (3h DA cycle, only conv-obs) have shown that this algorithm can filter spurious oscillations in the surface pressure tendency field. At difference with other digital filters, the filter design is almost completely dictated by the SI dynamics. On the other hand, standard verification scores show a clear reduction in ensemble spread. Although this result is to be expected, there is no simultaneous reduction in ensemble error and stochastic verification scores in consequence are not completely favourable. Also, first results with 3D-VAR do not show big gains with respect to the statistical balances method. All these tests however, have been done with 3 hours DA cycles and small amount of observations, conditions where initialization issues do not manifest in the foreground. Also the rather different numerical techniques employed in VC analysis and forecasts must clearly bias the results towards the wrong side. The introduction of some ad-hoc tuneable parameters helps to improve the verification scores.

5 References

-
- [1] Sasaki, Y. “Some Basic Formalisms in Numerical Variational Analysis”, *Monthly Weather Review*, Vol 98, No.12, Dec 1970a, pp 875-883
- [2] Thompson, P. “Reduction of Analysis Error through Constraints of Dynamical Consistency”, *Journal of Applied Meteorology*, Vol 8, No.5, Oct 1969, pp 738-742
- [3] Wahba, G. and Wendelberger, J. “Some New Mathematical Methods for Variational Objective Analysis using Splines and Cross Validation”, *Monthly Weather Review*, Vol 108, Aug 1980, pp 1122-1143
- [4] Fischer, C. et al., 2005 “An Overview of the Variational Assimilation in the ALADIN/France NWP System”, *Q.J.R. Meteorol. Soc.* 131; 3477-3492
- [5] Geijo, C., 2015 “A New Solver for the Non-Hydrostatic Semi-Implicit Scheme in HARMONIE using Green Functions”, *HIRLAM-ALADIN Newsletters #5* pp 138-162. (<http://www.umr-cnrm.fr/aladin/IMG/pdf/nl5.pdf>)
https://www.researchgate.net/publication/281293331_A_new_Solver_for_the_Non-Hydrostatic_Semi-Implicit_Scheme_in_HARMONIE_using_Greens_Functions DOI: 10.13140/RG.2.1.4076.4646
- [6] Ravela, S. et al, 2007 “Data Assimilation by Field Alignment”, *Physica D* 230, pp 127-145 (available from www.sciencedirect.com).
- [7] Hunt B.R. et al, 2007 “Efficient Data Assimilation for Spatiotemporal Chaos: A Local Ensemble Transform Kaman Filter”, *Physica D* 230 pp 112-126 (available from www.sciencedirect.com)
- [8] Derber J. and Bouttier F. “A Reformulation of the Background Error Covariance in the ECMWF Global Data Assimilation System”, *Tellus*, 51A, 1999, pp 195-221
- [9] Geijo, C., 2018 “ANNEX to Variational Constraints for Data Assimilation in ALADIN-NH Dynamics”.
https://www.researchgate.net/publication/326467111_ANNEX_to_Variational_Constraints_for_DA_in_ALADIN-NH_Dynamics. DOI: 10.13140/RG.2.2.17448.06402
- [10] Bénard, P. et al., 2010 “Dynamical Kernel of the ALADIN-NH Spectral LAM: Revised Formulation and Sensitivity Experiments”, *Q.J.R Meteorol. Soc.* 136, 155-169
- [11] Geijo, C. 2013, Presentation at the 6th WMO Conference on Data Assimilation.
https://www.researchgate.net/publication/281236886_Assimilation_of_Weather_Radar_Data_in_a_Convection_Permitting_NWP_System_using_the_Field_Alignment_Technique.
- [12] Laprise, R. “The Euler Equations of Motion with Hydrostatic Pressure as an Independent Variable”, *Monthly Weather Review* , Vol 120, January 1992, pp 197-207

VIEsion: Assimilation of Mode-S Data

Phillip Scheffknecht, Florian Meier, Christoph Wittmann, Lukas Strauss

1 Introduction

The VIEsion (Very fine rESolution modeling of aviation weather) project is a collaboration between the Austrian weather service ZAMG and the Austrian air traffic controller Austro Control. The core aim of the project is a further improvement of the aviation weather prediction, which is essential for a smooth operation of Vienna International Airport (VIE).

For this purpose, Austro Control provides the ZAMG with new Mode-S data gathered from commercial aircraft in the airspace over and around Austria, within the range of the Austrian radar. This data is then assimilated into a 1.2 km version of the AROME model. A small sample of the current results is presented below.

2 Austrian Mode-S Data

Distribution of the Data

The two core strengths of Mode-S data are its coverage of upper air layers, where data is usually limited to radiosondes and satellite data, and its high density in space and time. Figure 1 shows the spatial distribution of the data for the day of 2 May 2018, containing over 450000 data points. Most of the observations are located at cruise flight levels, between around 10 and 12.5 km above sea level.

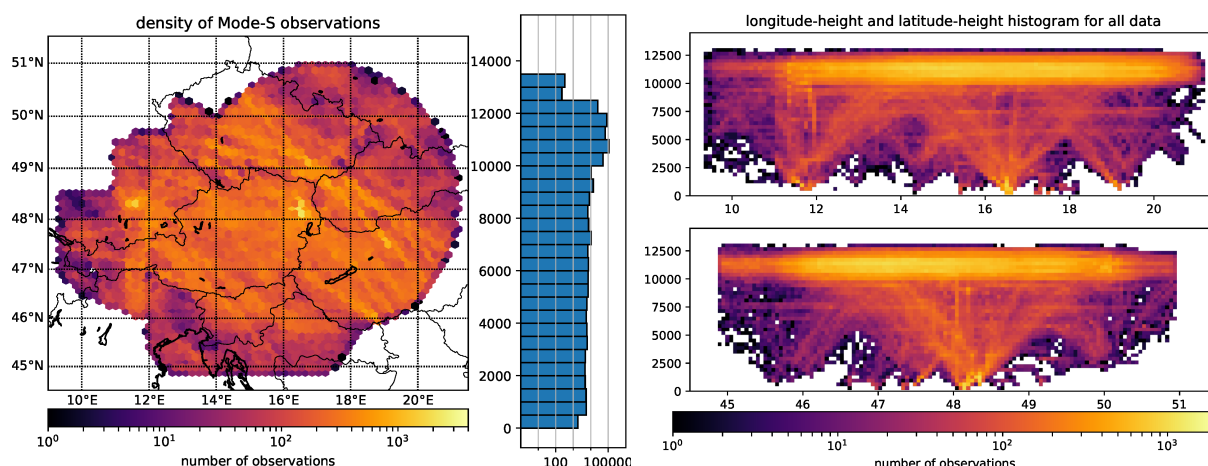


Figure 1: Distribution of 24 hours of Mode-S data for 2 May 2018 provided by Austro Control. The density is shown on a map (left) and in the vertical (y -axis in meters ASL) as 1-D histogram with bins of 250 mASL (center) as well as 2-D histogram in east west (top right) and north-south (bottom right) direction. The regions are colored according to the absolute number of observations within each cell on a logarithmic scale.

The lower parts of the troposphere are also sampled, albeit much less densely. The two vertical 2-D histograms in the right hand side panels of Fig. 1 show cones of denser observations extending downward where the major airports are located. The clearest signal is visible for Vienna International

Airport (VIE) at 16.5°E and Munich (MUC) at 11.5°E. Since the two are located roughly at the same latitude, they show as one in the lower right panel of Fig. 1, just north of 48°N.

Assimilation Tests

The current experiments consist of case studies which test the Mode-S data itself alongside new and experimental model configurations. The ZAMG is currently working on a 1.2 km version of the AROME model, which is being thoroughly tested. In addition, 500 m AROME is tested within the framework of the VIEsion project. Each case study consists of multiple simulations of an interesting event, and only a small sample is presented below.

Figure 2 shows the temperature observations of a flight assimilated in the 18 UTC simulation. The left panel shows the result of SCREENING, which compares the observations to the first guess and calculates the first guess departure. This departure is relatively low at flight level (purple) but tends to be higher at low altitudes (red). This results in a relatively noisy measurement series below about 700 hPa.

After this, MINIMIZATION thins the data and minimizes the cost function, pushing the model closer to the observations. As is apparent from the data in the bottom right panel, the model is adjusted strongly toward the observations, which can result in an in-homogeneous field along the flight track. Also, the sheer amount of measurements causes the cost function to converge more slowly. However, there is no direct indication that this causes problems during the following simulation. This was tested by greatly increasing the number of iterations of the minimization algorithm to achieve convergence, which resulted in no significant changes in the simulation results.

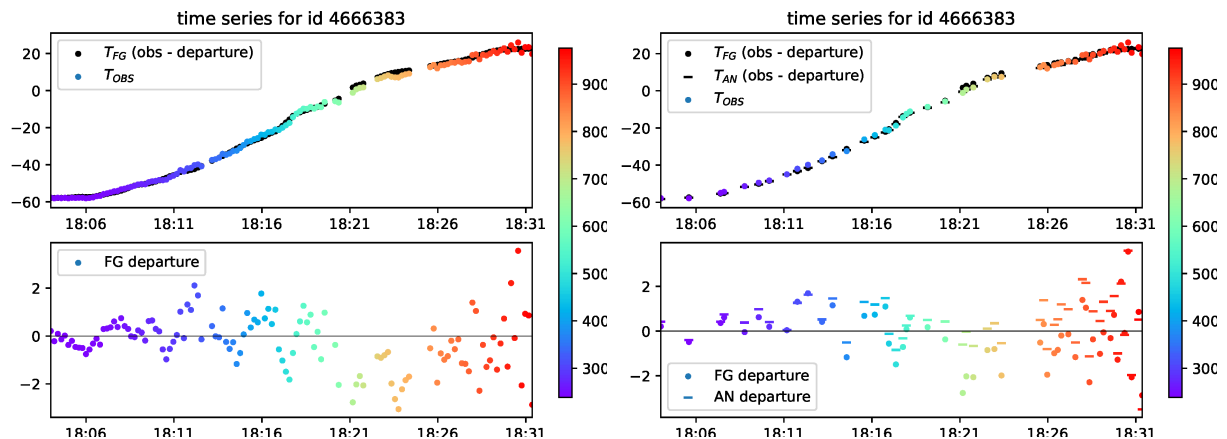


Figure 2: Example temperature data from a flight, showing output from SCREENING (left) and MINIMIZATION (right). The top panels show observed (color), first guess (black circles) and analysis (black dashes, only right side). The color of the data points indicates the pressure level (hPa) at which each observation is located. The bottom panels show the first guess departure (colored dots) and the analysis departures (colored dashes, only right side). For all panels, the y-axis shows the temperature (°C).

Since 2 May 2018 was a convective day with thunderstorms already present around 18 UTC, differences in measurements can be large over short distances. Each assimilation cycle is a trade-off between allowing the model to adjust the first guess to capture these mesoscale phenomena and preventing the model from assimilating erroneous measurements.

Simulation Results for the Convective Case of 2 May 2018

The convective case of 2 May was simulated using five configurations of AROME and initiation times from 09 to 18 UTC, resulting in a total of 44 simulations, four operational configurations, one every

three hours, and ten hourly runs for each of the experimental configurations. Table 1 shows an overview over the models.

Table 1: Simulation List where 18 indicates the initiation time of each model.

OPER18	ZAMG 2.5 km AROME, operational setup, coupled with IFS
RREF18	1.2 km AROME setup in testing
RMDS18	1.2 km AROME setup in testing with Mode-S assimilation
VREF18	500 m AROME experimental setup, coupled with RREF, not lagged
RREF18	500 m AROME experimental setup, coupled with RMDS, not lagged

The 2.5 km OPER is using the operational model configuration and is based on the respective operational analysis. The 1.2 km RREF and RMDS simulations are initialized with their own analyses and coupled to an OPER run with a lag of 3 hours, i.e. RREF18 and RMDS18 runs are coupled with the OPER15 run (which is not shown), whose three hour forecast is interpolated on the finer grid and used as first guess. The 500 m runs are initialized from interpolated 1.2 km analyses at the same time, i.e. from the 18 UTC RREF and RMDS analyses, respectively.

The convective event of 2018-05-02 took place mostly between 18 and 21 UTC with no relevant precipitation observed in the 9 hours after the event, such that the 12 hour accumulated precipitation represents the event accurately. In Figure 3, the five selected runs are compared to the INCA analysis, which is a gridded ZAMG product based on radar and surface observations.

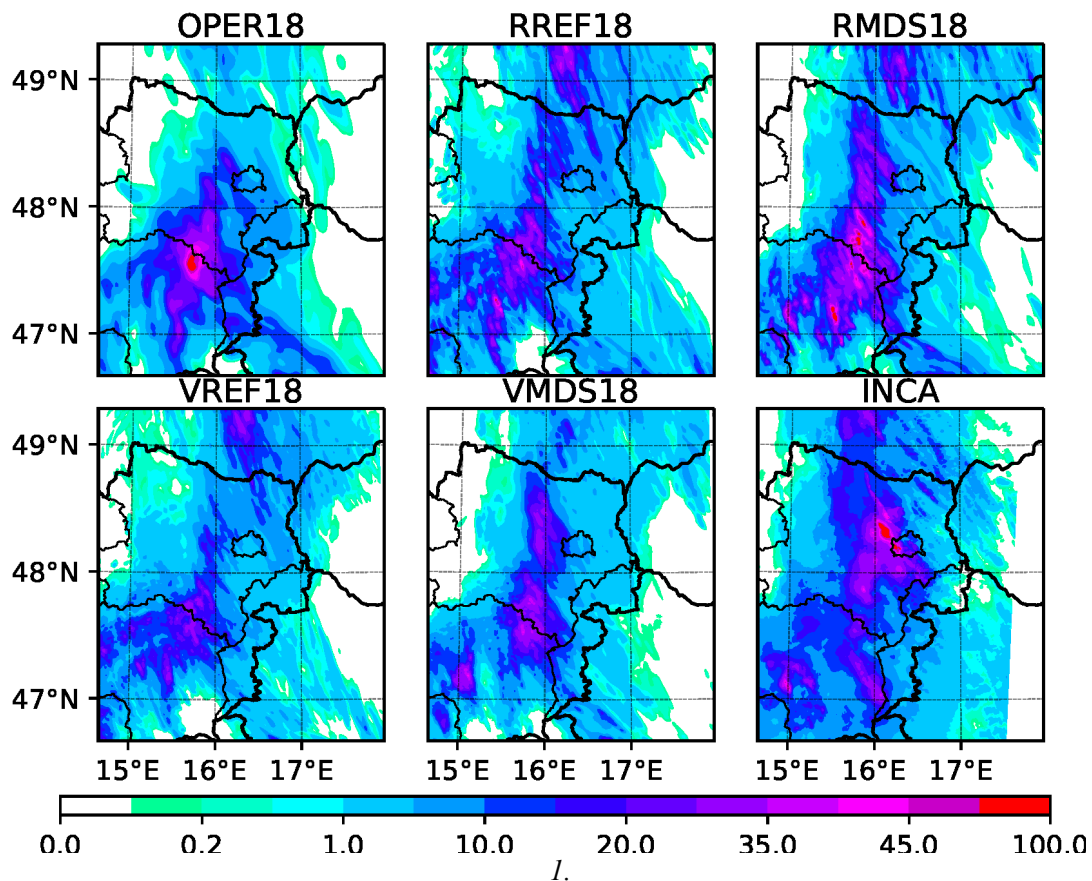


Figure 2: 12 hour accumulated precipitation (mm) from 18 UTC of 2 May until 06 UTC of the following day for 5 simulations initiated at 18 UTC (first five panels) and the INCA analysis (bottom right) accumulated over the same period. The borders of Vienna are visible just northeast of 16°E and 48°N.

The INCA analysis in the lower right panel of Fig. 3 shows values between 50 and 100 mm just northwest of Vienna and a long rain band stretching over most of eastern Austria along 16°E. All five simulations capture a convective event in the vicinity of the observed one, but there are substantial differences between the individual models.

The operational configuration (Fig 3, top left) misses the bulk of the precipitation north of the 48°N and places the heaviest precipitation along the border between Styria and Lower Austria. The 1.2 km RREF simulation captures the band better, but fails to reproduce the large maximum northeast of Vienna. When using Mode-S data, the precipitation northeast of Vienna increases by a factor of around 2, from 15 to over 30 mm, but the highest values are still found too far south. The 500 m simulations perform similarly to the 1.2 km ones, reproducing the precipitation band well but failing to locate the heaviest maximum. Overall, their precipitation values are slightly lower, which is a result of the different model dynamics. Just like for the 1.2 km simulations, the Mode-S data helps to better capture the northern part of the rain band.

3 Conclusions and Outlook

The above results show that Mode-S data can help to better capture mesoscale events. However, these results are a close look at a minor detail within a larger case study, which is in itself only a small part of the conducted tests. The overall results are mixed and evaluation is challenging, because high resolution model output compares poorly to high resolution observations when using standard methods like mean absolute error or correlation, even if the overall forecast would be considered useful and good by a forecaster. New quantitative methods are required to give more definitive answers of how much improvement can be expected from the regular use of Mode-S data. Only this quantitative evaluation of all the simulations using new tools will allow to accurately quantify the usefulness of Mode-S data in high resolution mesoscale modeling.

On the use of amateur weather observations in an operational nowcasting and NWP framework

Trygve Aspelien, Cristian Lussana, Thomas Nipen, Ivar Seierstad

1 Introduction

Observations of near surface weather parameters like screen level temperature, humidity and pressure have frequently been observed also in private homes for centuries. The recent technological developments make it possible to include this technology in all kind of gadgets and also share the data. The advantage is that we possibly can get access to a lot of weather data, also in areas having a sparse GTS observation network today.

Even though the quality of the sensors are normally quite good, the observation quality can suffer from misplacement (e.g. temperature measurement directly in the sun) or biases in how the measurement is performed. Amateur weather observations provide a lot of extra observations on top of the observational network we use today, but still only where people go or live so unpopulated areas will potentially still be left without conventional surface observations. The temporal resolution of the amateur weather observations are often very high and in the order of minutes.

There are several services covering Norwegian domains which provide a public API of amateur weather observations and these are used in nowcasting and correction of forecasts in MET-Norway's public API since March 19th, 2018 (i.e also on Yr.no).

2 Quality control

The quality control when using amateur weather observations is extremely important. One bad observation being used in the analysis can degrade the product significantly. The rule of thumb we use for amateur weather observations is never to trust a single observation and let the observations support each other. The system used is the in-house developed open source software TITAN.

TITAN has a wide range of different tests implemented, most importantly a spatial consistency check (SCT: Lussana et al., 2010), a buddy check, plausibility test, isolation test and a first guess check. The latter is so far applied only for snow depth observations where only observations from the international observation network are available. The SCT tries to fit a predefined profile (Frei, 2014) to the observations. The observations differing too much from the best fit profile are rejected.

For more information and a more detailed description of the individual tests in TITAN see the online documentation <https://github.com/metno/TITAN>

3 Operational nowcasting - post processing of MetCoOp EPS (MEPS)

The term nowcasting is here a bit different from how it is used in other contexts. The high temporal resolution of the amateur weather observations make it possible to do an analysis every hour but the input data, the

forecasts from MEPS, are only available 4 times a day. That means that the analysis is done often but only as a post-processing of the input data from the NWP model.

First the MEPS input data is downscaled with the tool gridpp (Sec: 3.1) from a horizontal resolution of 2.5 x 2.5 km to 1 x 1 km. The downscaler is for example taking into account elevation differences when interpolating to the fine scale grid.

Every hour a new quality control and analysis for screen level temperature is performed. The bias in every grid point for the whole time range of the latest available forecast is weighted as a function of the bias for the analysis time and the corresponding time of the previous day.

3.1 Analysis method

The method used for the analysis is based on Optimum (or Optimal) Interpolation (OI), however, two different schemes have been implemented.

If the background is composed of an ensemble of fields, the background error covariance matrix is derived directly from that ensemble (as for Ensemble Optimal Interpolation (Evensen, 1994)), such that it is weather-dependent. The scheme is applied on a gridpoint-by-gridpoint basis and a localization procedure is applied to remove spurious correlations between distant locations.

For the deterministic case -or as a fallback if a significant part of the ensemble is missing- the background error covariance matrix is specified by means of an analytical function, which in our case is a Gaussian function (i.e., a homogeneous and isotropic correlation function in the three dimensional space).

The software performing both the downscaling and the OI analysis is the in-house developed and open source tool gridpp. It is command line based and very simple to run with modified input settings. An example of the result can be seen in Fig. 1. This is a normal situations with warm valleys that are not resolved in the model or in the 1 km downscaled product, but the large extra amount of observations are able to indicate the location of the warmer valleys.

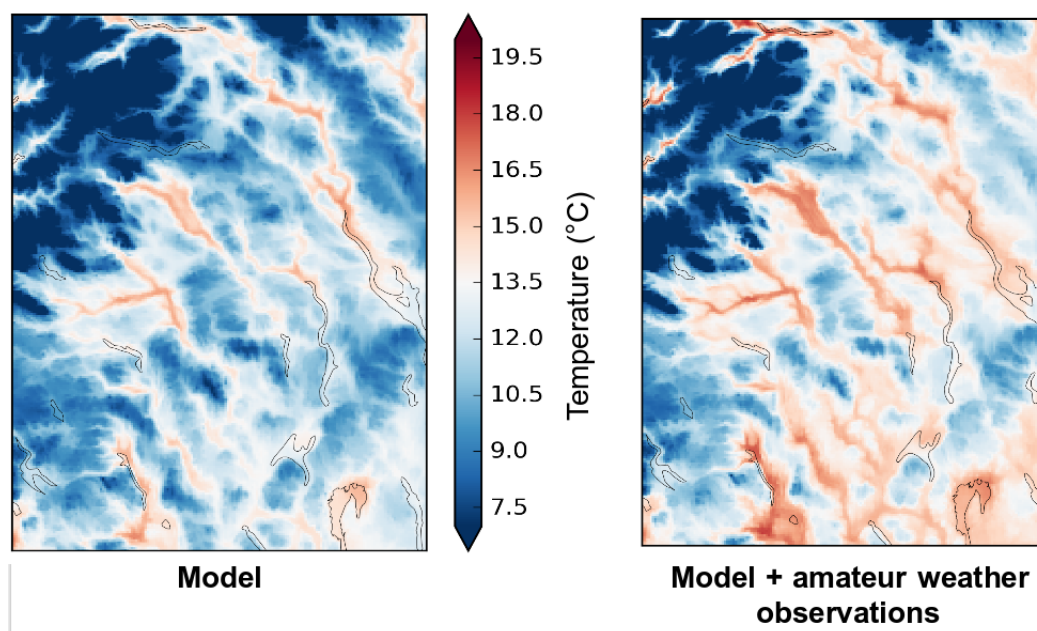


Figure 1: Example of OI analysis using amateur weather observations. Left downscaled raw field and right after the OI analysis using amateur weather observations.

3.2 Other analysis products

The tools TITAN (Sec 2) and gridpp (Sec. 3.1) are developed as part of the project RadPro. This is a close collaboration with Norwegian hydro-power companies. RadPro and other collaboration projects with The Norwegian Water Resources and Energy Directorate (NVE) will ensure that daily analysis products on 1x1 km grid should be produced for the following weather parameters:

- Temperature
- Precipitation
- Cloud cover
- Humidity
- Wind speed
- Snow depth

4 Amateur weather observations in the NWP analysis

The products described so far have been post-processed products made on the basis of a produced weather forecast with the NWP model (MEPS). The idea is that the quality control described in Sec 2 and the analysis procedure described in Sec 3.1 can be utilized to provide a better initial condition for MEPS and hopefully also provide a more accurate forecast.

Today MEPS uses the software CANARI to perform a screen level analysis of temperature and humidity and the surface snow depth. The screen level is assumed to be a proxy on how to update the soil moisture and temperature as very few in-situ observations exist real-time for the soil.

Since the methods to use the amateur weather observations now exist it is tempting to see if it is possible to use TITAN and gridpp to create the soil analysis. An extra advantage of doing it with these methods is that the methods are open source and de-coupled from the complete model system which make it possible to use in the offline SURFEX community. A disadvantage is that the tool CANARI is already quite powerful. On the other hand is CANARI also quite complex since it is twirled into the the whole variational assimilation system. Moreover CANARI is rapidly changing and as a consequence, the maintenance is a rather heavy effort.

Offline tests show that similar results to CANARI can be performed and with TITAN and gridpp when applying compliant settings (E.g. Fig. 2). Since the settings can be changed on command line it makes experimenting trivial.

A test on the land area fraction is implemented in gridpp and used for the snow depth analysis. For snow it important that the proper model equivalent of snow depth also is located in a land point. Also for screen level temperature and humidity this could be applied, but the land sea contrast is not as important as for snow depth which is not defined for ice-free sea points.

The screen level analysis of temperature and relative humidity and snow depth are used as input to the soil assimilation. In MEPS this is done inline from the binary performing the horizontal OI analysis (CANARI), in the alternative approach outlined here the horizontal OI analysis is provided as ASCII input to the SODA binary. The SODA binary is internally calling the same routines as CANARI which ensures consistency between the different methods.

The same analysis methodology for the NWP analysis is implemented into a research version of the HARMONIE-AROME script system (based on MEPS) and tests are ongoing.

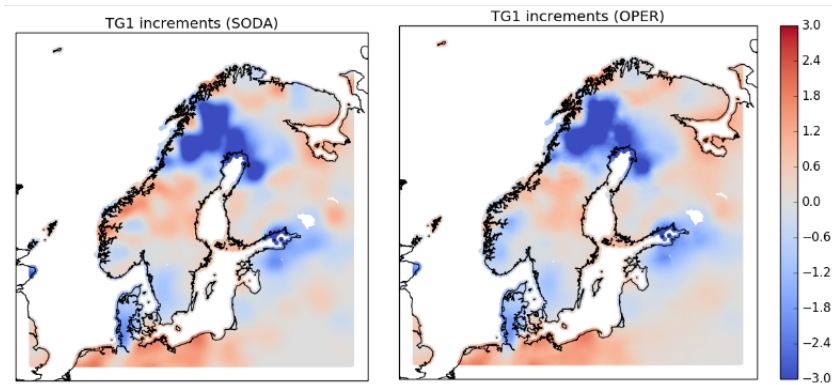


Figure 2: Analysis increment in soil level temperature level 1 (uppermost cm). Left using the offline tools described in Sec. 4, right from the operational MEPS using CANARI

5 Conclusions

The numerical integration of a NWP model is depending on the initial conditions. Higher quality of the initial conditions is likely also to give a better quality of the forecast. The availability on a real-time basis of a dense network of amateur weather observations can potentially provide better initial conditions for the operational weather forecasts, thus improving the quality of the raw NWP forecast before distributing it.

Since becoming operational the nowcasting system at MET-Norway is running every hour and it is improving the short-term temperature forecast significantly. The day 1 and day 2 forecasts are improved too.

The same analysis methodology for the NWP analysis is implemented into a research version of the HARMONIE-AROME script system (based on MEPS) and tests are ongoing.

6 References

gridpp - Gridded post-processor (<https://github.com/metno/gridpp>)

TITAN - auTomatIc daTa quAlity coNtrol (<https://github.com/metno/TITAN>)

RadPro: <https://www.met.no/prosjekter/radpro>

Evensen, G., 1994. Sequential data assimilation with a nonlinear quasi-geostrophic model using Monte Carlo methods to forecast error statistics, *J. Geophys. Res.*, 99(C5), 10143-10162, doi: 10.1029/94JC00572.

Frei, C., 2014. Interpolation of temperature in a mountainous region using nonlinear profiles and non-Euclidean distances. *International Journal of Climatology*, 34(5), pp.1585-1605.

Lussana, C., Uboldi, F. and Salvati, M.R., 2010. A spatial consistency test for surface observations from mesoscale meteorological networks. *Quarterly Journal of the Royal Meteorological Society*, 136(649), pp.1075-1088.

ALARO-1 Canonical Model Configuration Developments: shallow convection and surface roughness

Radmila Brožková, Ján Mašek

1 Introduction

In ALARO, the shallow convection scheme is handled as a part of the turbulence scheme TOUCANS. Recently, further improvements were proposed and implemented regarding the determination of one of the key parameters of that scheme. Works on coupling TOUCANS with the SURFEX scheme has begun in a more rigorous way within LACE. In order to ensure the ascending operational compatibility with using the ISBA scheme, the question of surface roughness treatment was addressed at first. Still on the ISBA side the roughness computation in presence of snow revealed a rather complicated approach. A unification proposal has been formulated.

2 Shallow convection

The effects of water phase changes, causing density fluctuations, are taken into account by a parameterization of the moist buoyancy flux, following the work of Marquet and Geleyn (2013). Equations of that scheme are now published in the recent paper by Bašták et al., 2018. As mentioned there, two key parameters ought to be determined, i.e:

$$\begin{aligned} & \frac{N^2(C)}{gM(C)} \\ &= \left(\frac{c_{pd}}{c_p} \right) \frac{\partial \ln \theta_l}{\partial z} \\ &+ \left\{ \frac{R_v - R_d}{R} + \hat{Q}(C, C_n) \left[\frac{L_v(T)}{c_p T} \frac{R}{R_v} - 1 \right] \left[\frac{R_v - R_d}{R} + \frac{1}{1 - q_t} \frac{1}{1 + D_C} \right] \right\} \frac{\partial q_t}{\partial z} \end{aligned}$$

the parameter \hat{Q}_{hat} highlighted by red and its relation to the cloud fraction C . Note that C_n parameter is of skewness type and has its interpretation as a cloud fraction at neutrality. The relation of C to \hat{Q}_{hat} has been determined from LES data (see Bašták et al., 2018, also for the rest of notations). However, C should be determined or iteratively inverted from \hat{Q}_{hat} . Whatever approach is taken, the boundaries of \hat{Q}_{hat} and C remain 0 and 1.

In the above mentioned paper C is determined from Sommeria and Deardorff (1977) scheme. In contrast to it the ALARO-1 implementation adopted a mass-flux type of computation proposed by Lewellen and Lewellen (2004) to obtain a first guess of \hat{Q}_{hat} . The scheme to obtain \hat{Q}_{hat} profile is therefore crucial, even if it is rather crude in the end. The core is inspired from the ascent profile computation used in the moist deep convection parameterization, with a lot of simplifications. Our recent proposals concern some more simplifications, corrections and removal of arbitrary thresholds which were setting the resulting \hat{Q}_{hat} to zero. First, we verified that we do not need to introduce any entrainment parameterization as already claimed by Lewellen and Lewellen (2004). Second, we included a proper treatment of negative buoyancy as proposed by Luc Gerard. Third, we do not link

any more the abortion of the cloud to some threshold of turbulent energies. Finally, we also dropped the idea of having moist Brunt-Vaisala frequency stability threshold to nullify Q_{hat} , which was used in the first implementation of the scheme. Like that arbitrary thresholds, influencing feedbacks in an incorrect way, were removed.

Recent modifications led to further improvement of results. In summer season the interaction with moist convection scheme is changed, as it comes out from the DDH diagnostics (not shown). Transport of heat and water is improved by reducing warm and dry bias at the top of boundary layer. Precipitation location gets also better, as it can be seen on Fig. 1.

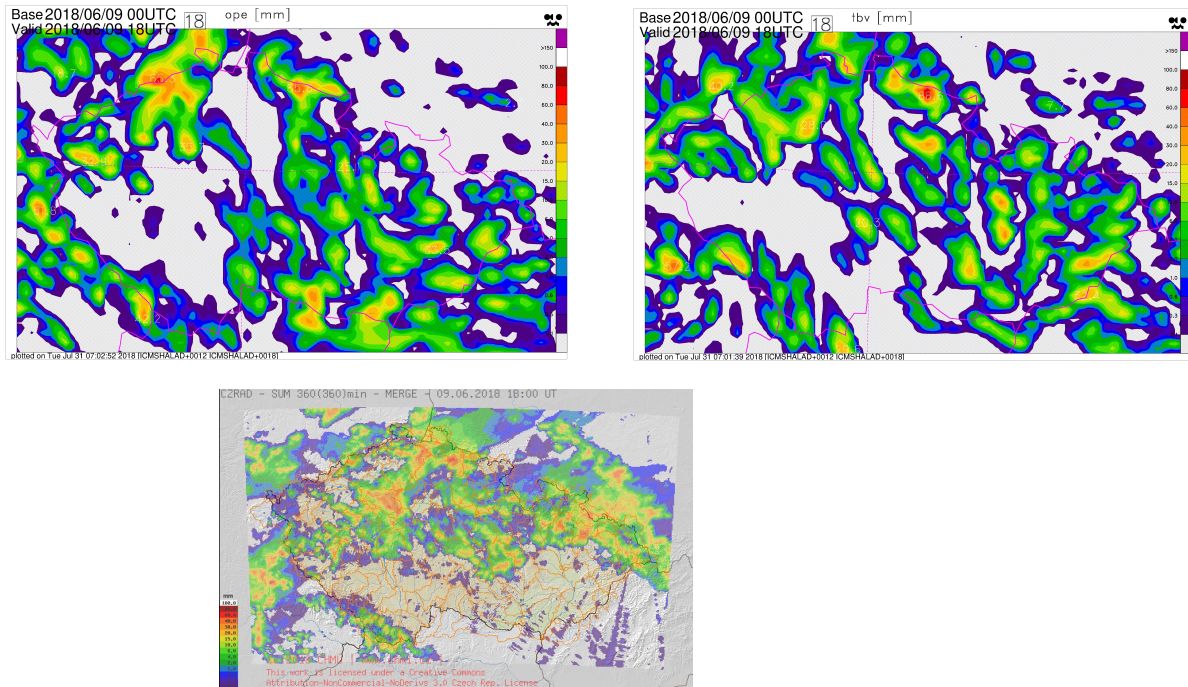


Figure 1: Precipitation sums of 09/06/2018 from 12h to 18h UTC over Czech Republic. Upper row: forecast at 18h lead time, reference (left), test (right). Bottom panel: verifying observations – merge of radar and gauges.

The shallow convection modifications became operational in Prague on 10 July 2018, together with the assimilation of MODE-S EHS data.

3 Surface roughness in presence of snow

By inspecting the surface roughness computation in order to move to the coupling of ALARO with SURFEX, we found couple of bugs and inconsistencies still on the side of the ISBA scheme. Our aim was to move first to the option when thermal roughness does not include the contribution of sub-grid-scale orography. The problems mentioned concern namely the treatment of presence of snow in that option, which was used in ARPEGE before switching to SURFEX. There is a detailed technical note by Ján Mašek, including relevant equations. Here we highlight the main points.

There are three different grid-box snow fractions used – one for albedo, one for computing dynamical effective roughness and one for computing thermal roughness. The problem is that their values may differ dramatically at some places, especially in the mountains. We can easily find an example of having the “albedo” snow fraction equal to almost one and the “dynamical effective roughness” snow

fraction equal to one percent, all that in one point. This is really not a sound situation, and for making the model working specific tunings had to be used, with rather curious parameter values.

To reach a quick win, we have made a proposal to unify the grid-box snow fraction for all three computations. New unified formula for grid-box snow fraction reads:

$$f_{snow}^{bg} = \frac{W_{snow}}{W_{snow} + W_{snow}^{crit} \left(1 + \frac{z_{0D}^{nosnow}}{a_2} \right)}$$

Where W_{snow} denotes snow reservoir. There are two tuning parameters – critical value of snow reservoir and the parameter a_2 . They reach now reasonable values, e.g. the multiplicative factor in the denominator may vary from 1 to 1.2.

We have made some preliminary tests, including an experiment with a full assimilation cycle. New formulation helps to improve screen level temperature and wind scores, see Fig. 2.

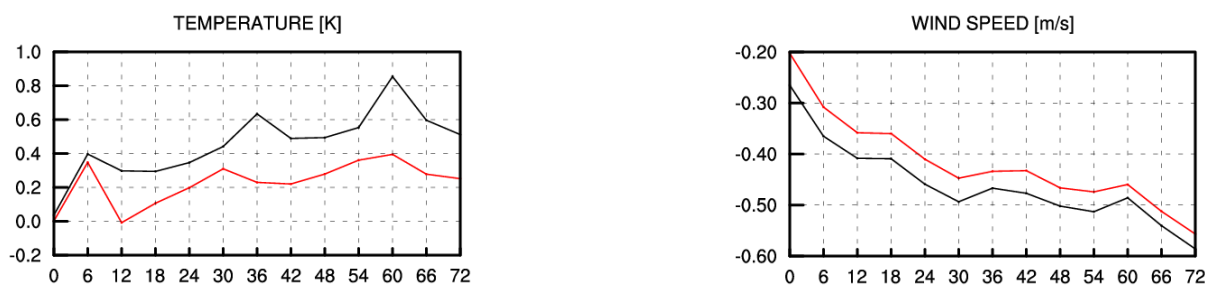


Figure 2: Bias of 2m temperature (K) and 10m wind (m/s), averaged from 0h UTC forecast over period 14/01-31/01/2017. Black line – reference; red-line – new grid-box snow fraction formulation with tuning, sub-grid scale contribution is not included in thermal roughness.

The implementation is quite easy and is available in the code starting by the export version of CY43T2. The activation requires to re-compute climate files and set the relevant namelist switches, see the technical report for details. The computation of surface roughness and drag coefficients on the SURFEX side shall be still checked. Unfortunately, a cleaner comparison between the current two-layer ISBA and the SURFEX implementation is not possible, since one cannot use the same physiography databases in both.

4 References

Bašták Ďurán, I., Geleyn, J.-F., Váňa, F., Schmidli, J., and R. Brožková, 2018: A turbulence scheme with two prognostic turbulence energies. *Journal of the Atmospheric Sciences*, <https://doi.org/10.1175/JAS-D-18-0026.1>.

Lewellen, D. C., and W. S. Lewellen, 2004: Buoyancy flux modelling for cloudy boundary layers. *Journal of the Atmospheric Sciences*, 61 (10), 1147–1160, doi:10.1175/1520-0469(2004)061h1147:BFMFCBi2.0.CO;2.

Marquet, P., and J.-F. Geleyn, 2013: On a general definition of the squared brunt-vaisala frequency associated with the specific moist entropy potential temperature. *Quarterly Journal of the Royal Meteorological Society*, 139 (670), 85–100, doi:10.1002/qj.1957.

Mašek, J., 2018: Improved treatment of surface roughness in the ISBA scheme. Technical note, 12pp.

Sommeria, G., and J. W. Deardorff, 1977: Subgrid-scale condensation in models of nonprecipitating clouds. *Journal of the Atmospheric Sciences*, 34 (2), 344–355, doi:10.1175/1520-0469(1977)034h0344:SSCIMOi2.0.CO;2.

A few thoughts about cloud reunification in Alaro

Luc Gerard

1 Introduction

Up to now and for historical reasons, validated Alaro versions have been using separate representations of radiative and microphysical clouds. From the beginning, Alaro introduced prognostic variables for cloud ice and droplets, falling snow and rain. Cloud condensates are produced or evaporated in the so-called 'cloud scheme', while the microphysics scheme converts part of these into precipitation and handles the evolution of precipitating species. The cloud scheme selected for Alaro was developed using an empirical relation from Xu and Randall (1996), completed by a closure implying a critical relative humidity. While this scheme computes a cloud fraction, this value was not found satisfactory. Another diagnostic scheme re-computes a cloud fraction eventually used for cloudiness diagnostic, and radiative exchange computation. Hence the prognostic cloud condensates used in the microphysics are disconnected from the model clouds.

2 Assessing the cloud shemes

2.1 Xu-Randall derived scheme

The XR96 formula expresses the total cloud fraction N as a function of the (steady-state) mean over large grid boxes of relative humidity $RH = \frac{q_v}{q_s}$, cloud condensate \bar{q}_c and saturation moisture \bar{q}_s :

$$N = (RH)^r \left[1 - \exp\left\{-\frac{\alpha \bar{q}_c}{(\bar{q}_s(1 - RH))^\delta}\right\} \right], \quad \alpha \sim 100, r \sim 0.25, \delta \sim 0.49 \quad (1)$$

Assuming conservation of total humidity, $q_t = q_c + q_v$, there remains two unknowns N and either q_c or q_v or RH , as long as the saturation humidity is kept constant. To close the scheme, a very simple closure relation has been used, assuming $RH = 1$ over N and a critical relative humidity RH_c in the clear part of the grid box.

Since the cloud scheme is used to re-adjust the humidity from a non equilibrium state, the underlying assumptions can then be questioned. In case the obtained condensate is larger than the initial value (condensation),

- computed condensate is a transient excess value
- precipitation will reduce it together with total humidity
- condensation induces local heating that increases q_s : assuming it constant will overestimate the condensation.

If on the contrary, the final condensate is smaller, there is evaporation; this induces local cooling, reducing q_s ; assuming it constant will overestimate evaporation.

The closure relation concerns the variability over the grid box, introducing an arbitrary critical relative humidity assumed to be realized (in average) out of the cloudy region. This is a very strong constraint, and moreover the scheme formulated quite arbitrarily $RH_c = f(z, phase, \Delta x)$ in order to obtain acceptable model scores.

In addition, the model uses a simplified expression of the XR formula and quite deviant values of the parameters ($\alpha \sim 150$). In general, the cloud fraction is too binary, there is a lack of moderate cloud fractions.

2.2 Improvement attempts

In order to keep the good model scores, diabatic effects as well as phase changes should be kept; however, this would imply keeping everything so that we cannot change the unpleasant cloud fraction.

It was tempting to try to address the physical weaknesses: limitation of suspended condensate and of diabatic effects, complete reformulation of the closure. For the latter, we revised the notion of critical relative humidity and its vertical profile (setting it more similar to what can be suggested from XR97), and introduced dependence of subgrid variability on TKE.

We were able that way to obtain quite acceptable cloud fractions. Unfortunately it lead to unacceptable degradation of the model scores. It can be possible to recover acceptable tendencies on particular cases only.

There appears to exist no alternative to maintaining the dissociation between microphysical condensates and radiative cloud fraction, while trying to build an adjustment scheme starting from a steady-state formula.

2.3 Alternative solutions

The diagnostic radiative cloud evaluation uses a very large set of parameters, including for instance arbitrary scaling of the stratiform condensate (qssusv/qsmocd). Still as it yields realistic clouds, the goal is to approach those directly with the prognostic cloud scheme.

Cloud fractions obtained with the Smith scheme as coded under LSMITH_CDEV seems to produce better clouds than the XR scheme; however we also find at its end an arbitrary scaling of cloud and condensate that are forced to zero towards the surface, and a uniform multiplication of the cloud fraction by rfacnsm=1.4.

The much more complex Rash-Kristjánsson implementation (LRKCDEV) still uses a rather arbitrary critical relative humidity profile.

We are currently revising and bug-fixing the Smith-Gerard (LSMGCDEV) switch, to test the possibility to obtain directly usable cloud fraction while keeping good model scores.

3 References

- Xu, K.-M. and D. A. Randall. A semi-empirical cloudiness parameterization for use in climate models. *J. Atm. Sci.*, 53:3084-3102, 1996.
- Smith, R. N. B. A scheme for predicting layer clouds and their water content in a general circulation model, *Q. J. R. Meteorol. Soc.*, 116:435-460, 1990.
- Rasch, P.J. and J. E. Kristjánsson, A comparison of the CCM3 model climate using diagnosed and predicted condensate parameterizations, *J. Climate*, 11:1587-1614, 1998.

Use of CAMS Aerosol Fields to Modify the Cloud Condensation Nuclei in HARMONIE-AROME

Daniel Martin-Perez. AEMET

1 Introduction

The microphysical parametrizations (autoconversion, cloud droplet sedimentation and collision of cloud liquid) in HARMONIE-AROME take constant values for the concentration number of cloud condensation nuclei (CCN). These values depend on whether the grid point is over sea, land or over urban terrain. So, it is considered 100 per cm^3 over sea, 300 per cm^3 over land and 500 per cm^3 over the towns, independently of the level. In order to get a more realistic representation of the CCN, aerosol mixing ratio (MR) fields obtained in near real time from CAMS are used to calculate the CCN. Three species of sea salt and the sulphate have been employed. It will be shown that the introduction of the aerosols modify the precipitation and the cloud cover with some positive effects in the case studied.

2 Obtaining CCN from CAMS aerosol mixing ratio

Inclusion of Aerosol Mixing Ratio Fields in Harmonie-Arome

Aerosol mixing ratio fields are going to be extracted from CAMS and assimilated inside HARMONIE-AROME. On the Web page of the ECMWF it is said about CAMS that “*The atmospheric composition outputs from the IFS are released as CAMS Global near-real-time data. As of May 2017 the horizontal resolution of the CAMS Global data is ~40 km (T511L60). Output data is available at a 3-hour intervals.*”. Three species of sea salt and one of sulphate are extracted from CAMS outputs and are included in the first guess and the Boundary conditions files for the use in HARMONIE-AROME (table 1).

Table 1: *Aerosol fields from CAMS*

Name	Short Name	Units	Parameter ID
Sea Salt Aerosol (0.03 – 0.5 μm) MR	aermr01	kg kg-1	210001
Sea Salt Aerosol (0.3 – 5 μm) MR	aermr02	kg kg-1	210002
Sea Salt Aerosol (5 – 20 μm) MR	aermr03	kg kg-1	210003
Sulphate MR	aermr11	kg kg-1	210011

The rest of the atmospheric fields are obtained from the High Resolution IFS. As the resolution of CAMS outputs and the HRES IFS are different, first of all both are interpolated separately to the grid of HARMONIE-AROME and afterwards it is needed to do a blending of the files obtained from both sources to get the definitive files.

The aerosol mixing ratio fields are advected by the dynamics of the model. It must be remarked that no sources or sinks are considered in this first attempt, so the aerosols won't be washed out by the rain and there will be differences between the mixing ratio fields advected in HARMONIE-AROME and

the fields given by CAMS. To illustrate these differences in figure 1 it is shown the sea salt mixing ratio from CAMS and at same moment, but after 12 hour integration, from HARMONIE-AROME. The red spot on the right image shows a high concentration of aerosol that doesn't appear on the left image where it was probably washed out by rain.

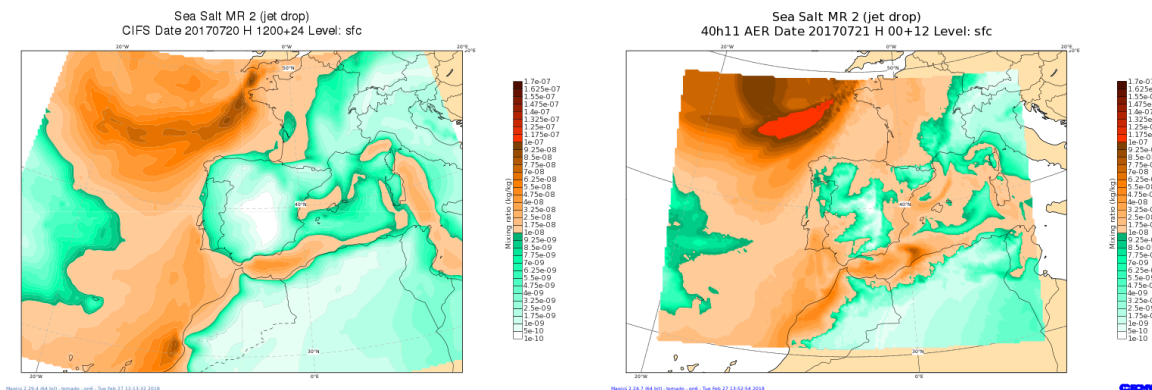


Figure 1: Sea salt mixing ratio from CAMS (left) and from HARMONIE-AROME after 12 hours integration (right)

Conversion of MR to Number of Cloud Condensation Nuclei

To convert the mixing ratio fields of the aerosols to number concentration we apply the formula:

$$Q_s = \frac{\rho_s}{\rho_{air}} = \frac{N_s}{V} \frac{4\pi}{3} \mu_s \langle r_s^3 \rangle \frac{1}{\rho_{air}}$$

where Q_s is the mixing ratio of the aerosol type 's'; ρ_s , the aerosol density; ρ_{air} , the density of the air, N_s , the number of condensation nuclei, μ_s , mass density of the aerosol; $\langle r_s^3 \rangle$, mean value of the cubic radius of aerosol particles.

In order to calculate the mean value of the cubic radius mean it is needed to assume a size distribution for the aerosols. It is supposed a log normal size distribution for each type of aerosol (figure 3).

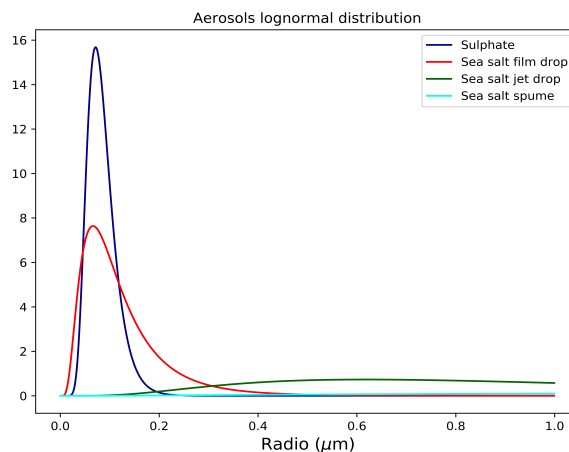


Figure 2: log normal size distributions for the three sea salt species and the sulphate

The parameters of the log normal size distribution and the mass density for each species of aerosol are given in table 2.

Table 2: Density and log normal size distribution parameters.

Name	Density (kg m ⁻³)	Rg (μm)	Sigma,σ	Mean cubic r. (kg m ⁻³)
Sea Salt Aerosol (0.03 – 0.5 μm)	1182	0,1	1,9	6,39E-021
Sea Salt Aerosol (0.3 – 5 μm)	1182	1	2	8,69E-018
Sea Salt Aerosol (5 – 20 μm)	1182	6	3	4,93E-014
Sulphate	1600	0,08	1,4	8,52E-022

An example of obtaining concentration number of condensation nuclei from mixing ratio for sulphate aerosols is shown in figure 3.

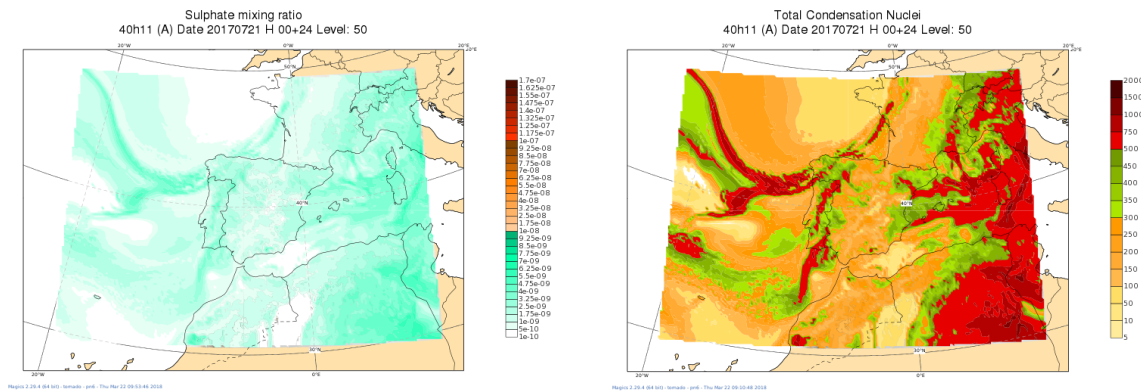


Figure 3: Sulphate mixing ratio on level 50 of HARMONIE-AROME model for 21/07/2017 and forecast length +24 (on the left panel) and Condensation nuclei concentration (in cm⁻³) for the same level, date and forecast length (right panel).

Cloud Condensation Nuclei

Once the number concentration of condensation nuclei is known, it must be obtained the cloud condensation nuclei number. The classical way is through the Twoney approximation, but, in this case, a much simple approximation has been applied. A supersaturation maximum has been calculated depending on the water vapour and the cloud water:

$$S_{max} = \frac{(r_v + r_c / clf) * P}{\epsilon \epsilon_s}$$

From the Kohler curve, depending on the characteristics of the aerosol and the radius of it, there is a critical supersaturation that, once it is reached, the aerosol can be considered activated. It has been considered that those nuclei whose critical supersaturation is lower than the supersaturation maximum are activated and are taken into account in the microphysical parametrizations. The number of activated condensation nuclei can be obtained easily from the log normal size distribution.

$$n_{s,act} = \int_{r_{s,Smax}}^{\infty} n_s(\ln r) \frac{dr}{r} = \frac{n_{s,tot}}{2} \left[1 - \operatorname{erf} \left(\frac{\ln(r_{s,Smax} / R_{g,s})}{\sqrt{2} \ln(\sigma_{g,s})} \right) \right]$$

where $n_{s,tot}$ is the concentration number of condensation nuclei and $r_{s,Smax}$ the radius for the aerosol for which the critical supersaturation is equal to the supersaturation maximum (it can be obtained from kohler formulas).

In figure 4 it is shown the supersaturation maximum calculated for the model level 50 for the same date and forecast length than in figure 3 and it is also shown the concentration number of activated nuclei.

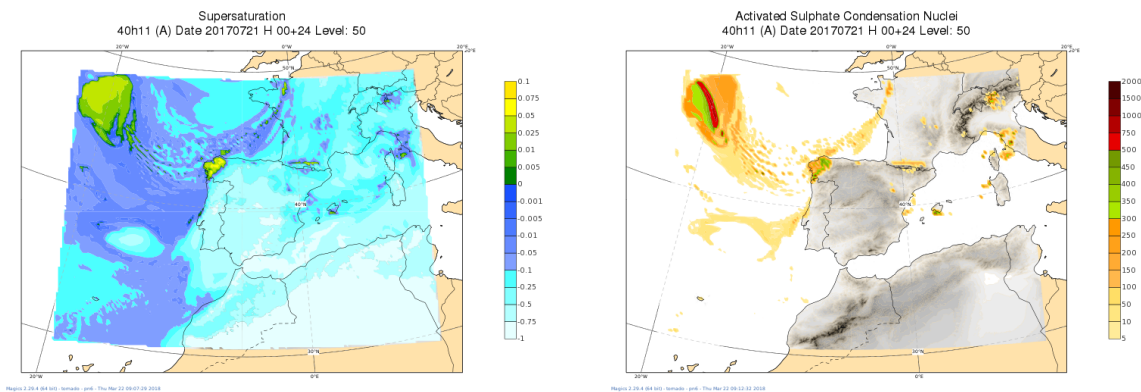


Figure 4: Supersaturation maximum (left) and activated sulphate condensation nuclei (right). Same date as in figure 3.

3 Case study

In this case of May 18th 2017, the Iberian Peninsula was under the influence of a through. There was rain in north east of the peninsula. Two HARMONIE-AROME, version 40h1.1, experiments have been run: a reference with no modification and another one with the CAMS aerosol.

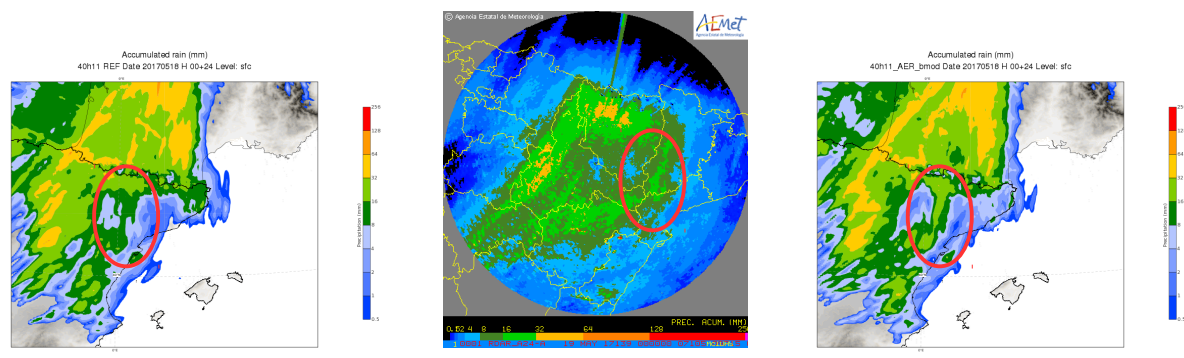


Figure 5: On the left image it is shown the accumulated precipitation in 24 hours forecasted by the reference model on the NE of the Peninsula, the same for the model modified to get CAMS aerosol on the right and the accumulated precipitation obtained from the RADAR of Zaragoza in the centre. (Date: 18/05/2017)

In figure 5 it is shown the accumulated precipitation in 24 hours for the reference model and for the model with CAMS aerosols, compared with the RADAR of Zaragoza. It can be observed a band of precipitation from north to south in the centre of the image that matches better for the experiment with CAMS aerosol than for the reference experiment.

There is another interesting result concerning the low clouds. It has been observed occasionally that the model gives more low clouds over the Mediterranean sea than expected. When the CAMS aerosol are used, the cloud cover is reduced over the Mediterranean. Probably a more realistic CCN helps to avoid this problem (figure 6). It was also noticed that light precipitation over the Mediterranean sea disappeared

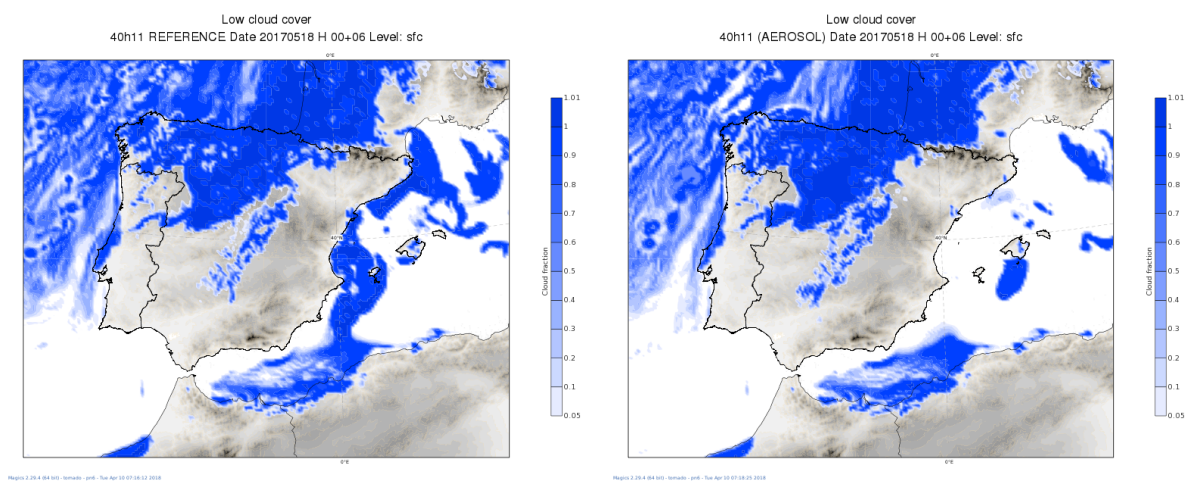


Figure 6: On the left image it is shown the low clouds for the reference experiment and on the right image for the one using CAMS outputs. (Date: 18/05/2017, forecast length H+6)

4 Conclusions

The concentration number of cloud condensation nuclei is obtained from the aerosol fields from the CAMS data and used in the microphysical parametrization schemes of HARMONIE-AROME (autoconversion, cloud droplet sedimentation and collision of cloud liquid). The mixing ratio fields are advected in HARMONIE-AROME by the dynamics, there is a lack of sources and sinks, but still, better results might be expected than using constant values.

In the case study, it was noticed that light precipitation over the Mediterranean sea disappeared. It seems that the intensity of the maximum of precipitation is reduced, but not by default. And it is shown a positive impact in the 24 accumulated precipitation.

Concerning the low clouds, not so much fake low clouds over the sea are formed in the case study when the number of condensation nuclei from CAMS is considered showing a better agreement with the observation.

A next step will be the inclusion of near real time aerosol fields from CAMS in the radiation scheme.

5 References

<https://software.ecmwf.int/wiki/display/CKB/What+is+the+IFS>

Mocrette et al., 2009. Journal of Geophysical Research. Aerosol analysis and forecast in the European Centre for Medium-Range Weather Forecast Integrated Forecast System: Forward modeling.

B. Vié et al., 2016. Geosci. Model Dev. LIMA (v1.0): A quasi two-moment microphysical scheme driven by multimodal population of cloud condensation and ice freezing nuclei.

Ghan et al., 1998. Journal of Atmospheric Science. Competition between Sea Salt and Sulfate Particles as Cloud Condensation Nuclei.

Verification and Quality Assurance in HIRLAM-C 2018: - Status and Outlook -

Bent Hansen Sass

1 Introduction

The work associated with Limited Area Models (LAMs) in numerical weather prediction is normally first of all devoted to develop setups which can be shown to provide quality improvements in a general sense relative to a global model providing the lateral boundary conditions. It is also relevant to show that the model setup developed is competitive to alternative model systems available for the area of interest.

In order to continuously to develop the model system further it is necessary to develop a suitable framework for diagnosing model deficiencies. It needs to be sufficiently advanced to gain insight to relevant aspects of atmospheric modelling. In addition, it is relevant to demonstrate and communicate model skills and limitations to the users of the model, e.g. duty forecasters. In section 2 two figures are presented which show respectively a multi-year development trend of 2m temperature as measured by bias and rmse valid for a Finnish station list, and an evolution of 2m relative humidity for a station list of Scandinavia in runs executed at MetCoOp. The former shows a clear improvement since 2009. The latter reveals a systematic annual cycle in bias of 2m relative humidity.

These results obtained from the MONITOR verification package is based on a point to point verification between forecast and observation. This methodology, however, has some limitations when verifying high resolution models, e.g. due to the so-called 'double penalty issue' (ref. [2, 3, 4])

As a consequence the spatial verification methods have become essential. The common ALADIN-HIRLAM verification package HARP [1] has recently been developed to include spatial verification methods.

A general challenge in recent years relates to the fact that normally the number of model grid points in high resolution models is much larger than the number of traditional observations in the model domain. This is not optimal. Fortunately new types of observations emerge in the context of BIG data. Pressure measurements from mobile phones is one such example. A PhD study in DMI investigates the potential of assimilating such data in Harmonie-Arome. The preliminary results are promising showing positive impact of these data in case studies of precipitation forecasts. The data received are numerous, e.g. about 2 million pieces of data in less than two weeks. Some results are displayed in Fig.3. Careful quality control and preprocessing is needed to use these data in NWP.

Finally, the Table shows the envisaged type of verification in the future needed to properly investigate the properties and potential of an NWP model.

2 Multi-year verification trends

It is relevant to diagnose multi-year trends in the quality of NWP, in this case Harmonie-Arome. One such example has been provided by FMI (fig1) showing bias and rmse of 2 metre temperature for Finnish stations. It is clear that this parameter has improved since the start of the systematic

verification in 2009. It is also important to diagnose systematic errors, e.g. repeated on an annual scale. This is shown in Fig2. showing the 2m relative humidity for Scandinavia station list. It is evident that a positive bias has developed annually during Spring, apparently linked with the melting season (snow and ice).

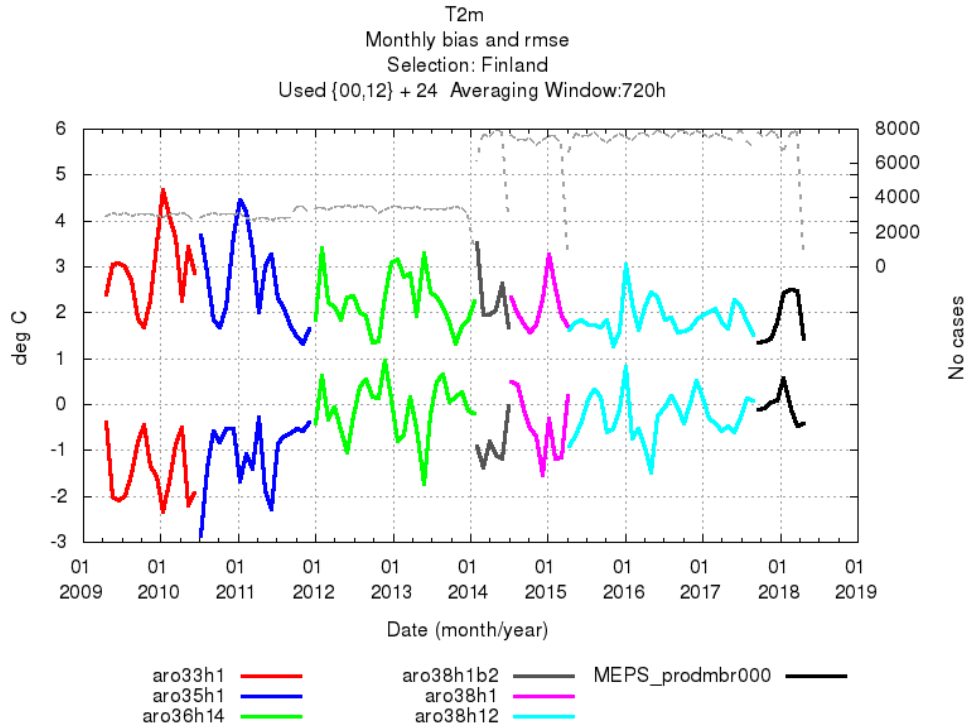


Figure 1: Bias and RMSE since 2009 of 2m temperature (see legends) for Finnish stations

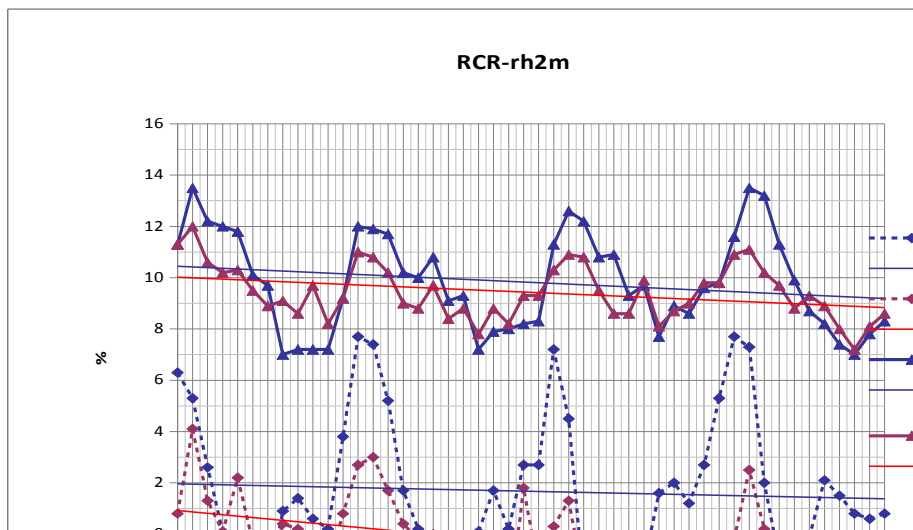


Figure 2: Monthly values of bias and standard deviation of 2m relative humidity (Scandinavia station list) since 2014. The annual cycle in bias is clear.

3 Challenges and opportunities in high resolution NWP

High resolution NWP requires high resolution observations for proper verification, if possible reliable analyses in the same grid as the model. The limitations by traditional point verifications are linked with the 'double penalty' issue. Fortunately the huge amount of data coming up, e.g. in the context of measurements from mobile phones, has a potential to alleviate the problem of insufficient amount of verification data. However, in order to utilize new data sources, careful quality control methods needs to be implemented. Fig. 3 shows a map of Denmark with example of measured surface pressure from mobile phones.

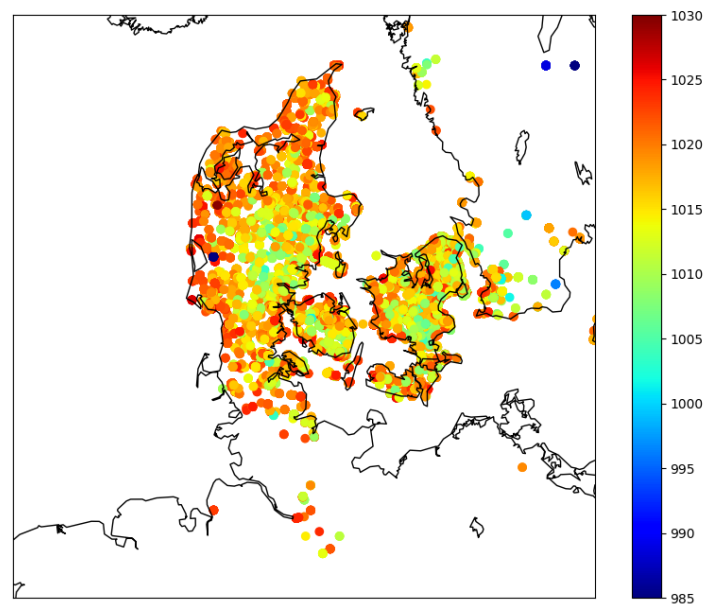


Figure3: BIG data from mobile phones : Collection of surface pressure data from a setup at DMI (PhD student Kasper Hintz). About 2 million data from Denmark collected in less than 2 week , implying a huge amount of data for quality control and surface analysis

Some of the new groups of verification schemes are illustrated schematically in the Table below. The possible evolution towards 3-dimensional verification with spatial aspects included is indicated in the last column. Also time window aspects may be envisaged. It is hoped that HARP verification will evolve with several of the new types of schemes in the future.

TABLE : Envisaged new types of verifications in the future

Forecasted \ Observed	Set of forecasts at irregular observation points	1-dim grid of forecast verification	1-dim fuzzy forecast verification , spatial or in time, pointwise	2-dim grid of forecast verification	2-dim fuzzy verification , spatial structures	3-dim grid of forecast verification	3-dim fuzzy verification, spatial or in time in each point.
Set of irregular observation points, e.g. station list	Traditional point to point verification	-	Example: Fuzzy verification in time	-	-	-	New 3-dimensional verification schemes
1-dim (regular) grid of observed or analyzed values	-	Example: Vertical profile line of data or selected points	-	-	-	-	New 3-dimensional verification schemes
2-dim (regular) grid of observed or analyzed values	-	-	-	Traditional point to point verification	FSS, SWS ,SAL spatial verification (ref. [5,6,7])	-	New 3-dimensional verification schemes
3-dim (regular) grid of observed or analyzed values	-	-	-	-	-	Traditional point to point verification	New 3-dimensional verification schemes

4 References

- [1] HARP v2: Documentation, (www.hirlam.org), by Andrew Singleton (Met.Norway) and Alex Deckmyn (RMI).
- [2] <http://www.cawcr.gov.au/projects/verification/>
Theme: Forecast Verification methods Across Time and Space Scales , 7th International Verification Methods Workshop (WWRP/WGNE Joint Working Group on Forecast Verification Research)
- [3] Gilleland, E., Ahijevych, D.A., Brown, B.G., Ebert, E., 2010: Verifying forecasts spatially, BAMS 1365-1373
- [4] Murphy, A.H., 1993: What is a good forecast? An essay on the nature of goodness in weather forecasting. Wea. Forecasting, 8, 281-293.
- [5] Roberts , N.M., and Lean, H.W., 2008:
Scale –selective verification of rainfall accumulations from high-resolution forecasts of convective events . Mon. Wea. Rev., 136, 78-97
- [6] Sass, B.H., and Yang, X, 2012: A verification score for high resolution NWP: Idealized and pre-operational tests , HIRLAM Tech. Rep. no. 69, 28pp [available from www.hirlam.org]
- [7] Wernli, H. , Paulat, M., Hage, M. and Frei, C., 2008:
SAL- A Novel Quality Measure for the Verification of Quantitative Precipitation Forecasts , Mon. Wea. Rev. , 136, 4470 – 4487

AROME-SURFEX orographic parametrizations

Laura Rontu, Alexandre Mary, Clemens Wastl, Yann Seity

1 Introduction

Within AROME-SURFEX, orographic radiation parametrizations (ororad) are available in order to account for the slope, shadow and sky view effects on solar and terrestrial radiation at the surface. A version of ororad has been introduced to the ALADIN-HIRLAM cycle43 within SURFEX 8, following Wastl et al. (2015); Rontu et al. (2016); Senkova et al. (2007). To account for the impact of the subgrid-scale orography on the surface layer momentum fluxes, a new scheme (orotur) has been added to HARMONIE-AROME-SURFEX.

In principle, handling of slope effects on radiation is a simple trigonometric exercise. The main challenge is in description of the subgrid-scale orography properties. Three main principles apply: 1) Average the fluxes, not the orography. For example, for the net SW radiation coefficients have been derived to multiply the downwelling direct and diffuse radiation fluxes based on the fine-resolution digital elevation model (DEM) data. 2) Mind the physics of the scales. The resolution of available DEM data is much higher than that of the AROME-SURFEX. On the other hand, some parameters like the local horizon angles and the integrated sky view factor are non-local, possibly representing the area of several resolved grid squares. On the slopes, vegetation and land surfaces vary, possibly in a still smaller spatial scale, and are treated by the tiling approach. 3) Keep the treatment of orographic effects as simple as possible. Statistics of the surface elevation do not depend on time so the main parameters can be precalculated. It may be possible to apply some parametrizations as postprocessing, not necessarily during the model's time integration.

Table 1. Orography-related parameters within grid resolution

parameter	description	unit	usage
$H_{\Delta x}$	mean surface elevation	m	dynamics
σ_{sso}	subgrid-scale scale standard deviation	m	momentum
s_{sso}	mean subgrid-scale slope angle	rad	not applied
$h_{m,i}$	slope angle in direction i	rad	radiation
f_i	fraction of slope in direction i	-	radiation
$h_{h,i}$	local horizon in direction i	rad	radiation
δ_{sv}	sky view factor	-	radiation
δ_{sl}	slope factor	-	radiation
δ_{sh}	shadow factor	-	radiation

Figure 1: Oroparameters for radiation: the grid-scale sky view, slope and shadow factors (yellow shading) are based on the directional building blocks of slope elevation angles, fraction of slopes and local horizons (blue shading). Parameters related to momentum fluxes are shown without shading.

The impact of the smallest-scale orography features on the surface layer momentum fluxes requires information about the fine-scale variation of the surface elevation that can be derived from digital elevation model (DEM)

data like SRTM (Jarvis et al., 2008). In SURFEX, suitable statistical variables are already available: the standard deviation or subgrid-scale slope angle, which is derived as an eigenvalue of the orography gradient correlation tensor, see e.g. Baines (1998). In the literature (Helbig et al., 2017) it has been suggested to use sky view factor as a basic variable also for momentum flux parametrizations.

2 Ororad: calculation of slopes and horizons

2.1 Slope elevation angle and azimuth

Ororad parametrizations utilize directional fractions of the subgrid-scale slopes (Senkova et al., 2007). Based on fine-resolution source DEM, for each grid square the fraction of northern, north-eastern etc. slopes and the mean slope angle in each sector is derived, see Table 1. Three different approaches for derivation of these variables have been tried: 1) external, using Geospatial Data Abstraction Library (GDAL, 2014), 2) using PGD tools for calculation of the orography gradient correlation tensor for subgrid boxes as suggested by A. Mary, 3) applying PGD tools to grid-scale surface elevation. Figure 2 illustrates the difference for south-eastern slopes over the Sochi olympics domain over the Caucasian mountains. It is obvious that the grid-scale approach (Figures 2c and 2f) leads to binary fractions and significantly smoothed slopes due to loss of subgrid-scale information. The other two approaches lead to more similar results. The subgrid tensor approach within PGD is consistent with the rest of the model and does not require external preprocessing. It is thus applicable for operational usage within SURFEX after further testing and comparisons over relevant mountain areas.

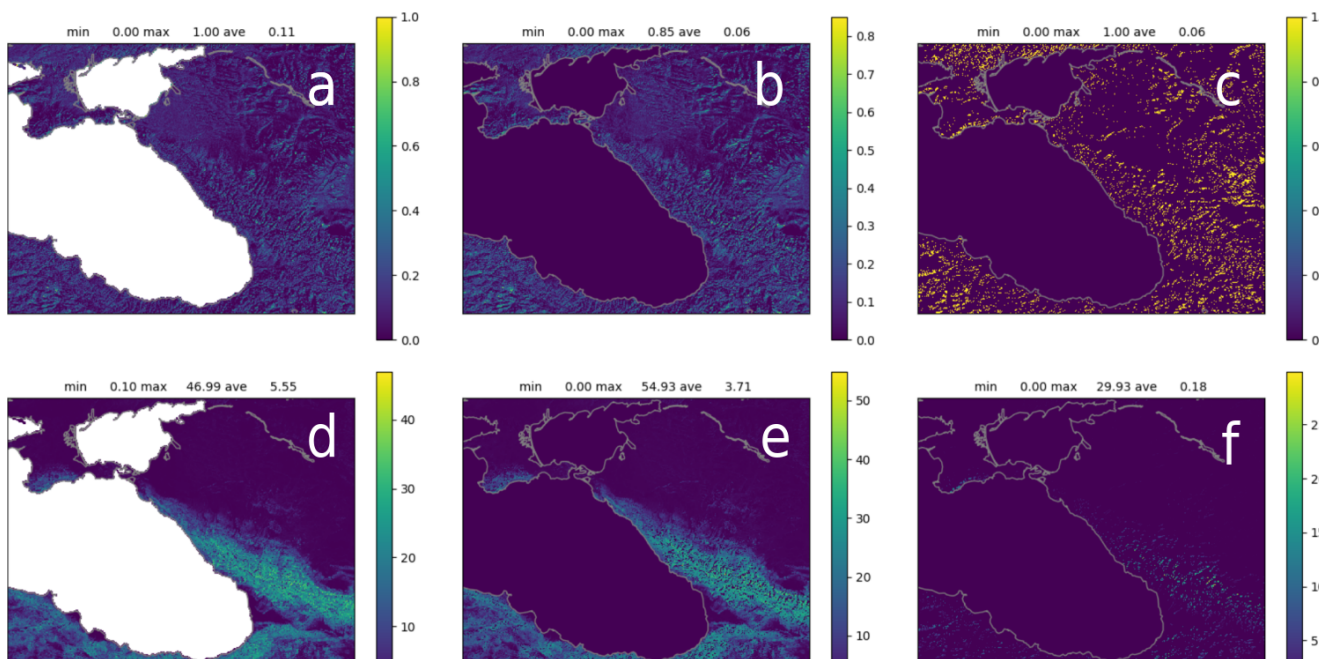


Figure 2: Fraction of SE slopes (0 ... 1, upper panel) and their mean maximum slopes (degrees, lower panel) prepared by three different methods: external (a,d), PGD subgrid tensor approach (b,e) and PGD grid-scale approach (c,f). Averages, minima and maxima are shown in the subtitles. Note the different colour scales.

2.2 Local horizon angle and sky view factor

There exist several ways to approximate the local horizon angles (LHA) for all directions around a point. They lead to different results, and also to different sky view factor, which is defined as integrated over 360 degrees LHA (Rontu et al., 2016). In principle, it is necessary to take into account the slope of the point for which the local horizons are calculated (Manners et al., 2012), something that was omitted by Senkova et al. (2007). The question remains how to define this slope optimally to represent conditions in a grid-square.

It was shown by Rontu et al. (2016) that local horizon was accurately represented for the valley St. Leonhard in Pitztal, Austria, when calculated in a SRTM gridpoint by using external programs. Their result is shown in Figure 3 together with values averaged over the 2.5 km grid-square around St. Leonhard. The grid-average values indicate larger sky view, thus smaller impact on LW and diffuse SW radiation fluxes. In this comparison, slope of the central point was not taken into account and the external calculations were applied in the SRTM grid (horizontal resolution 3") while the average was done by PGD for the AROME grid.

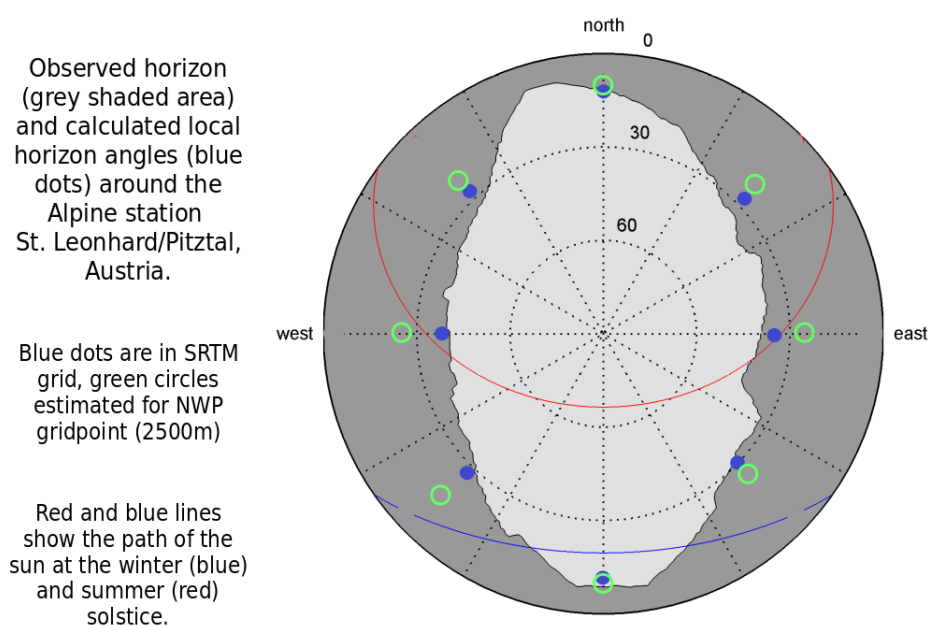


Figure 3: Local horizon angles for St. Leonhard.

3 Ororad: sensitivities and impacts

Figure 4 shows examples of ororad impact in MUSC single-column experiments where different ways for calculation of the slopes and horizons were applied to provide the input. An additional experiment using modified microphysics parametrizations (LOCND2=.false.) is also shown. The results are compared with the reference experiment with no ororad parametrizations and LOCND2=.true. Input atmospheric and surface data were picked from 3D experiments over Sochi Olympic area, station Krasnya Polyana (see Rontu et al. (2016)) at the 8th of February 2014. These MUSC experiments indicate possible sensitivities within a simplified setup, not comparable to observations.

In the experiments, the input local horizons and sky view factor were more different than the slope angles. The impact of all experiments to early morning temperatures in the clear-sky conditions was similar, showing a couple of degrees warmer temperature at the location which was exposed to sun earlier than the assumed

flat grid-square would have been (Figures 4a and 4b). In the afternoon and during the next night, temperature differences grew larger. The experiment 43seocf, with modified microphysics, showed results closest to the NO-ORO reference and quite different from the experiment 43se, which however used the same slopes and horizons as 43seocf. In the reference experiment the sky stayed clear almost till the next morning while in the ororad experiments, depending on the microphysics, a shallow low cloud tended to form and dissolve (Figures 4c and 4d, cloud height checked from the experiment output). The MUSC experiments may be unrealistic, but such cloud-radiation interactions and related sensitivities to ororad parametrizations are probable also in the full 3D model runs.

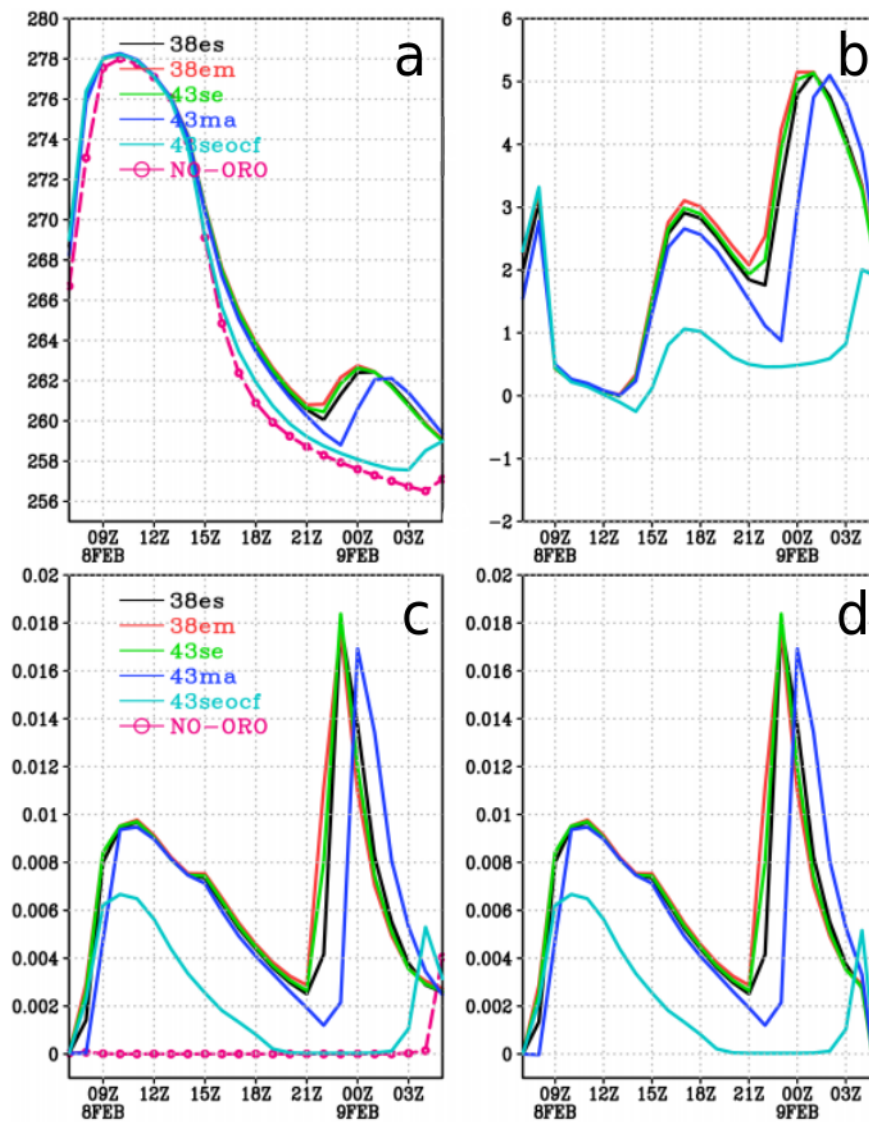


Figure 4: Impact of ororad parametrizations in MUSC experiments: surface temperature (a, b, unit K) and vertically integrated cloud water content (c, d, unit kg/m^2). On the left, time series of the variable is shown for different experiments: 38se (cycle 38, Senkova external), 38em (Manners external), 43se (cycle 43 Senkova), 43ma (Manners), 43seocf (as 43se but microphysics parametrization $\text{OCND2}=\text{false}$), NO-ORO (no ororad parametrizations applied). On the right-side figures, difference between each experiment and NO-ORO is depicted.

4 Orotur: method and variables

4.1 Parametrization of orographic effects on momentum fluxes

In the default SURFEX, various options are available for parametrization of the small-scale subgrid-scale orographic momentum-fluxes: application of the concept of orographic roughness, possibly with directional components based on Georgelin et al. (1994), or parametrization of the non-separated sheltering effect due to the airflow over hills and mountains (Wood et al., 2001) in the form suggested by Beljaars et al. (2004). In the HARMONIE-AROME-SURFEX NWP system parametrization of the vertically propagating buoyancy waves is not applied because the generation of these waves is believed to be handled by the fine-resolution nonhydrostatic dynamics of the model and their dissipation treated by the turbulence parametrizations of the model (Bougeault and Lacarrere, 1989). In ALADIN-ALARO system such parametrizations are applicable (Catry et al., 2008).

A simplified version of the HIRLAM small-scale orographic turbulence parametrization (Rontu, 2006), hereafter referred to as orotur, was tried in HARMONIE. The suggested scheme is another realization of the Wood et al. (2001) idea of handling the non-separated sheltering effect. The surface value of the subgrid-scale orographic stress $\vec{\tau}_{os}$ (horizontal momentum flux in the surface layer given in units of Pa) is related to the subgrid-scale orography variance σ_{sso}^2 , multiplied by the turbulent stress $\vec{\tau}_{ts}$

$$\vec{\tau}_{os} = C_o \sigma_{sso}^2 \vec{\tau}_{ts}, \quad (1)$$

where C_o is the subgrid-scale orography drag coefficient and $\vec{\tau}_{ts}$ denotes the turbulent surface stress $\vec{\tau}_{ts} = \overline{\rho_s w' v'}$. ρ_s stands for the air density at the surface, overline denotes average over a gridsquare and w' and v' are deviations of the vertical and horizontal wind components from the average, respectively. Finally, the total stress $\vec{\tau}_{tot}$ is obtained as a sum of the orographic and turbulent components

$$\vec{\tau}_{tot} = \vec{\tau}_{os} + \vec{\tau}_{ts} = (1 + C_o \sigma_{sso}^2) \vec{\tau}_{ts} \quad (2)$$

The coefficient $C_o = C_{oo} V_{oo}^2 / (V_{nlev}^2 + V_{oo}^2)$, where V_{nlev} denotes the lowest model level wind speed, $C_{oo} = \alpha / \Delta x^2$, α and V_{oo}^2 are tunable constants (in the first trials set to 100 m² and 8 m²/s², respectively) and Δx denotes the model's horizontal resolution (grid size in metres). The idea behind the wind scaling was to increase the drag on the weakest winds by accounting for the surface layer wind shear. Inclusion of Δx^2 -scaling was done in order to roughly relate the orography variations to the steepness of subgrid-scale slopes in each gridsquare.

There are three main differences between the simplified orotur and the original HIRLAM scheme suggested by Rontu (2006). First, the parametrization is now entirely based on the subgrid-scale standard deviation (σ_{sso} , see Table 1), instead of the filtered smallest-scale mean slope used by HIRLAM. Second, the parametrization modifies the surface-layer turbulent momentum fluxes, which are further passed as lower boundary condition to the turbulence parametrizations above the surface layer. This was done instead of direct modification of the lower troposphere wind tendencies in the momentum equations of the model. The three-dimensionality and stability-dependency of the orographic stress is thus realized via the vertical diffusion (turbulence) parametrizations only. Also, the turbulent and orographic stress vectors $\vec{\tau}_{os}$ and $\vec{\tau}_{ts}$ are assumed parallel. However, the default classical concept of orographic roughness (Mason, 1985; Georgelin et al., 1994) is not needed anymore. Third, the drag coefficient was made dependent of the lowest model level wind velocity and also on the model resolution (Equation 2). The second and third modification were partly motivated by similar approximations used in the operational HIRLAM (v.7.4) model (Rontu, 2007).

4.2 Impact of the momentum flux parametrizations

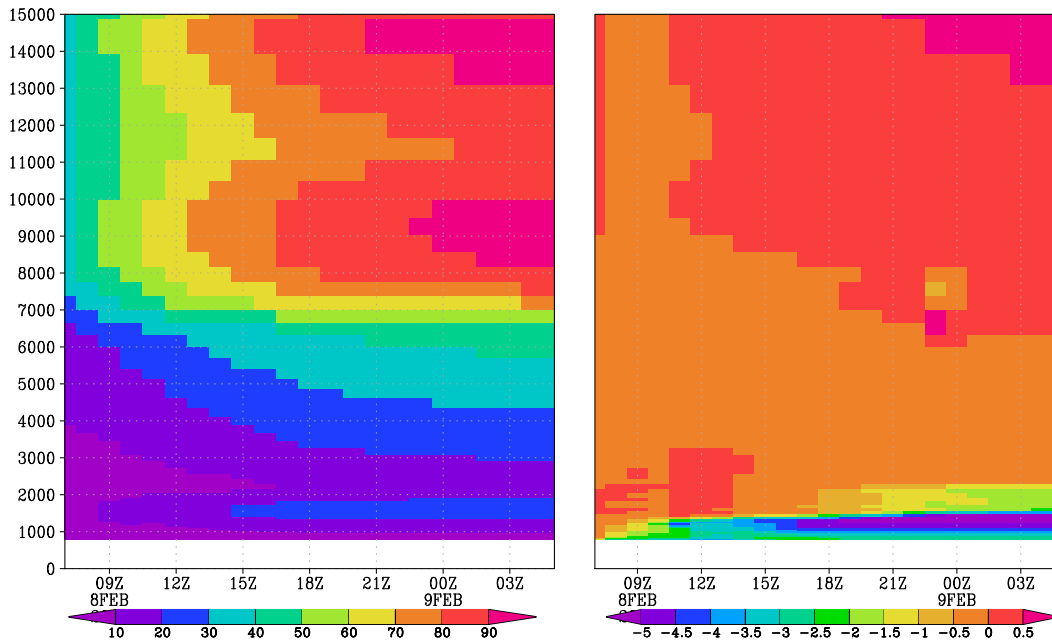


Figure 5: Wind speed (m/s) as a function of height (m, y-axis) and time (x-axis) for the station Krasnya Polyana from MUSC experiments initiated at 06 UTC the 8th of February 2014 with enhanced wind forcing. Values of the enhanced experiment on the left, difference from the reference (no orotur) on the right.

Properties of the suggested orotur parametrizations were studied already earlier in MUSC experiments (cycle38). We then increased artificially the weak input wind speed by 10 m/s at 23 lower tropospheric levels and forced the initial weak wind profile towards the modified profile during the single-column time integration. The enhancement led to an increase of the near-surface turbulent kinetic energy and formation of a low-level jet in the lowest kilometre of the simulated boundary layer, both with and without the orotur parametrizations.

Different values of the coefficients C_{oo} and V_{oo}^2 (Equation 1) were tried and the results diagnosed using time-height cross-sections of wind and turbulent kinetic energy (TKE) as well as the friction velocity at the top of the lowest model layer. Modification of the coefficient values in combination initial weak wind profile led only to a small decrease of the lowest level wind speed with some 0.2 m/s. When enhanced forcing was applied, the wind speed difference between the orotur and reference experiment doubled, still showing only a minor effect. With a ten-fold value $C_{oo}=1000 \text{ m}^2$, the maximum wind difference reached -2.9 m/s at the level of the low level jet maximum. Finally, Figure 5 shows an example of the wind evolution in a case where C_{oo} was set to 1000 m^2 and V_{oo}^2 to $64 \text{ m}^2\text{s}^{-2}$. In this case, the reduction increased for the strongest winds. Correspondingly, the maximum lowest level TKE values were doubled from 1.1 to $2.3 \text{ m}^2\text{s}^{-2}$ as compared to the case where orotur parametrizations were not applied. Also the lowest model level temperature was affected by the increased turbulence, increasing by up to 1.5 degrees.

We can conclude that the coefficients C_{oo} and V_{oo}^2 allow physically reasonable way of tuning the low level turbulence and wind in the boundary layer over the rough terrain as a function of the orography standard deviation (Equation 1) in each gridbox. However, more testing against representative low level wind observations is needed to optimise this tuning for the three-dimensional forecast model.

5 Next steps

To finalize the implementation of ororad and orotur parametrizations it is necessary to check and optimize the suggested code for SURFEX v.9 and the next cycles of ALADIN-HIRLAM. Specific tasks for ororad and orotur include:

ORORAD

- Compare external v.s. subtensor slopes, local horizon and skyview factor
- Perform model-observation intercomparison over Alps using global SW radiation and surface temperature observations.

OROTUR

- Continue testing and tuning, choose an optimal basic orovvariable for orographic momentum flux parametrizations.
- Study the interactions with surface layer turbulence parametrizations and their roughness definitions.
- Find an area with representative wind observations, downscale model wind towards point observations and perform model-observation intercomparisons.

References

- Baines, P. (1998). *Topographic effects in stratified flows* (Cambridge University Press)
- Beljaars, A. C. M., Brown, A. R., and Wood, N. (2004). A new parametrization of turbulent orographic form drag. *Q. J. R. Meteor. Soc.* 130, 1327–1347
- Bougeault, P. and Lacarrere, P. (1989). Parameterisation of orography-induced turbulence in a meso-beta scale model. *Mon. Wea. Rev.* 117, 1872–1890
- Catry, B., Geleyn, J.-F., Bouyssel, F., Cedilnik, J., Brožkova, R., Derkova, M., et al. (2008). A new sub-grid scale lift formulation in a mountain drag parameterisation scheme. *Meteorologische Zeitschrift* 17, 193–208
- GDAL (2014). Geospatial data abstraction library. <http://www.gdal.org>
- Georgelin, M., Richard, E., Petitdidier, M., and Druilhet, A. (1994). Impact of subgrid-scale orography parametrization on the simulation orographic flows. *Mon. Wea. Rev.* 122, 1509–1522
- Helbig, N., Mott, R., van Herwijnen, A., Winstral, A., and Jonas, T. (2017). Parameterizing surface wind speed over complex topography. *J. Geophys. Res. Atmos.* 122, 651—667. doi:10.1002/2016JD025593
- Jarvis, A., Reuter, H. I., Nelson, A., and Guevara, E. (2008). Hole-filled SRTM for the globe version 4
- Manners, J., Vosper, S. B., and Roberts, N. (2012). Radiative transfer over resolved topographic features for high-resolution weather prediction. *Quarterly Journal of the Royal Meteorological Society* 138, 720–733. doi:10.1002/qj.956
- Mason, P. J. (1985). On the parameterization of the orographic drag. Proc. Seminar on Physical parametrization for Numerical Models of the Atmosphere, ECMWF
- Rontu, L. (2006). A study on parametrization of orography-related momentum fluxes in a synoptic-scale NWP model. *Tellus* 58A, 68–81

- Rontu, L. (2007). *Studies on orographic effects in a numerical weather prediction model*. Tech. Rep. 63, Finnish Meteorological Institute Contributions. Available as <http://urn.fi/URN:ISBN:978-952-10-4184-6>
- Rontu, L., Wastl, C., and Niemelä, S. (2016). Influence of the details of topography on weather forecast – evaluation of harmonic experiments in the sochi olympics domain over the caucasian mountains. *Frontiers in Earth Science* 4. doi:10.3389/feart.2016.00013
- Senkova, A., Rontu, L., and Savijärvi, H. (2007). Parametrization of orographic effects on surface radiation in HIRLAM. *Tellus* 59A, 279–291
- Wastl, C., Mary, A., Seity, Y., Rontu, L., and Wittmann, C. (2015). Parameterization of orographic effects on surface radiation in AROME-SURFEX. *ALADIN-HIRLAM Newsletter* , 81 – 82. Available as <http://www.umr-cnrm.fr/aladin/IMG/pdf/nl5.pdf>
- Wood, N., Brown, A. R., and Hewer, F. E. (2001). Parametrizing the effects of orography on the boundary layer: An alternative to effective roughness lengths. *Q. J. R. Meteor. Soc* 127, 759–777

Cycles, mitraillette and the like ...

Claude FISCHER

1 Introduction

This short note provides an overview about code evolution, cycles, OOPS along the lines of my talk at the Toulouse All Staff Meeting. Contributions by A. Mary, K. Yessad, R. El Khatib and P. Saez have been much appreciated. Part of this information dates back to the IFS/Arpège coordination meeting held in Toulouse on 19 March, and the author thanks the colleagues from ECMWF who provided the relevant contributions for that meeting.

2 R&D cycles

CY45 : declared on 28 June 2017

- Significant re-factoring for OOPS !
 - ▶ Obs operators [CY43-CY44-CY45]
 - ▶ ODB interfaces [CY45]
 - ▶ MODEL object in IFS codes [CY45]

CY45T1 : declared on 24 January 2018

- Updates for Alaro-1 ; for Bator with Hirlam
- Tests : bug in IDFI, norms of Alaro under investigation, Aladin+Surfex test broken
- and many more contributions, refer to my document for the LTM and HMG-CSSI meetings
- No DA tested yet

CY46 : declared on 10 April 2018

- OOPS re-factoring : VarBC, time handling step 1, LBC object, etc.
- Full-POS for OOPS : re-factoring done (interfaces & methods are working)
- same level of overall validation than CY45T1 (Alaro norms ?, no DA tested etc.)
- IDFI fixed, fixes for FP and models included (thus, code probably a bit cleaner than in CY45T1_main)
- Use ecCodes for accessing GRIB_API interfaces

CY46T0 or T1 : autumn 2018 (exact content and timing tbc)

CY47 : January-March 2019 (agreed with ECMWF)

- Robust base version for OOPS ?

CY47T1 : spring or autumn 2019

MF code versions :

- CY42_op2 : operational since 5 December 2017
- CY42_op3 : e-suite for Arome EDA (AEARO)
- CY43T2_bf : target base version for 2018 e-suite. Intensive validation effort is ongoing in order to achieve baseline validation for all Arpège and Arome confs (_bf.06 now in MF's GIT) => *at the time of writing this short note (01.06.2018), _bf.08 is available in MF's GIT and very close to the base version for MF's e-suite version.*

ALADIN export versions / HIRLAM shared versions :

- CY40T1_bf.07 : released 24 April 2017
- CY43T2_bf.xx : a test version based on _bf.04 is under evaluation by HIRLAM and in CHMI. The final export version will have $xx \geq 08$.

Note : all FLUBs (technical memoranda) of recent cycles, minutes from IFS/Arpège coordination meetings and technical videoconferences (incl. OOPS) are available at <http://www.umrcnm.fr/aladin/> (note that some pages are pwd-protected)

3 mitraille

Reminder : all namelists and protojobs now available in MF's GIT-GCO repository

■ Latest versions :

- V102017 : CY45T1
- V042018 : CY46

■ New tools in order to help get a complete and user-friendly overview of the many test results :

- Checkpack.py, ciboulette.py => details were given by Alexandre at the System WG meeting on Thursday 19 April afternoon. Refer to those minutes available from Maria Derkova (ACNA).

■ Thoughts about future evolution :

- Add elements of DA
- Add other new elements (eg PREP ?)
- Improve user-friendliness
- Extend to OOPS in due time
- Open question : use tools as a recommended or somehow compulsory step in code commitment process ?

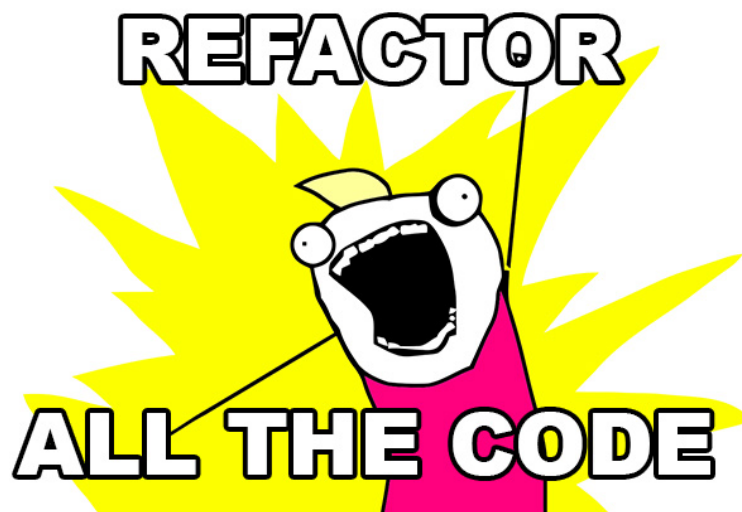
4 OOPS

■ At Project level – timing at ECMWF :

- OOPS-IFS 4D-VAR fully available in Research by end of 2018, then have staff test OOPS binaries for a long enough period in 2019
- E-suite and operations : possibly only after move of HPC Centre to Bologna (thus, rather S2/2020) unless this move slips in time

- FORTRAN code re-factoring status :
 - Significant code overhaul over [CY43-CY46], rather welcome by all involved developers and scientists
 - Remaining issues after CY46 : VarQC, all-sky radiances, c-VarBC, restart, time handling step 2 (EC) ; complete plug-in of FP in OOPS (MF) ; DFI (Aladin)
 - Technical testing and validation w/r to « classical » binaries
- Plans at MF in 2018 – 2019 – and beyond :
 - Forecast model tests (Arpège, Arome), Full-POS in various configurations
 - Some simple obs operator tests, TL/AD model tests (coll. with EC)
 - Left for after CY47 : rebuild 4D-VAR and LAM/3D-VAR prototypes, start testing with respect to « classical » VAR confs, test OOPS-FP within 4D-VAR, re-phase EnVar codes

Figure 1: a kind reminder ...



5 Outlook towards other major code changes (after OOPS)

- ATLAS will become visible in IFS codes in CY47, but not compulsory for installation (protected by pre-compile directives)
- New dynamical cores (precise implementation in IFS cycles totally open for now)
- Codes for continuous DA, for COPE
- Changes related to outcome of ESCAPE or next-ESCAPE projects ; changes coming from porting to new HPC architectures ?

6 References

Fischer, C., 2018. *Progress and plans about status of common IFS/Arpège/LAM cycles and MF operational + R&D activities*. Document 4.a of the Aladin LTM meeting on 16.04.2018, Toulouse.

Object Orientation in Post-processing

Ryad El Khatib

1 Introduction

For the past two years, the post-processing package Fullpos has been re-factored in order to be compliant with the OOPS project. The first aim was to enable the post-processing to be called from the OOPS C++ abstract layer, and beyond, to support multi-instantiation. However, for Météo-France and unlike ECMWF, a second aim is needed : a full change of resolution of a dataset must be possible within OOPS, without leaving the executable. Because of the variable mesh of the global model ARPEGE, at Météo-France we can't just truncate the spectra of fields to a lower resolution in the incremental 4D-Var incremental assimilation. This paper describes the state of the art in this matter.

2 Objects concerning the post-processing

The post-processing becomes an object, and will use other existing objects in the code. These objects are nothing but big Fortran structures, defined by large derived types. They are allocated by complex procedures called “constructors” ; and exploited by so-called “methods”. Usually the first method that should be used is an initialiser of the constructed object.

The main objects concerning the post-processing are the following ones :

- **Geometries** : define spectral and gridpoint dimensions and attributes, geometry, and orography. The constructor is `sugeometry` ; or `geometry_setup` to include the initialization of the orography.
- **Fields** : define spectral fields, grid-point upper-air fields and surface fields. The constructor is `fields_create`. The method initializing a Fields object is `read_fields`.
- **Models** : define dynamics, physics, and optional fields (GFL) attributes. The constructor is `model_create`. The method to perform a time step is `model_step`.
- **Post-processors** (Fullpos) : define the interpolators attributes, the spectral filters, etc. The constructor is `subfpos` ; the initializer (computation of interpolations weights, reading of target climatology fields) is `sufpdata`. The method for usual back-end post-processing (that creates output files) is `allfpos`.

Any program using such objects should invoke at start a start-up procedure, called `ifs_init`. That procedure contains all that is not multi-instantiable, or at least not yet : message passing initialization, spectral transforms definition, constants etc. For instance the vertical interpolator is not fully an object at this stage, so for now the vertical interpolations attributes are defined within `ifs_init`.

Note that these objects are not fully independents : a Model object needs an associated geometry ; a Fields object needs an associated geometry, and an associated model, too. These associations are materialized by pointers in the constructors of objects. Being aware of these associations, the manipulation of these objects can be made more robust ; or on the contrary more dangerous if attributes of different objects are mixed.

3 Post-processing server

The figure 1 below describes in a pictorial way how such objects can be aggregated to build a simple post-processing server, similar to the configuration 903 of the current Arpege/Arome software (the greyish pictures denote non-initialized objects).

Note that such server can be developed on top of a Fortran interface (and has been, actually, for testing purpose).

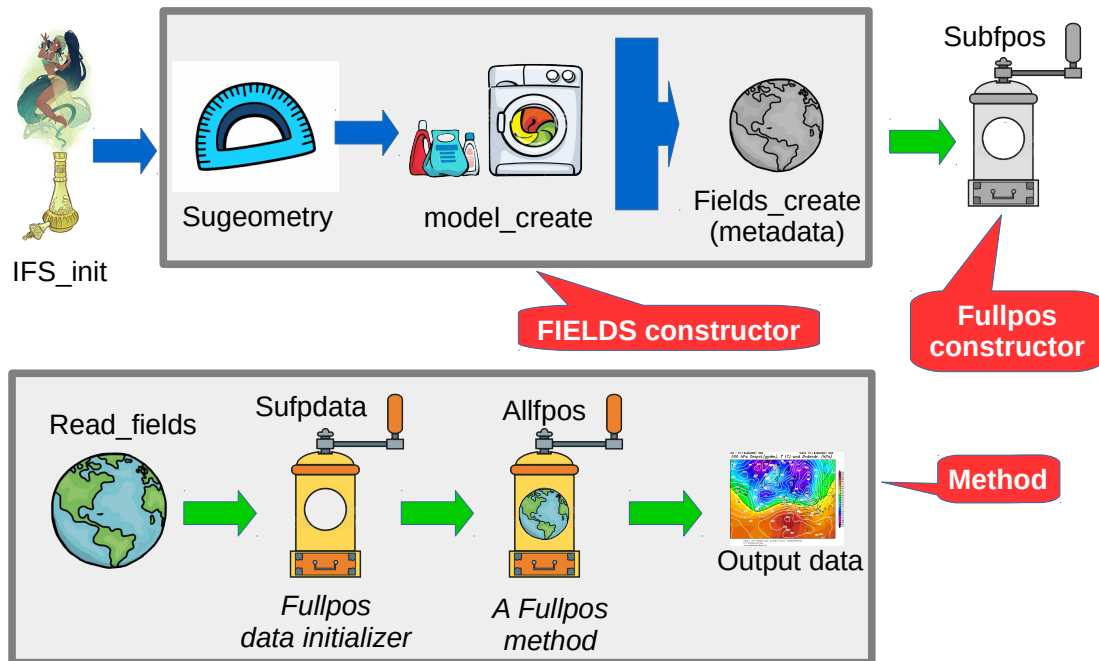


Figure 1 : a simple post-processing server

Such post-processor can be easily implemented within the forecasting model, ie after a chosen invocation of a model step.

Also a multi-post-processors server can be build, just by creating more Fullpos objects, all of them operating from the same model, model geometry and model fields.

4 Fields transformer for the 4D-Var assimilation

The context of the 4D-Var assimilation requires two reciprocal post-processors to be constructed (figure 3). As shown above, this requires two geometries, two models and two fields infrastructures. But they are all provided as existing objects in OOPS : high resolution geometry, fields, and forecasting model on one side ; low resolution geometry, fields, and minimizer on the reciprocal side. So that the construction of the two post-processors are easy.

The difficulty resides in the production of the output data, which should not be a file on disk, but a fields object. The adopted solution is schematized in the figure 2 : again, the software already provides useful objects, such as the spectral transforms package and the fields constructor. So that the operation consists in a serie of elementary post-processing requests to compute the individual gridpoint arrays of the pre-constructed target fields object ; while the spectral representation of output fields is performed by an invocation of the (target) model spectral transforms. In addition, the facility of pointer

remapping provided by the Fortran 2003 standard has been of some help to convert post-processing 2D arrays into output 3D arrays.

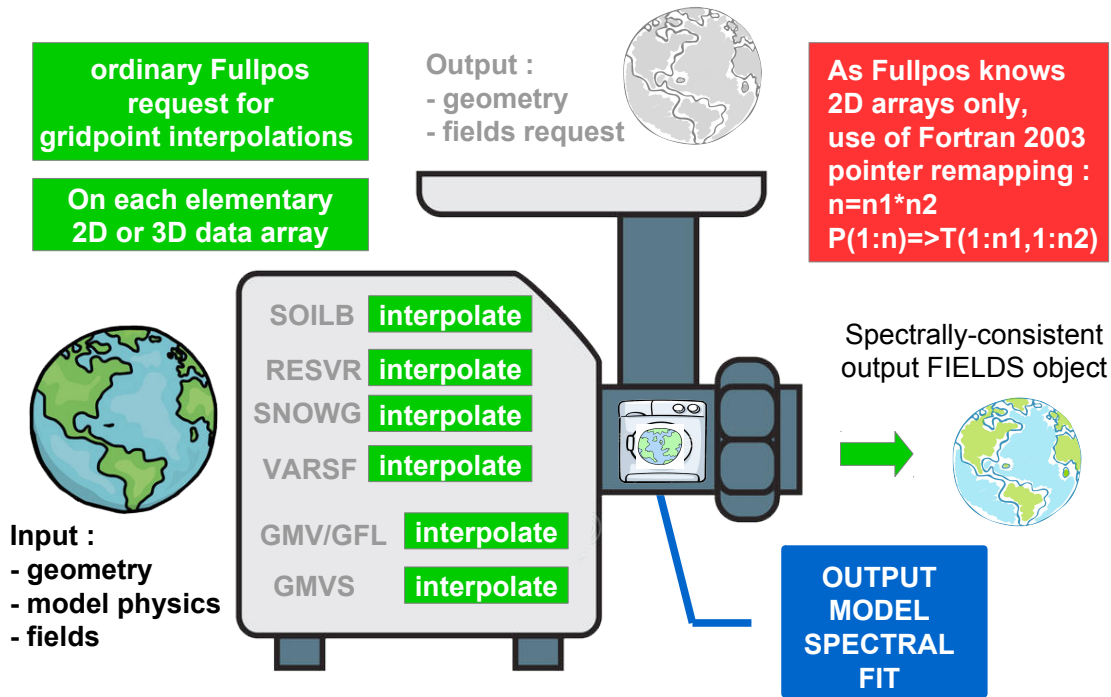


Figure 2 : How to change the fields object geometry without leaving the executable

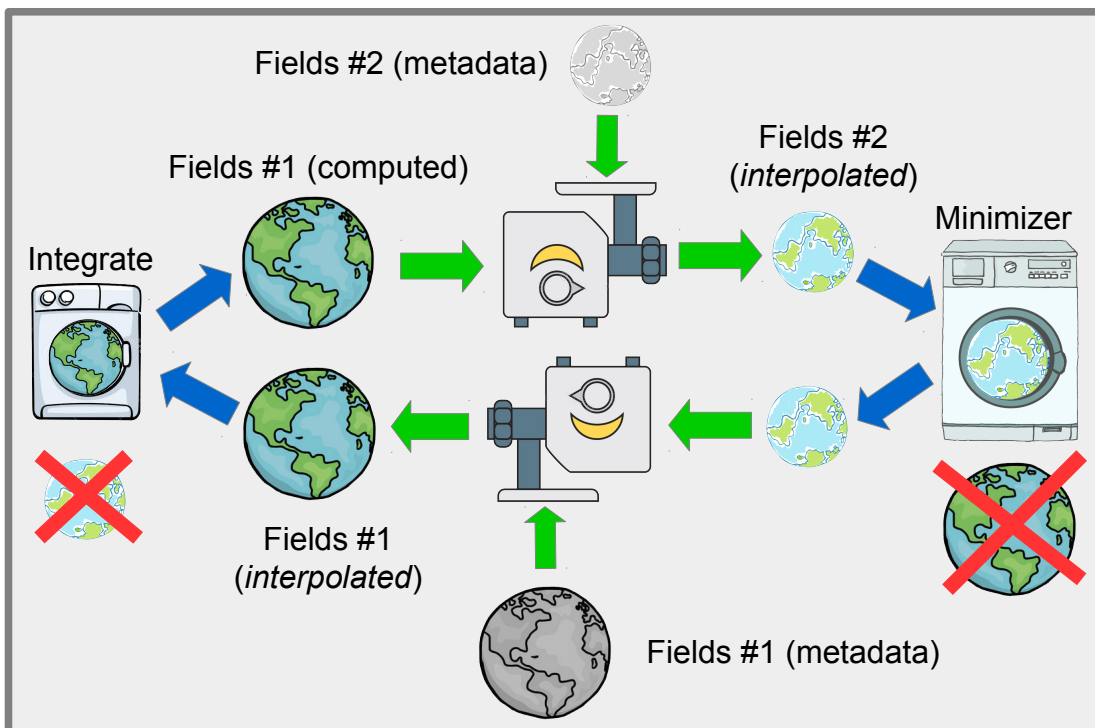


Figure 3 : Context of the 4D-Var assimilation for the change of geometry

5 Status in cycle 46, and beyond OOPS

In cycle 46 the refactoring of the post-processing *for itself* has been achieved, so that it can be called from the C++ OOPS layer. However the multi-instantiation of the post-processing is limited by the I/O-server which is not yet ready to support this facility (but the I/O-server is not expected to be used in OOPS). Multiple instantiation of the post-processing is possible, however simultaneous multi-instantiation in time would also needs the spectral transforms package to be refactored, but this is not on the critical path of developments.

A test program written in fortran has been used to control the change of resolution for OOPS. Testing should continue in order to assess the robustness if this new method. This program should be used also to evaluate its computational cost. Note that this method is unable yet to change the vertical levels, due to a miss of refactoring of the vertical definition. But again, this is not on the critical path of developments for OOPS.

Refactoring of the post-processing can go further, for optimization purposes and to simplify developments made by newcomers in the community.

There is room to take advantage of the multi-post-processors support, already in the fortran code of today, like low frequency against high frequency post-processing on different grids and for different fields ; or multi-couplers post-processing server (one input file transformed into a set of coupling files of different geometries). The use of multiple I/O-servers should be considered to achieve that.

As for the fields object transformator, its usage in another context than the global 4D-Var assimilation would be interesting, if possible. The tangeant linear of Fullpos could also be an idea of developement, in order to change directly the resolution of fields increments rather than plain fields in the 4D-Var assimilation.

CANARI model implementation using SYNOP for ALADIN Algeria

Idir Dehmous, Mohand Ouali Ait Meziane

1 Introduction

One of the relevant problems of numerical weather prediction is to find the best initial atmospheric state for forecast initialization. Data assimilation is a set of methods and techniques that allow to find a better estimation of this state. The process of data assimilation consists of a combination of meteorological observations, previous forecast (background) as well as the information provided by climatology. One of the methods used to analyze some parameter in surface level is CANARI (Code of Assimilation Necessary for ARPEGE for its Rejection and Initialization) which was introduced during the 1990s by Météo France for the limited air model ALADIN (Fischer et al., 2006), it is based on the principle of optimal interpolation algorithm. The typical equation of an optimal interpolation problem is given (Bouttier, 2007) by:

$$X_a = X_b + K(Y - H[X_b]) \quad (1)$$

where

$$K = BH^T(HBH^T + R)^{-1} \quad (2)$$

X_b is first guess state (resulting from a previous forecast), X_a is an atmospheric analysis state, H observation operator which simulates the values of observations in model grid point, B is matrix of model error covariances, R is the observations error covariance matrix.

2 Format and type of observations

Météo France uses the OULAN binary to generate the OBSOUL file in order to convert the alphanumeric raw data into a readable format for the BATOR program, other versions of OULAN program have been developed in order to process observations coming from the different stations of the other countries of ALADIN consortium, example (Hungary, Tcheque Republic, ..) (Randriamampianina and al, 2008). At the algerian meteorological office, the OULAN program is not available, therefore to generate the input files for the BATOR program the synops are encoded directly in BUFR format using the program "synop2bufr.f90". In our experiment about 35 stations are used for each analysis, Figure 1 shows their geographical locations.

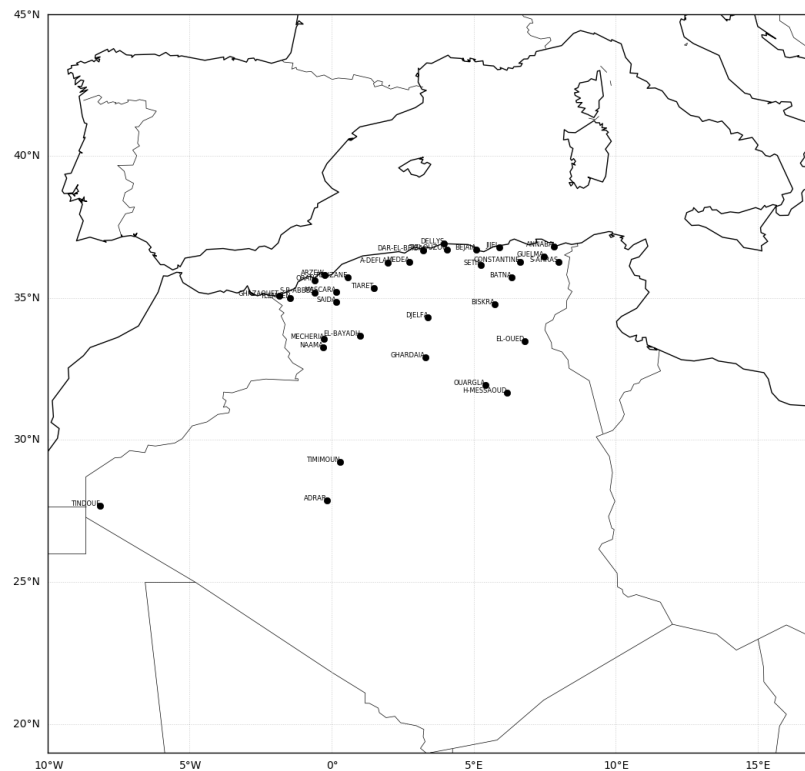


Figure 1: Stations geographical locations

3 Preprocessing of observations and preparation of the ODB

During our CANARI assimilation experiments for the ALADIN Algeria domain, we started by preparing observations in ODB (Observation Data Base) format, this format was developed by the ECMWF (European Center for Medium Range Weather Forecasts) and is designed to handle the considerable data flow of observations (Saarinen, 2004). There are two types of ODB formats: the ECMA compressed format used exclusively for the CANARI model and the screening, and CCMA format commonly used for variational configurations (3DVAR and 4DVAR). In our setup of the CANARI model, the ODB was generated in ECMA format. The program that generates the ODB is the BATOR binary of the ARPGE / ALADIN code. It aims to extract the observations from the data file in OBSOUL, GRIB and BUFR format and write them in the ODB database. In the case where several types of observations are used (AMDAR, ASCAT etc), an ECMA sub-base (ECMA.amdar, ECMA.ascat etc) for each type of observation is generated. Once the ECMA databases are written, they are then merged using the odbtools (SHUFFLE) binary, the final output database contains all the required files and is used as input for CANARI.

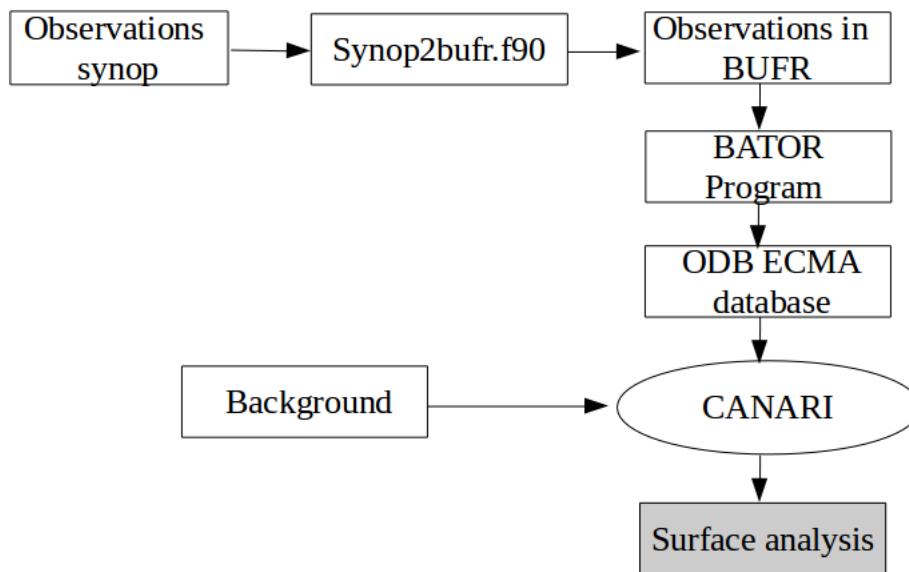


Figure 2: Canari surface analysis process

4 Experiment's description

CANARI data assimilation experiments for the ALADIN Algeria model have been realized in the period between 13-04-2017 and 30-04-2017, taking each run the 06h00 synoptic file including the stations shown in figure 1, the observation files contain the standard parameters, such as the temperature at 2 meters, the relative humidity, the pressure at sea level, the wind speed and wind direction. The first-guess file used is the 6:00 ALADIN forecast of the 00h network "ICMSHALAD + 0600". In addition to the observations data and the background file, the two climatological files of the current month and the previous month are used as input for CANARI, necessary to update the climatological constants (vegetation, albedo, etc.)(Taillefer, 2002). Moreover, during the CANARI configuration, only the analysis of the two temperature variables and the relative humidity at 2 meters is activated (LAET2M key and LAEH2M equal to "True" in the NACTEX namelist). At the end of execution only the two parameters "CLSTEMPERATURE" and "CLSTHUMID.SPECIF" are extracted from the analysis file.

5 Impact of a single observation

Figures 3 and 4 show the impact of a single observation on 2m temperature and humidity. These results are obtained for the station of Dar El-Beida for the date of 13-04-2017 at 06h.

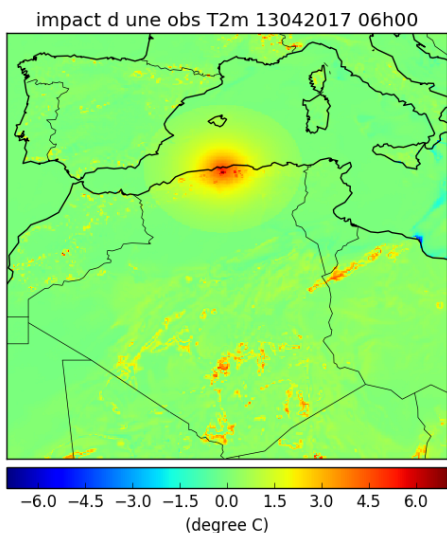


Figure 3: Impact of single observation on T2m increment

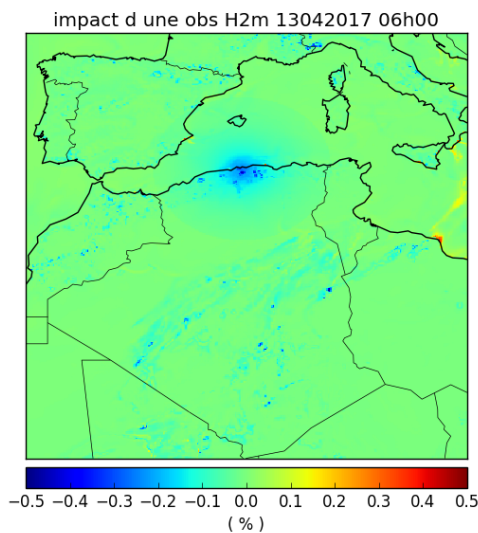


Figure 4: Impact of single observation on H2m increment

The plots (difference analysis-background) show a considerable increments for the both parameters T2m and H2m. The information provided by the observations source tends to spread under the effect of optimal interpolation following circular contours, then attenuates completely as one moves away from the obseravtion point (about 100km from the station), with increments comprises between -6 °C and 6 °C for temperature. For the 2m humidity parameter, differences between -0.5% and 0.5% are observed.

6 Impact of all observations

The figures below show the difference between the first-guess temperature field, resulting from the forecast 06h and the analysis obtained after the introduction of the observations. In order to clearly see the effect of the analysis on the used background, the namelist is configured in order to performe the analysis only on temperature and humidity at 2 meters.

In fact, the sea surface temperature (SST) used in our analysis is that of the ARPEGE model interpolated on the ALADIN 8km grid, the alterations that we see on the analyzed temperature and humidity fields (figure 6 and 8) are mainly caused by information provided from the observations, particularly for the north, northwest and southwest regions. These are relatively the high density areas stations.

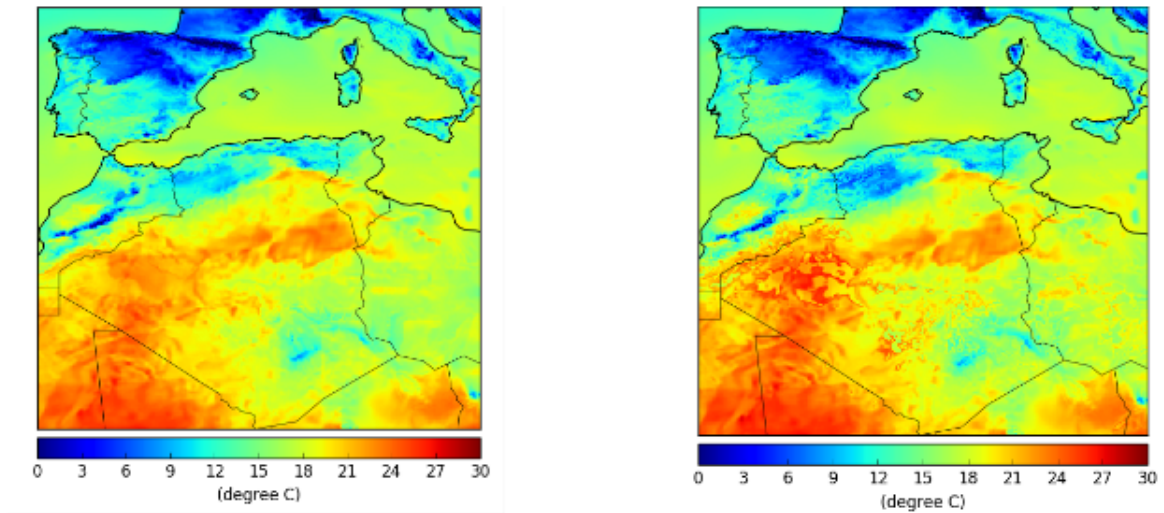


Figure 5: background T2m (left) , analysis (right)

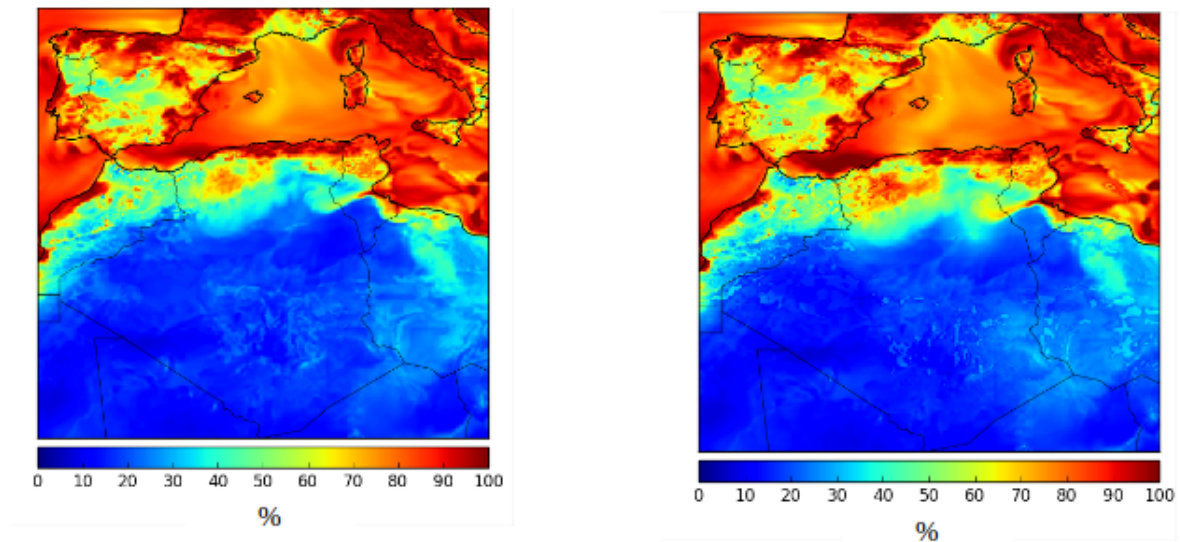


Figure 6: background H2m (left) , analysis (right)

Because of the small number of stations used for our experiment (35 stations), the difference observed between analysed and background fields is not very significant. To highlight the contribution of information provided by the observations to the analysis, the evolution of the parameters T2m and H2m and their biases were plotted over the different analysis dates.

Concerning the evolution of the temperature at 2 meters, the plots show significantly better biases (figure 8) compared to the operational forecasts, i.e an average bias of 2.45 °C for the background fields versus 1.70 °C for the analyzed fields .Note that the CANARI analysis tends to take values between those given by observations and those given by the background (Figure 7), except for days from 26-04-2017 to 28-01-2017 where there is a slight deterioration in the scores for the analysis.

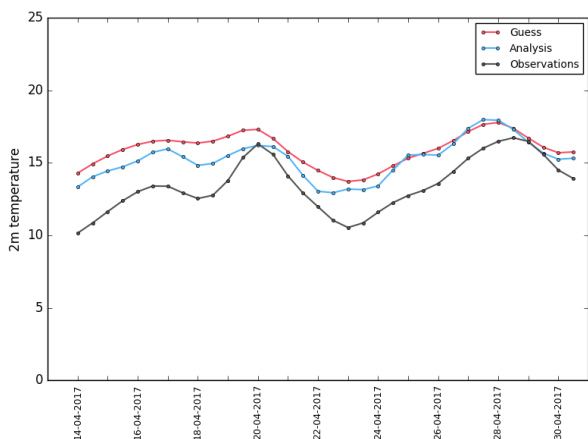


Figure 7: Evolution of T2m background and analysis

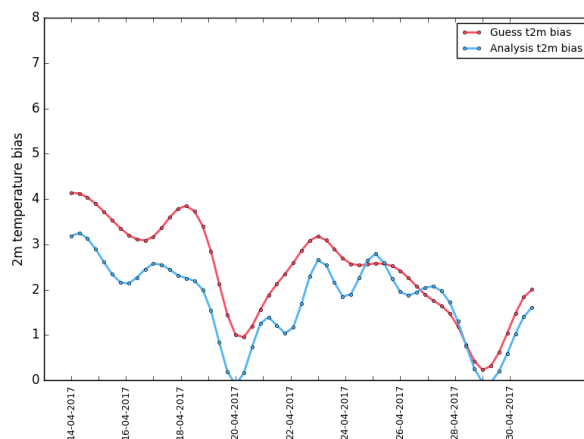


Figure 8: Evolution of T2m background and analysis biases

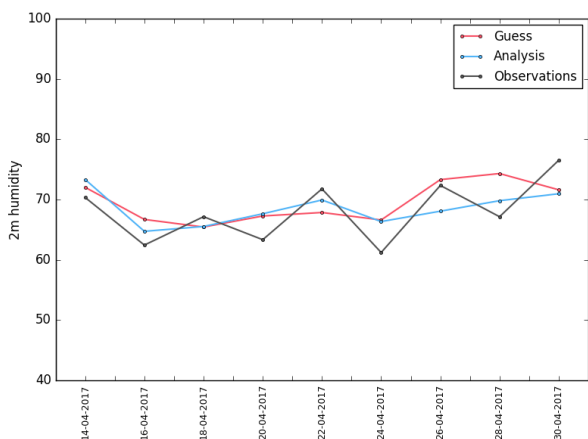


Figure 9: Evolution of H2m background and analysis

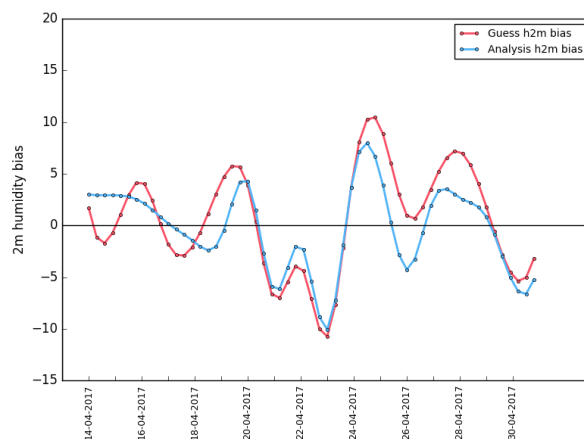


Figure 10: Evolution of H2m background and analysis biases

The evolution of analyzed surface moisture (Figure 9) shows oscillations around the observations and ALADIN background. On the other hand, Figure 10 shows a decrease in the average bias between analysis and first-guess with 0,65% for the background and 0,40% for the analyzed humidities (figure 10).

Conclusion

The CANARI model has been successfully implemented on HPC with archiving of analysis files and ODB databases generated from the synoptic observations. The introduction of the observations shows an impact on the 2 meter temperature parameter with an appreciable decrease of the biases compared to non-analyzed ALADIN forecasts (average bias of 2.45 °C for the background versus 1.70 °C for the analysis). The 2 meter analyzed humidities show oscillations around the observed data and the ALADIN background, but there is a decrease in mean biases between the analysis and the background values (0.65 % for first-guess and 0.40 % for the analyzed humidities). Finally, tests over a longer period will be planned with an assimilation cycle (every 06h) using main synop and other types of observations data, in order to validate the CANARI configuration for operational purpose.

7 References

Bouttier F. Arome, avenir de la prévision régionale, 2007.

Fischer C., Montmerle T., Auger L., and Lacroix B. Météorologie, 54 edition, 2006.

Randriamampianina R., Storto A., Aladin-Harmonie/Norway and its assimilation system, the implementation phase, HIRLAM Newsletter, 54, 20–30 ,2008.

Saarinen S. , ODB User Guide, ECMWF draft , 1st edition, 2004.

Taillefer F., Technical documentation ,based on ARPEGE cy25T1, 2002.

Running AROME DUST 3km : Validation over new domain

Abdenour AMBAR, Mohamed MOKHTARI, Abdel Aziz KONSEIBO

1 Introduction

This paper is a short article presenting validation of AROME-Dust (3km) over new domain (Burkina Faso). It shows the ability of this convective scale model to predict the life cycle of desert aerosols (emission, transport and deposition) and then confirm the first validation done previously over Algeria (A.Ambar and M.Mokhtari, 2016).

2 Set up

The AROME-Dust configuration is available locally based on cy40t1 at a resolution of 3 km, for research purpose and not for operational use, due to high calculation demands. It is also available on Beaufix (Meteo France machine) based on cy43t2 (M.Mokhtari and A.Ambar, 2016) and recently updated (M.Mokhtari, 2018) in order to take into account the thermic transport process and fix few bugs.

The full experience was prepared on Beaufix based on cy43t2_bf.04. Our model is running at 3km resolution and coupled to Arpege, with recent version of Surfex (V8.0) for surface physics. Climatological files were prepared over Burkina Faso domain (Fig -1-).

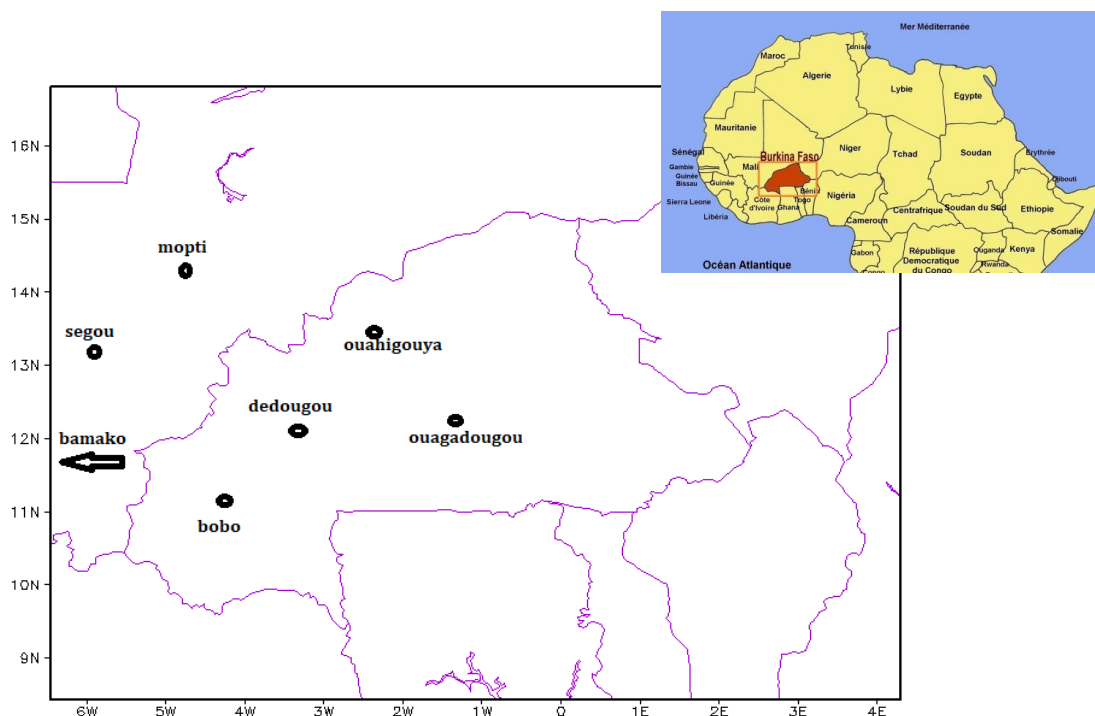


Fig -1- : Burkina Faso domain.

3 Example : results and validation

Figure -2- represents MSG-SEVIRI satellite images on April 14th, 2016 at 09^h, 12^h, 15^h and 18^h, over Burkina Faso domain and some parts of the bordering countries. It shows an important dust uprising event caused by east to northeast strong winds.

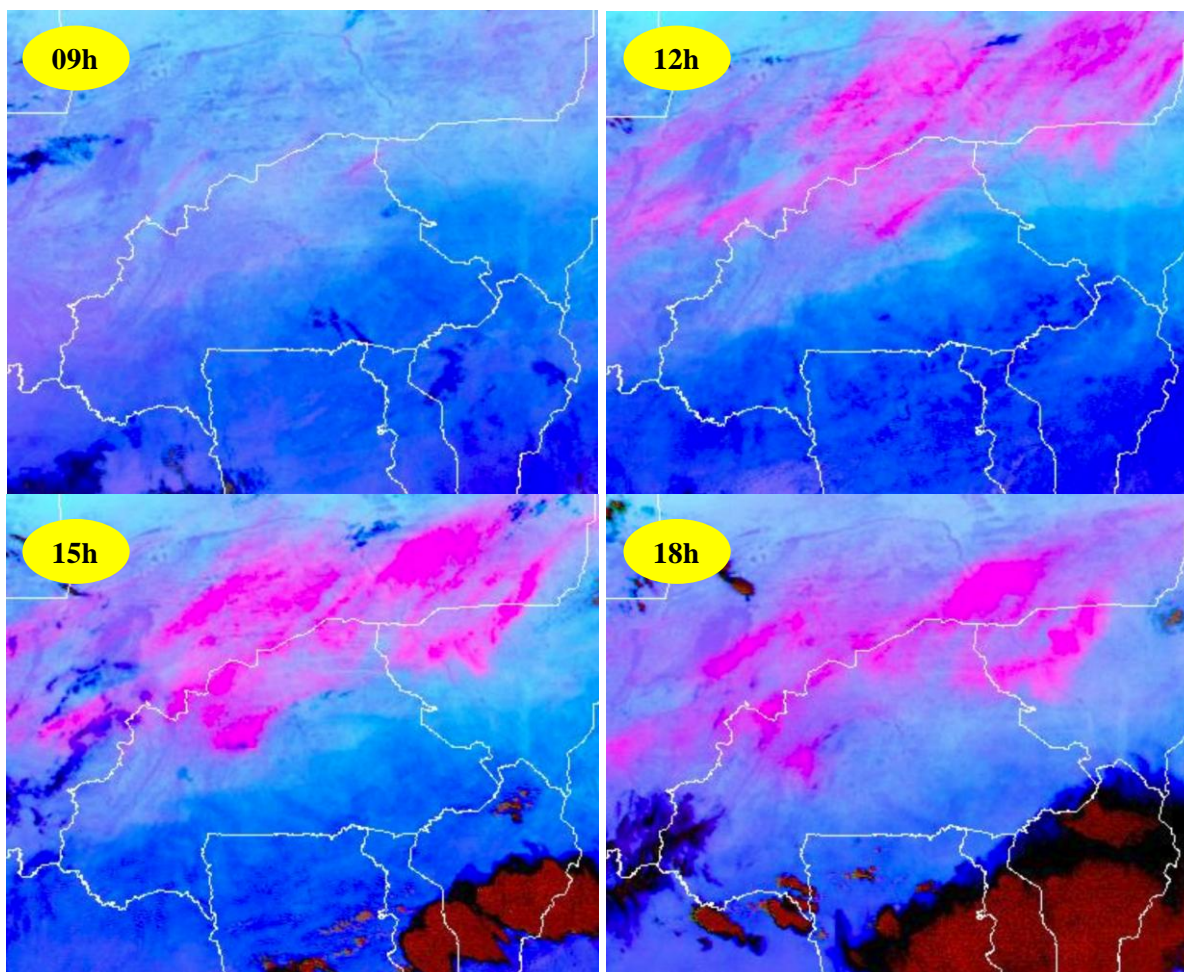


Fig -2- : MSG-SEVIRI satellite images over Burkina Faso domain on April 14th, 2016.

This situation was pretty well predicted by AROME-Dust (Figure -3-) and prove again how this convective scale model can give a nearly realistic desert dust forecasts.

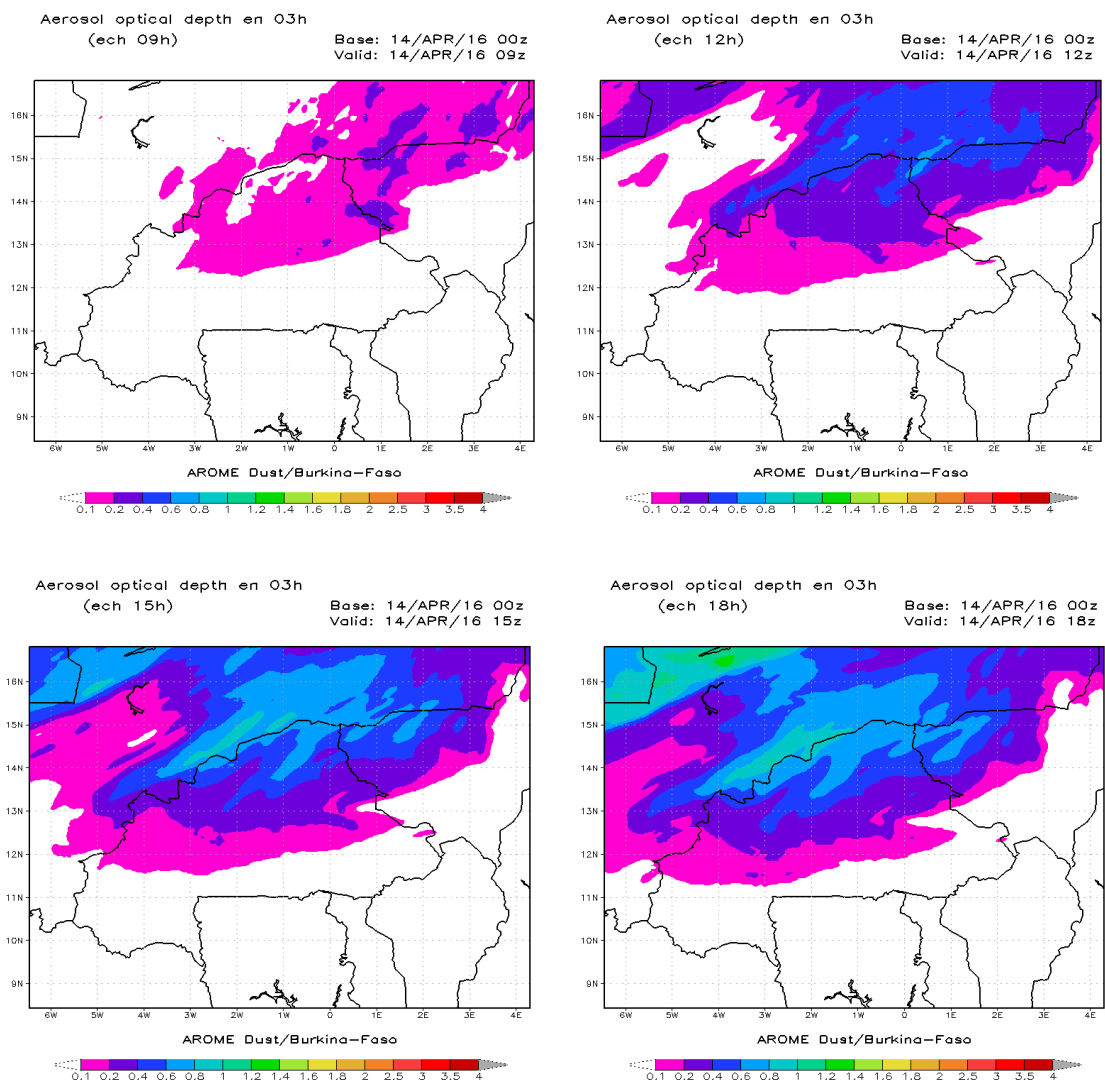


Fig -3- : Aerosols optical depths (AOD) simulated by AROME_Dust on April 14th, 2016 over Burkina Faso domain.

Conversion of desert dust concentration values to visibility allows us to compare our results to visibilities observed in few stations situated in our domain. Fig -4- shows that visibilities simulated by AROME_Dust follow generally the same trend as observations.

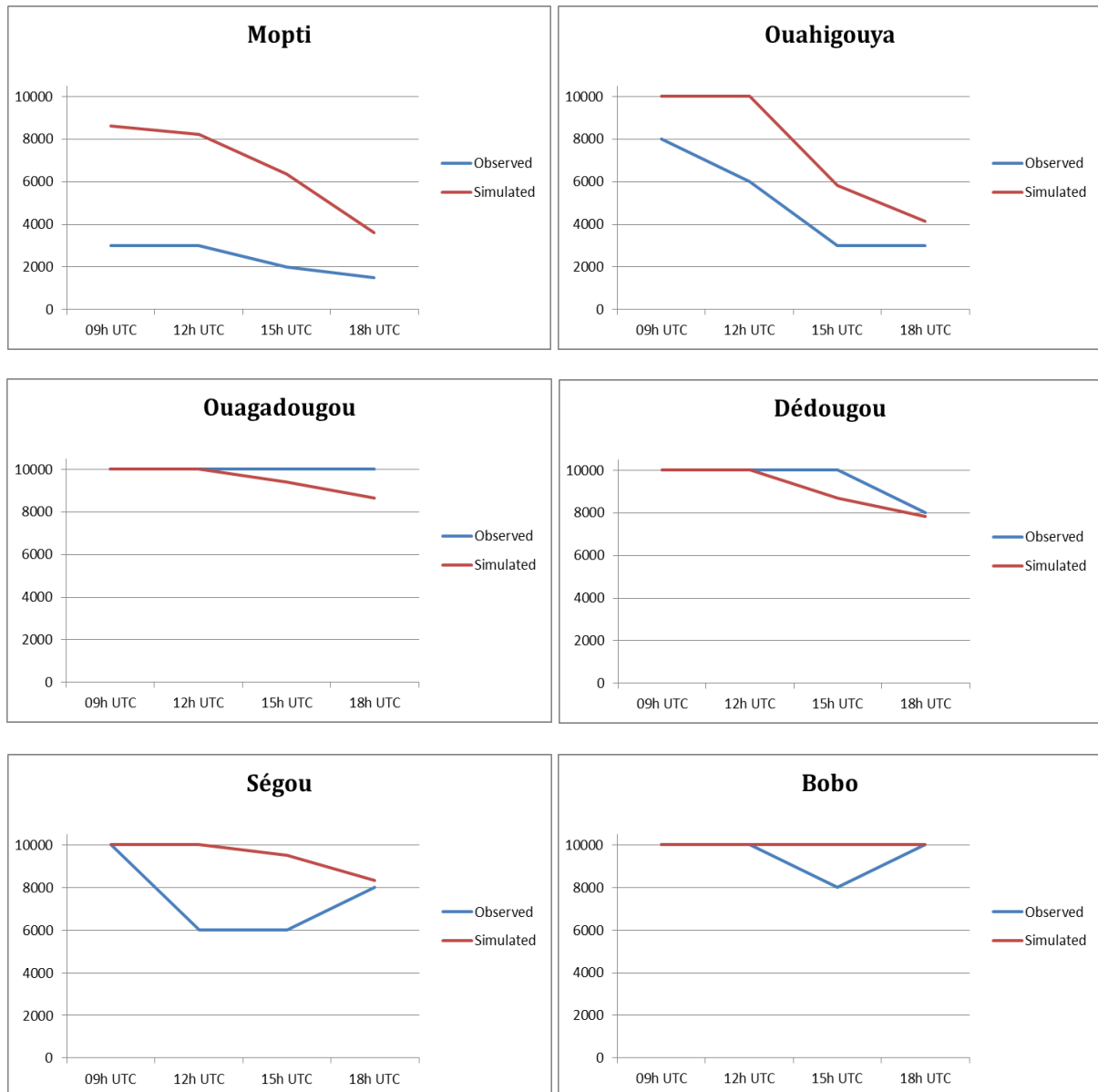


Fig -4- : Visibility measured (METAR observations) and simulated (AROME_DUST) at several stations (Burkina Faso and Mali) on April 14th, 2016.

4 References

A.Ambar and M.Mokhtari (2016): Desert dusts modeling in AROME: Contribution of physical parameterizations at convective scale. ALADIN-HIRLAM Newsletter N°08.

M.Mokhtari and A.Ambar (2016): Updating and validation of Arome_dust. Stay report, CNRM.

M.Mokhtari (2018): Préparation d'un pack de référence de la version AROME_Dust. Stay report, CNRM.

Verification of HARM-AROME model at 1.0 km over Spanish Harbour Areas

Inés Santos, Elena Padorno, José A. Ruíz, Isabel Martínez

1 Introduction

A very high resolution numerical weather prediction is a request not just from forecasters but from the huge amount of external users of numerical weather prediction data as well. SAMOA Project, funded by the Spanish National Harbour Authority, aims to develop a meteorologic and oceanographic support system for the National Harbours. One of the modules of this project is focused on a very high resolution weather forecast for surface variables over harbour influence areas. Paying special attention to the 10 meter wind forecast, due to its importance both for harbour operations and for its integration on local wave models.

In this frame, AEMET is running HARMONIE-AROME over 4 domains of 1 km resolution and 30 seconds time step twice per day with a forecast length of 48 hours. The obtained results show the added value of the 1 km resolution compared to the 2.5 km of the operational run. It is noticeable the higher data density and richer dynamics, capturing smaller eddies and more local behaviours, and also the better verification scores. Nevertheless, this is just a first step, much further work has to be done; the introduction of a proper data assimilation, improvements in the physics and numerical methods or the use of a more appropriate verification method.

2 SAMOA Project

At the initial phase of SAMOA Project, 7 Harbour Authorities, encompassing 16 harbours along the Spanish coast, showed interest in the high resolution weather forecast over their influence areas. Due to the high computational cost of running HARMONIE-AROME at 1 km resolution over the whole Spanish territory, the coastal character of the areas and the limited resources available; 4 disjointed domains were defined. One covering the Canary Islands, one along the Gulf of Biscay, another over the Alboran Sea and the last one over the Mediterranean Sea, including the Balearic Islands and Mediterranean peninsular coast.

A new configuration of HARMONIE-AROME v40h1.1 was compiled to include the proper parameters for the new domains and to fulfil stability. The 4 areas of interest currently run twice per day on the ECMWF supercomputer, at 00 UTC and 12 UTC, with a forecast length of 48 hours. But the execution is being moved to AEMET premises for a better control and supervision. The output GRIB files containing weather surface variables (surface pressure, surface and 2 m temperature, 10 m wind, relative and specific 2 m humidity, total precipitation and cloud cover and radiation and heat fluxes) are converted into NetCDF format for seven smaller subareas centred on the harbour regions and delivered to the National Harbour Authority for its integration in their operational systems.

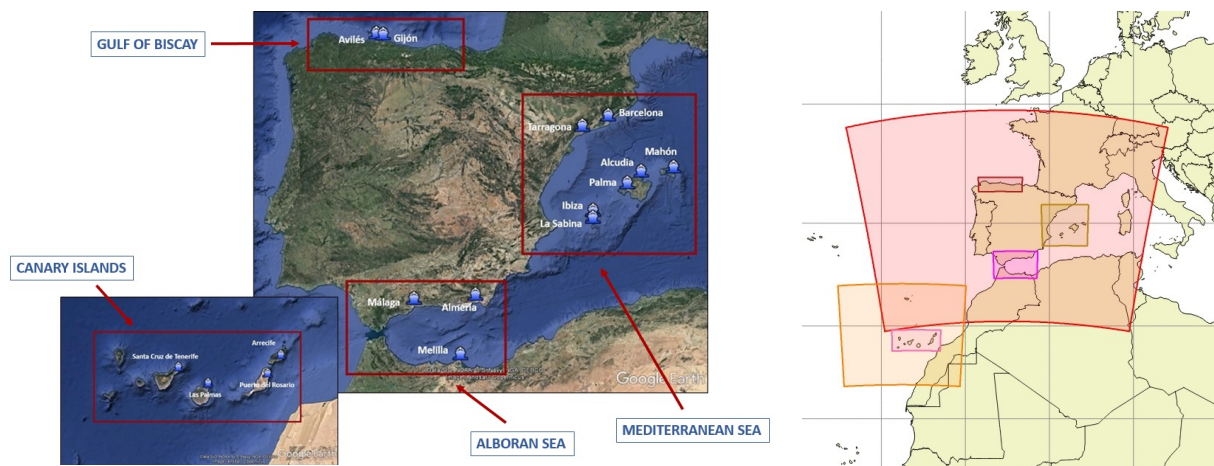


Figure 1: On the left, geographical view of the 4 domains with the included harbours. On the right, the 1 km new domains and the 2.5 km AEMET operational domains.

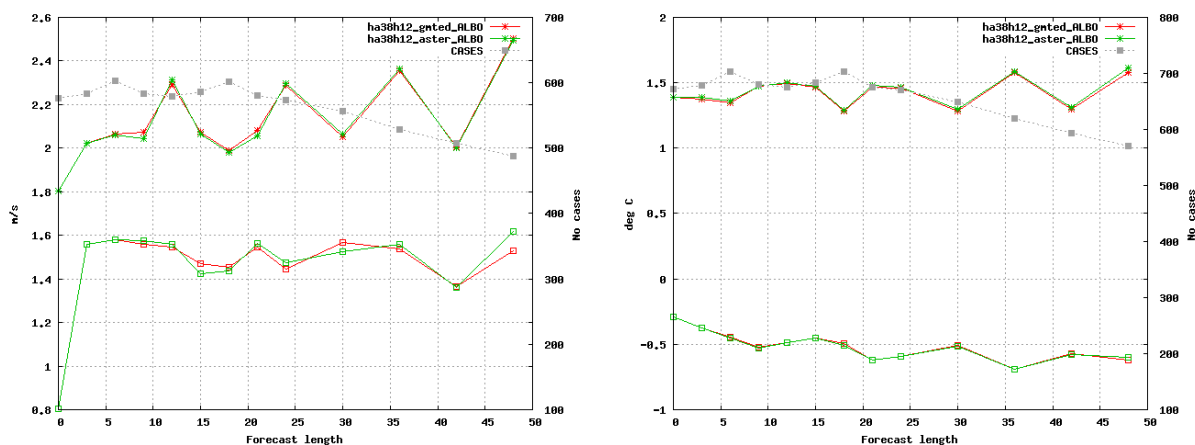
3 Model Configuration

The model configuration started with HARMONIE-AROME v38h1.2, it soon migrated to v40h1.1.beta.5 and finally to v40h1.1.

Topography

Before the GMTED2010 topography was incorporated to the 40h1.1.beta.5 model version, integrations were done using the ASTER topographical database, developed by NASA and METI and with 1" (about 30 m) resolution.

Comparing the verification results obtained for the GMTED2010 and ASTER topographies at cases of study of intense wind for three of the areas (figure 2) with version ha38h1.2 using IFS nesting, dynamical adaptation and PC scheme; the scores are quite similar for two of them but significantly different for one, the Mediterranean Sea, where the ASTER topography provides much better figures.



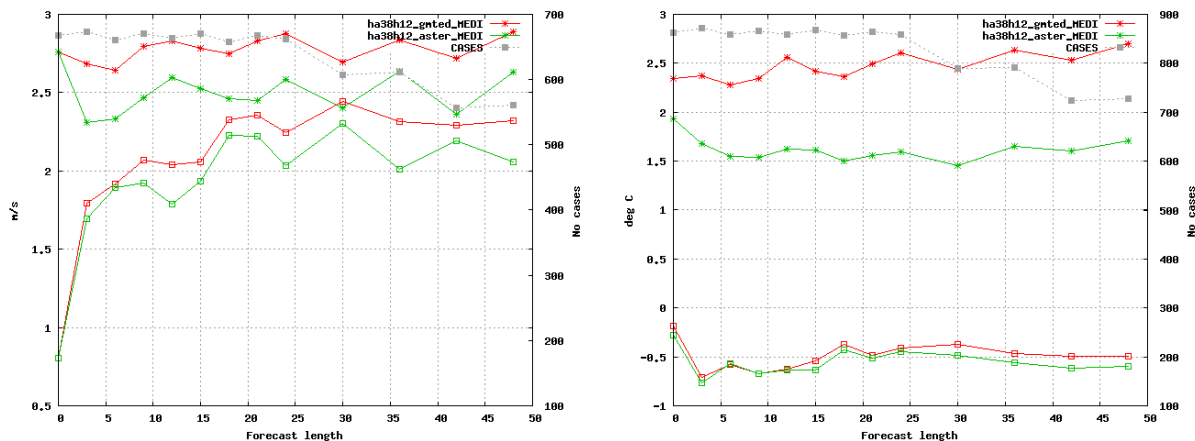


Figure 2: Verification scores for U10m on the left and T2m on the right using GMTED2010 (red) and ASTER (green). Graphics on the first line correspond to the Alboran Sea domain during 01-07/12/2016. Graphics on the second line correspond to the Mediterranean Sea domain during 12-18/01/2017. RMSE STDV (*) and bias (□).

Nesting

A nesting to AEMET operational HARM-AROME 2.5 km operational model was considered but the similar scores, or even better, for the IFS nesting (figure 3) together with the possibility of an earlier data delivery to the customer, drew to the selection of the second option.

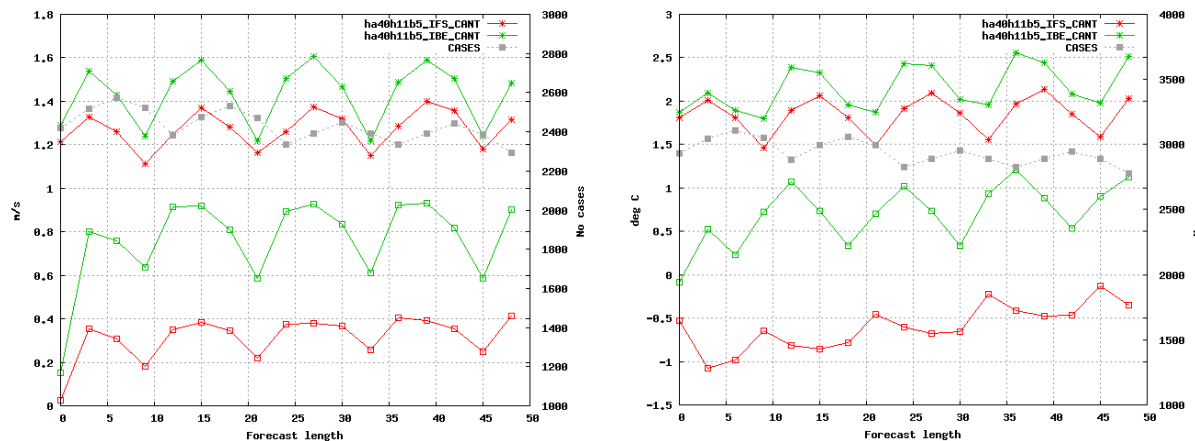


Figure 3: Verification scores for U10m on the left and T2m on the right using IFS (red) and HARM-AROME 2.5 km (green) nesting. Gulf of Biscay domain during July 2016. RMSE STDV (*) and bias (□).

Analysis

Atmospheric analysis was discarded at this stage of the project. On the other hand, blending and surface analysis did not show much benefit (figure 4). So, both, atmosphere and surface are initialized from the IFS model at each new run.

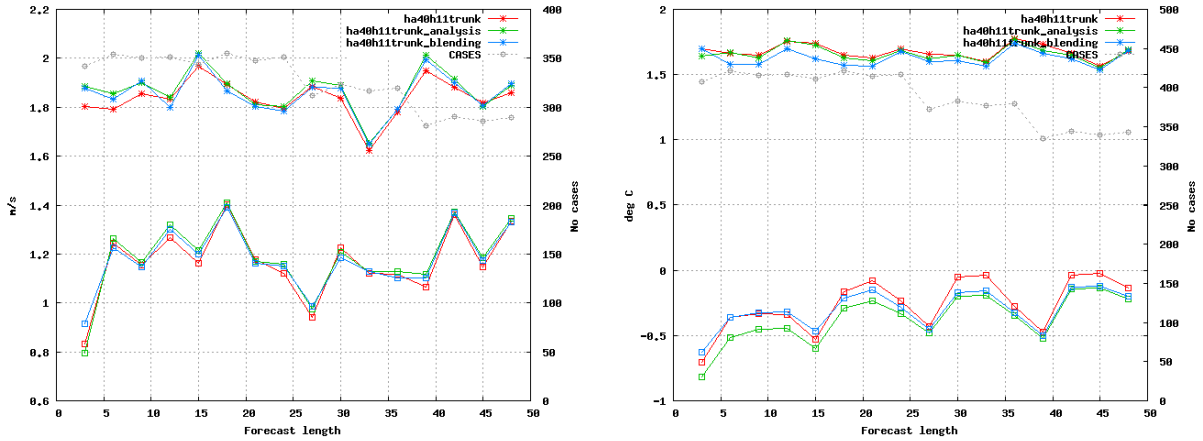


Figure 4: Verification scores for U10m on the left and T2m on the right using dynamical adaptation (red), CANARI_OI (green) and CANARI_OI and blending (blue). Gulf of Biscay domain during 10-15/01/2017. RMSE STDV (*) and bias (□).

PC vs SETTLS

A change of numerical strategy, from SETTLS to predictor-corrector, was performed in order to obtain model stability. It proved to stabilize the model despite the weather situation, unlike different tested strategies. Since this modification, the 1 km resolution configuration has been running twice per day without failure from May 2016 (figure 5). Other namelist variable changes were also included: LPC_FULL = TRUE, LPC_NESC = TRUE, LPC_NESCT = FALSE, LPC_CHEAP = TRUE, NSITER = 1, LRHDI_LASTITERPC = TRUE, LSETTLS = FALSE, LGWADV = TRUE and LRDBBC = FALSE.

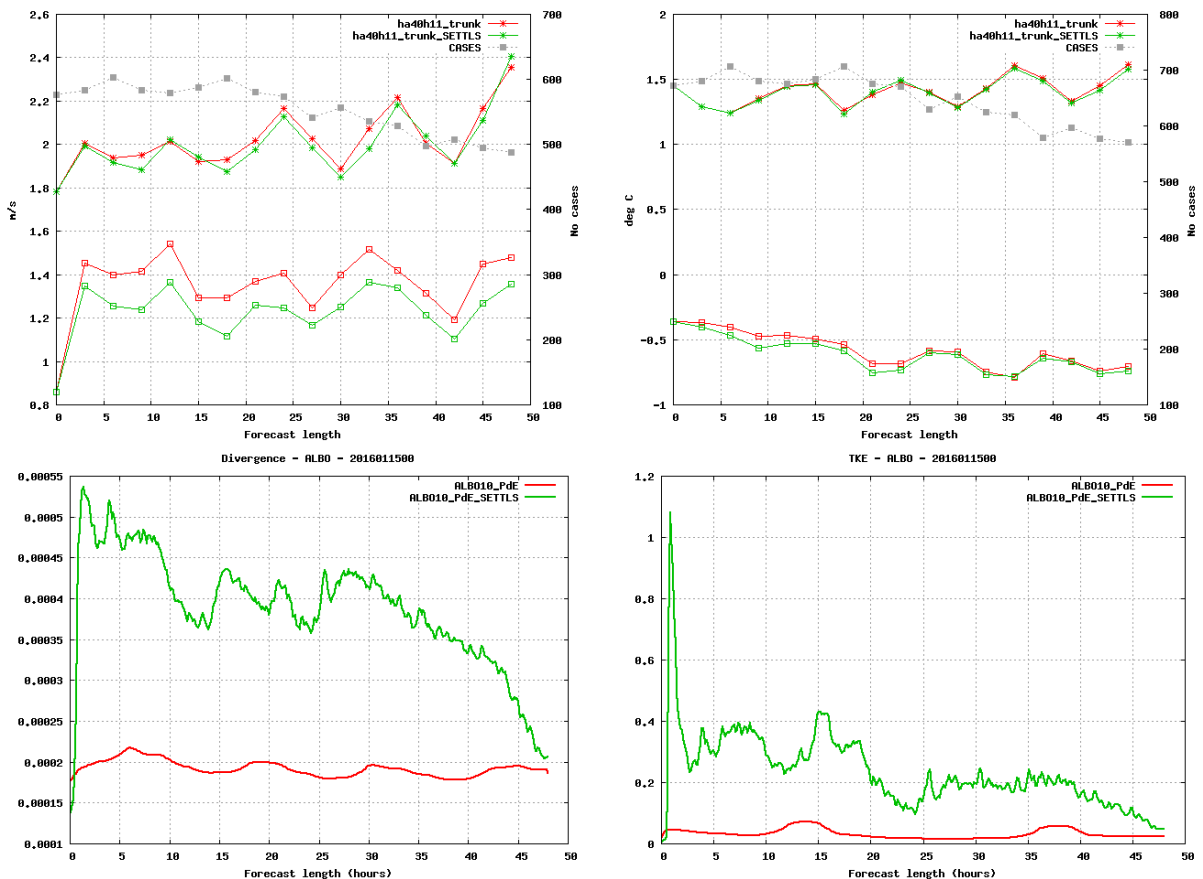


Figure 5: Up, verification scores for U10m on the left and T2m on the right using P-C (red) and SETTLS (green) for the Alboran Sea domain during 01-07/12/2016. RMSE STDV (*) and bias (□). Down, divergence, on the left, and TKE, on the right, norms at a critical situation for the model stability over the Alboran Sea on the 15th of January 2016.

Diffusion and HARATU

In order to improve the forecasting results, especially at some areas like the Alboran Sea, which showed verification scores very similar to the 2.5 km model, different strategies were tested in an attempt to better represent the orography impact on turbulence.

Reversing the HARATU update at HARMONIE version 40h1.1 was an option due to its simplicity and it proved to slightly improve the verification scores at all areas for wind with a very little worsening for temperature. The different impact of this modification over each area is uneven; showing close to no change at the Alboran Sea and a substantial one t the Gulf of Biscay. On the other hand, the activation of the Semi-lagrangian Horizontal Diffusion (SLHD) for the spectral variables improved the results at all the areas, being crucial for the scores improvement at the Alboran Sea. The final configuration activates Semi-lagrangian Horizontal Diffusion for all the spectral variables but humidity and temperature.

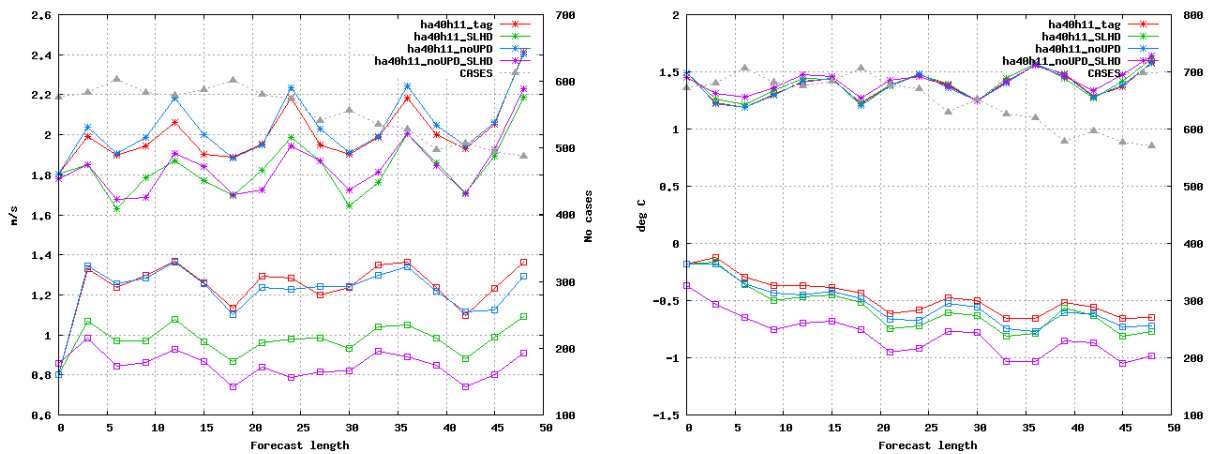


Figure 6: Alboran Sea domain during 01-07/12/2016. Verification scores for U10m on the left and T2m on the right, with the reference 40h11 model version (red), activating the SLHD (green), reversing the HARATU update (blue) and with the combination of both options (purple). RMSE STDV (*) and bias (□).

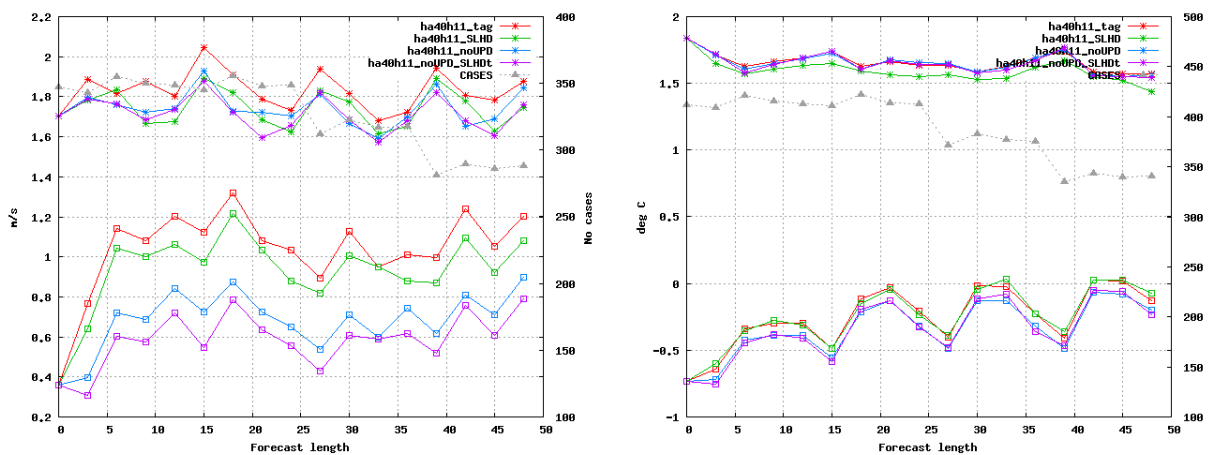


Figure 7: Gulf of Biscay domain during 10-15/01/2017. Verification scores for U10m on the left and T2m on the right, with the reference 40h11 model version (red), activating the SLHD (green), reversing the HARATU update (blue) and with the combination of both options (purple). RMSE STDV (*) and bias (□).

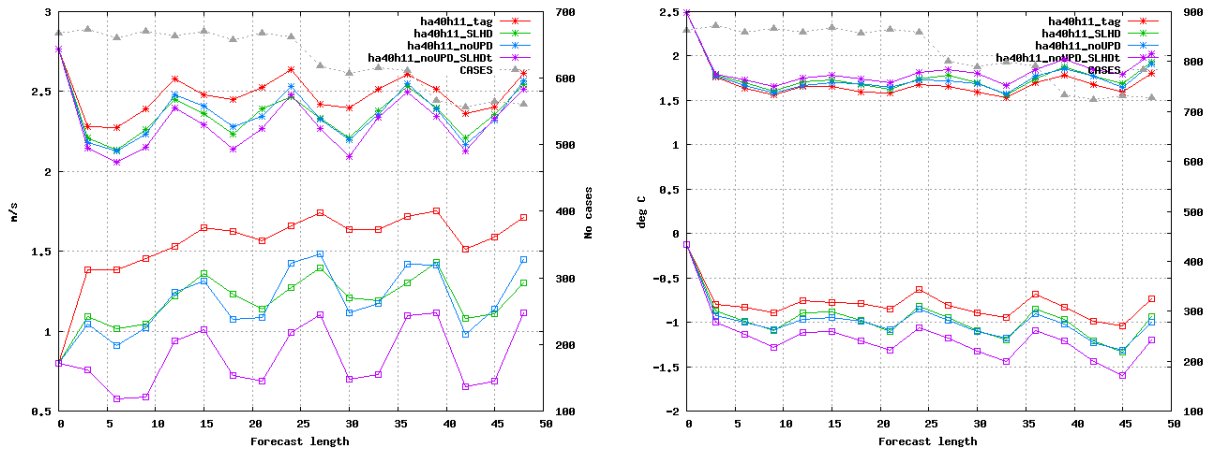


Figure 8: Mediterranean Sea domain during 12-18/01/2017. Verification scores for U10m on the left and T2m on the right, with the reference 40h11 model version (red), activating the SLHD (green), reversing the HARATU update (blue) and with the combination of both options (purple). RMSE STDV (*) and bias (□).

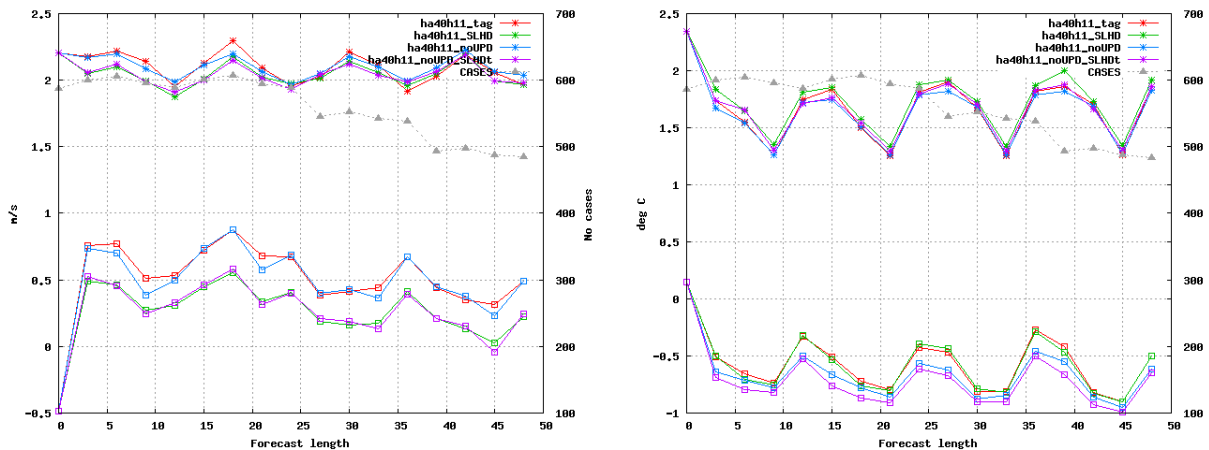


Figure 9: Canary Islands domain during 16-21/03/2017. Verification scores for U10m on the left and T2m on the right, with the reference 40h11 model version (red), activating the SLHD (green), reversing the HARATU update (blue) and with the combination of both options (purple). RMSE STDV (*) and bias (□).

4 Verification Results

A verification of the final configuration has been performed during complete months, March and October 2017, in order to assess the impact of the final 1 km HARMONIE-AROME suit with respect to the operational 2.5 km one.

In general, the new configuration overestimates winds but much less than the 2.5 km run, showing a significant score improvement for this variable at all areas. The general behaviour is quite similar for the other variables, except for temperature, with a slightly higher underestimation at some cases. The 12 hours precipitation ETS obtains better verification figures for the 2.5 km run as well.

The following figures (10 to 13) compare the operational 2.5 km run with the new 1.0 km configuration run, with IFS nesting, dynamical adaptation and PC scheme and both executed with cycle 40h1.1 during March 2017.

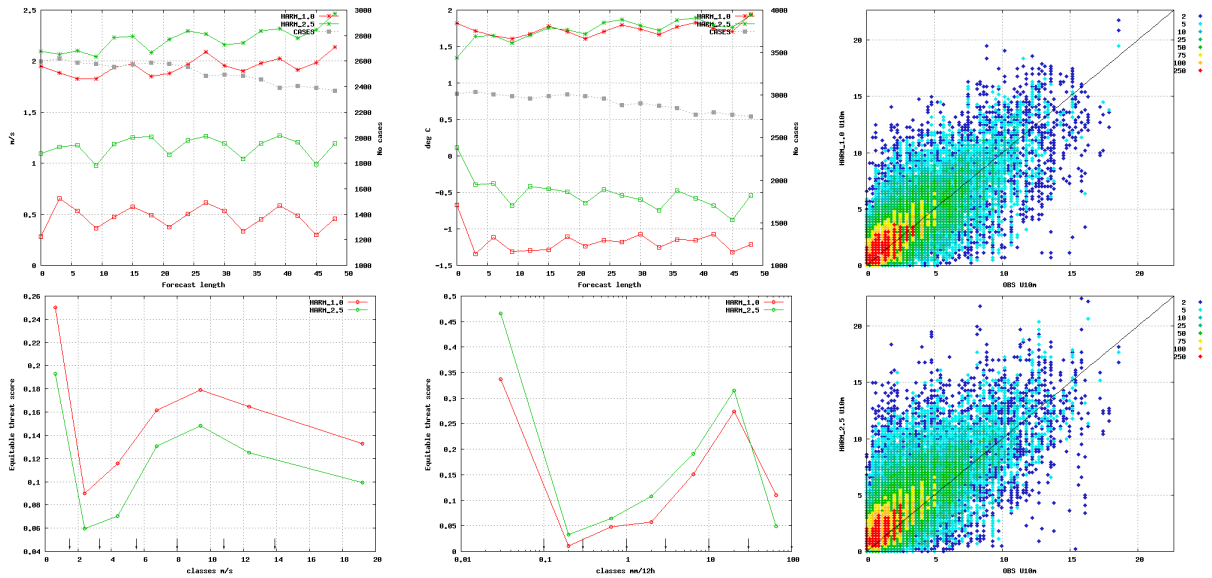


Figure 10: Alboran Sea domain. Verification scores for HARM-AROME 1.0 (red) and HARM-AROME 2.5 (green). U10m (up left) and T2m (up centre). RMSE STDV (*) and bias (□). ETS U10m (down left) and ETS PE (down centre). On the right, the U10m scatterplots for 1.0 km (up) and for 2.5 km (down).

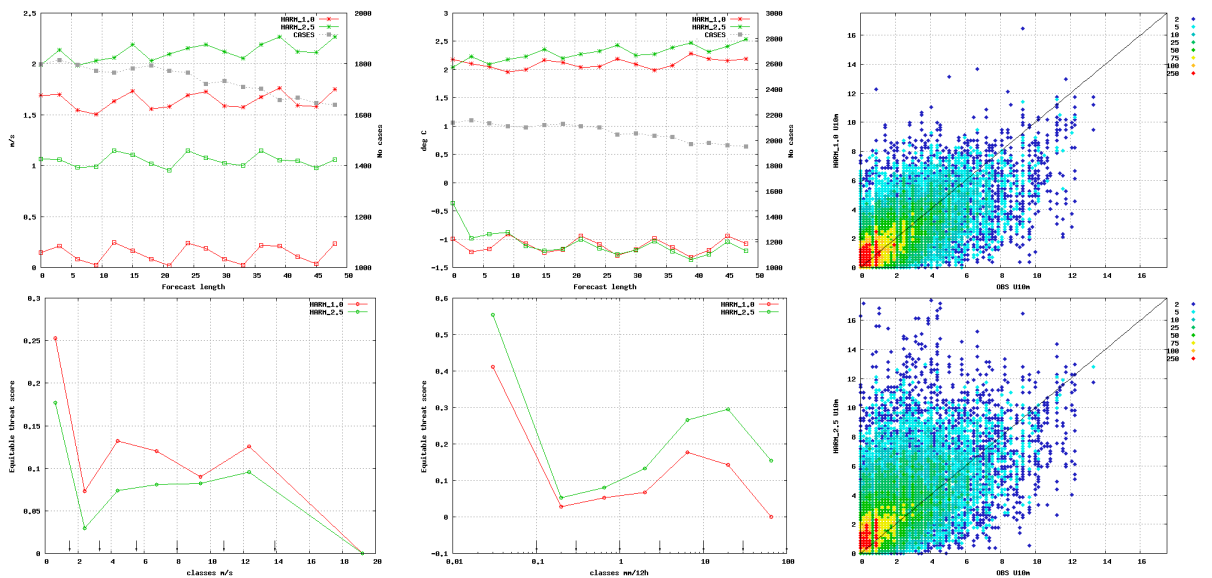


Figure 11: Gulf of Biscay domain. Verification scores for HARM-AROME 1.0 (red) and HARM-AROME 2.5 (green). U10m (up left) and T2m (up centre). RMSE STDV (*) and bias (□). ETS U10m (down left) and ETS PE (down centre). On the right, the U10m scatterplots for 1.0 km (up) and for 2.5 km (down).

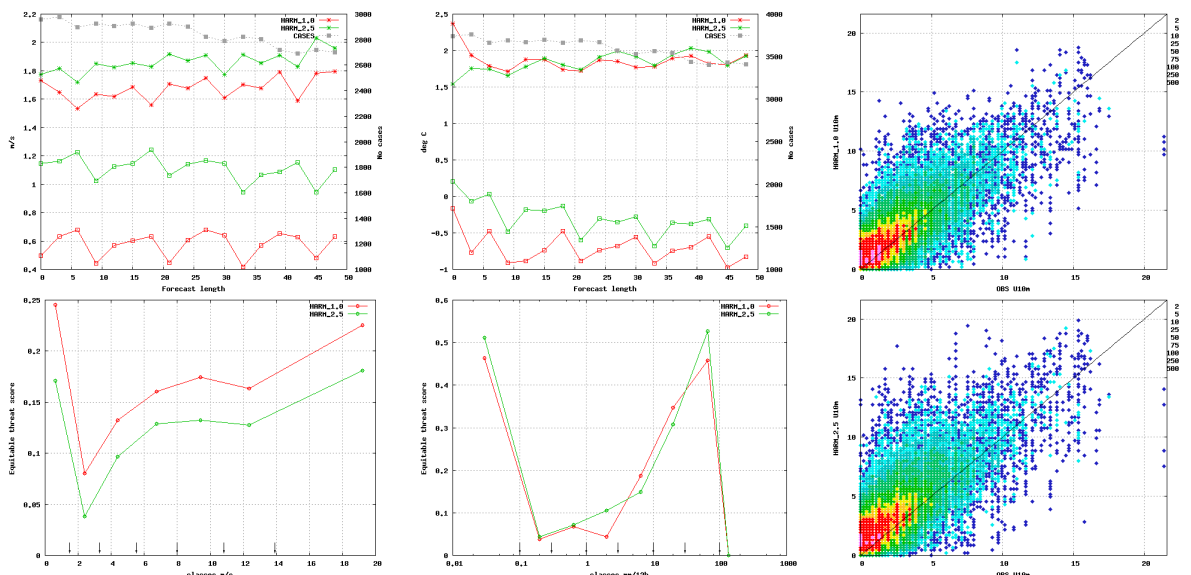


Figure 12: Mediterranean Sea domain. Verification scores for HARM-AROME 1.0 (red) and HARM-AROME 2.5 (green). U10m (up left) and T2m (up centre). RMSE STDV (*) and bias (□). ETS U10m (down left) and ETS PE (down centre). On the right, the U10m scatterplots for 1.0 km (up) and for 2.5 km (down).

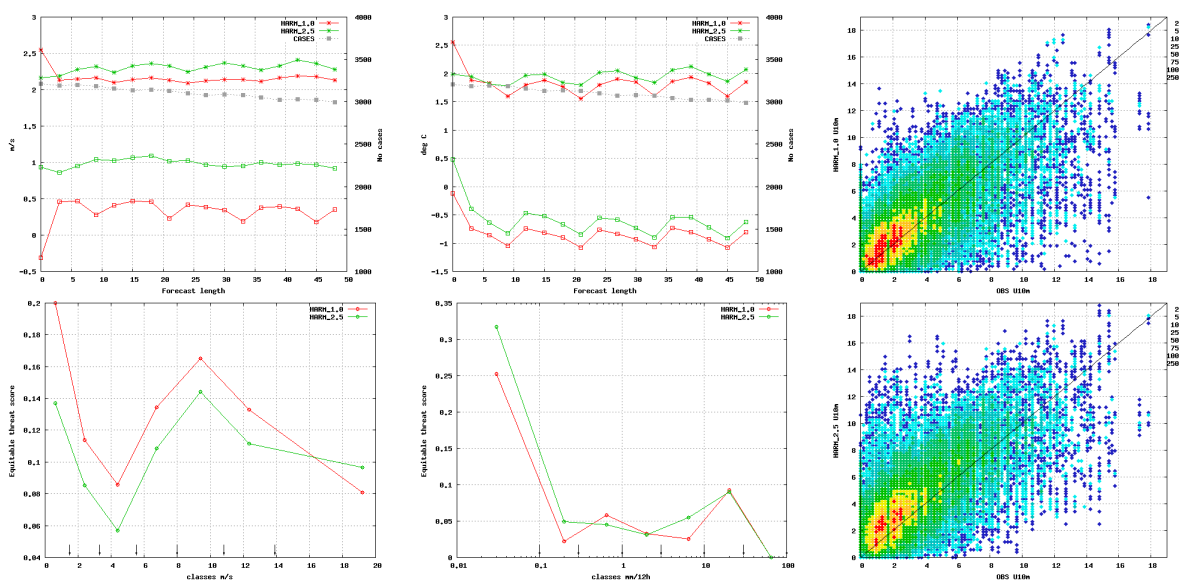


Figure 13: Canary Islands domain. Verification scores for HARM-AROME 1.0 (red) and HARM-AROME 2.5 (green). U10m (up left) and T2m (up centre). RMSE STDV (*) and bias (□). ETS U10m (down left) and ETS PE (down centre). On the right, the U10m scatterplots for 1.0 km (up) and for 2.5 km (down).

In general, the 10 m wind behaviour shows better results in autumn than in spring. This is probably due to the higher atmospheric instability at the last season. However, the improvement accomplished by the 1.0 km run in March looks bigger than in October. About the different areas, the Mediterranean Sea and Gulf of Biscay show both better results and bigger improvement than the Alboran Sea and the Canary Islands. Especially the Gulf of Biscay, whose weather is mainly dominated by Atlantic frontal situations.

About temperature, all areas have a similar RMSE STDV behaviour in October for the two resolutions, with a slight increase of the negative bias at the 1.0 km run. In March, there is a slight worsening of the verification figures for the higher resolution, being noticeable the increase of negative bias at the Mediterranean and Alboran Sea areas. Regarding the 12 hours precipitation ETS, the 1.0 and 2.5 km, results are similar for the Mediterranean Sea and Canary Islands but the 2.5 km model scores overtake the 1.0 km ones at the Alboran Sea and especially at the Gulf of Biscay.

Finally, the following figure (figure 14) shows the wind day variation 6 hours mean during March 2017. It can be observed a closer estimation of the real values with the 1.0 km configuration, reducing the 2.5 km overestimation. This is remarkable at the Gulf of Biscay and Canary Islands, where the 1.0 km forecast significantly approaches the observations mean line. During October 2017, the 1.0 km run even seems to underestimate the Canary Islands lower winds.

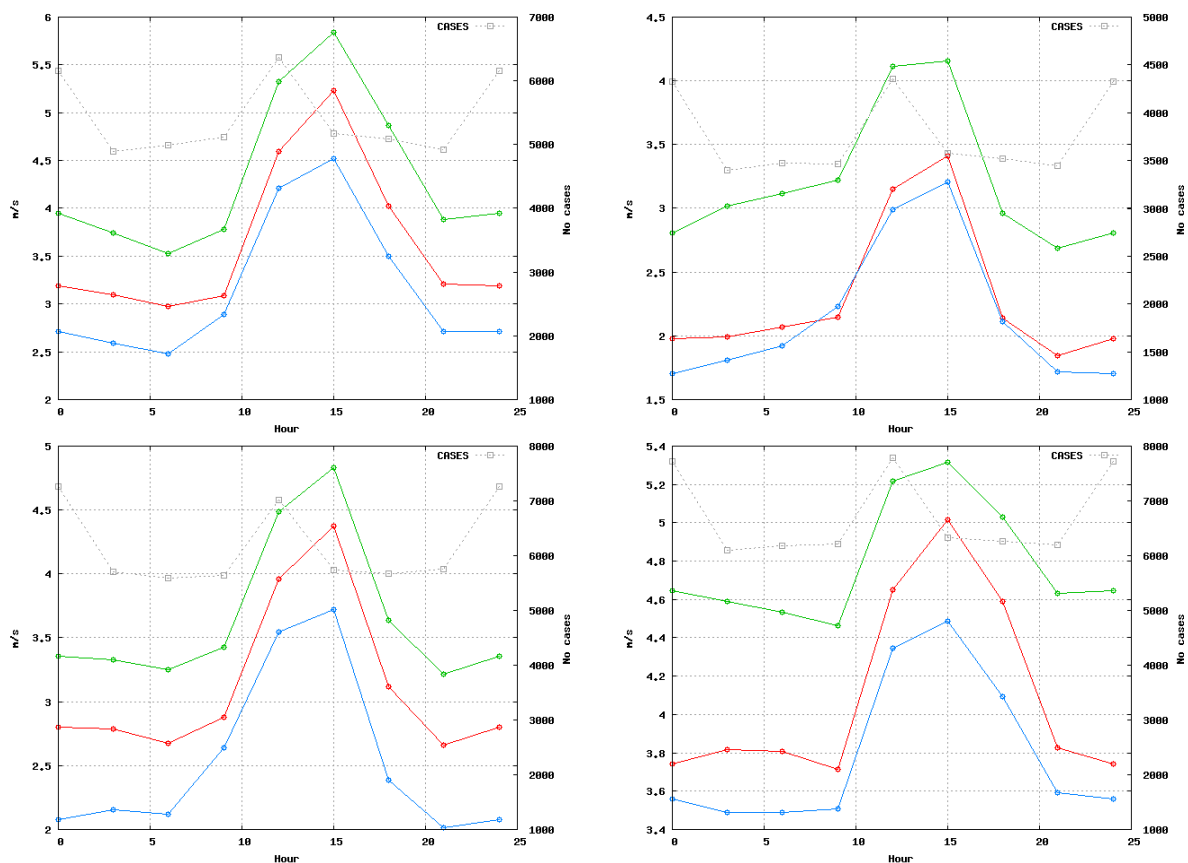


Figure 14: U10m day variation for HARM-AROME 1.0 (red), HARM-AROME 2.5 (green) and real observations (blue) at the Alboran Sea (up left), Gulf of Biscay (up right), the Mediterranean Sea (down left) and the Canary Islands (down right).

5 Conclusions

The higher resolution configuration of the HARMONIE-AROME model provides benefits like a richer and more detailed atmospheric dynamics with an important improvement of the wind forecast accuracy, which is the main goal of the SAMOA project. The results for the other variables are quite similar for the two model resolutions considered except temperature, which shows a slight worsening of the verification scores at certain situations. On the other hand, the 12 hours precipitation also seems to deteriorate however, this should be checked with more adequate verification methods for this special type of variable.

It is remarkable the different model behaviour depending on the area. Not just due to the different area shape and dimensions but also due to the different orography and dynamics. The Semi-lagrangian Horizontal Diffusion was the chosen option to try to better represent orographic turbulence but the Sub-grid Scale Orography modelling is also under consideration. Further studies will include the use of different types of grid or will start with the data assimilation work.

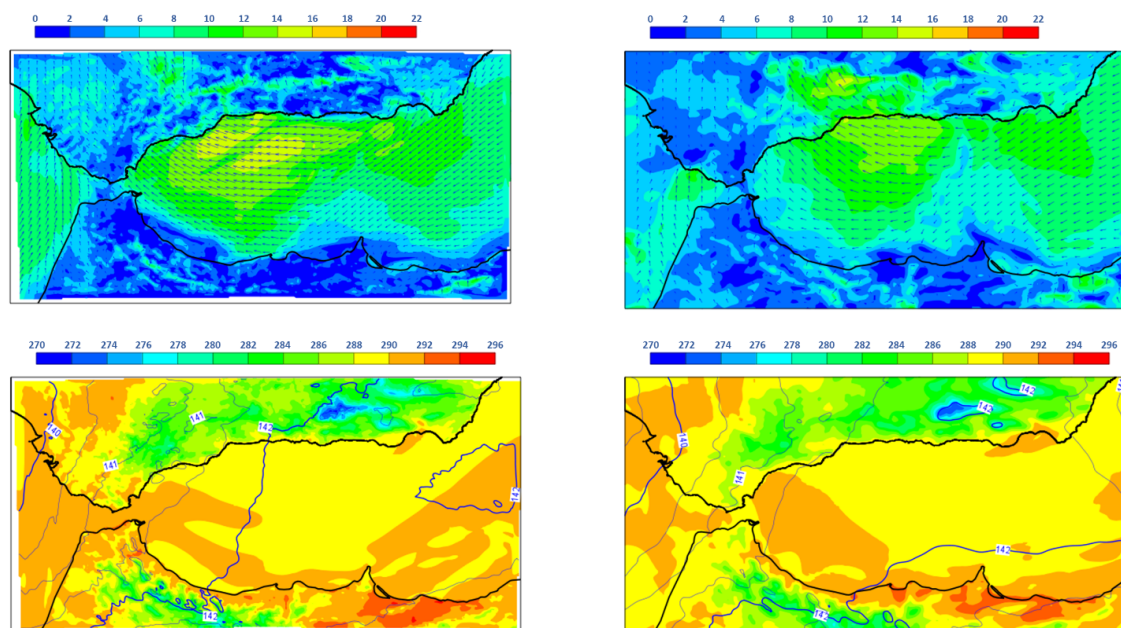


Figure 15: Alboran Sea domain. U10m direction and intensity for the 2016120312+12 (up) and 850 hPa geopotential and T2m for the 2016120312+24 (down). On the left the 1.0 km model and on the right the 2.5 km one.

6 Acknowledgements

It is compulsory for us to thank the help received from Karl Fortelius, providing us the first indications for reaching model stability, Filip Vana, for his suggestion of using the SLHD to improve the Alboran Sea verification scores, and, of course, thanks to the AEMET NWP Department for their help and support.

7 References

- Bengtsson L., Andrae U., Aspelien T., Batrak Y., Calvo J., de Rooy W. C., Gleeson E., Hansen-Sass B., Homleid M., Hortal M., Ivarsson K., Lenderink G., Niemelä S., Nielsen K. P., Onvleed J., Rontu L., Samuelsson P., Santos Muñoz D., Subias A., Tijn S., Toll V., Yang X., Ødegaard Køltzowb M. (2017). *The HARMONIE-AROME Model Configuration in ALADIN-HIRLAM NWP System*. Monthly Weather Review, vol. 145, pp. 1919-1935.
- Brousseau P., Berre L., Bouttier F., Desroziers G. (2011). *Background-error covariances for a convective-scale data-assimilation system: AROME-France 3D-Var*. Quarterly Journal of the Royal Meteorological Society, vol. 137, pp. 409-422.
- Danielson J., Gesch D. (2011). *Global Multi-resolution Terrain Elevation Data 2010 (GMTED2010)*. U.S. Geological Survey Technical Report, Open-File Report 2011-1073, 26 pp.

De Rooy W. C. (2014). *The fog above sea problem: Part I analysis*. ALADIN-HIRLAM Newsletter, No. 2, pp. 9–15.

De Rooy W. C., de Vries H. (2017). *Harmonie verification and evaluation*. HIRLAM Technical Report, No. 70.

Lauritzen P. H., Jablonowski C., Taylor M. A., Nair R. D. (2011). *Numerical Techniques for global atmospheric models*. Lecture Notes in Computational Science and Engineering, Springer, vol. 80, 556 pp.

Lenderink G., Holtslag A.A.M. (2004). *An updated length-scale formulation for turbulent mixing in clear and cloudy boundary layers*. Quarterly Journal of the Royal Meteorological Society, vol. 130, pp. 3405-3427.

O'Brien E. (2012). *Numerical stability and kinetic energy spectra in high-resolution HARMONIE*. HIRLAM Newsletter, No. 59, pp. 27-32.

Seity Y., Brousseau P., Malarden S., Hello G., Bernard P., Bouttier F., Lac C., Masson V. (2011). *The AROME-France convective-scale operational model*. Monthly Weather Review, vol. 139, pp. 976-991.

Vaná F., Bénard P., Geleyn J., Simon A., Seity Y. (2008). *Semi-Lagrangian advection scheme with controlled damping: An alternative to nonlinear horizontal diffusion in a numerical weather prediction model*. Quarterly Journal of the Royal Meteorological Society, 134, pp. 523-537.

Visibility Prediction based on AROME Cy38t1 (2.5km) Outputs using Machine-Learning Regression

Driss BARI

1 Introduction

Precise visibility estimation from the numerical weather prediction (NWP) model output are useful for air and road traffic management when visibility is reduced. For example, a dense fog event (visibility below 200 m) obliged the diversion of 21 aircrafts in 2008, which supposed to land at Mohamed V international airport (GMMN), Casablanca, Morocco, to other national airports. Such flights diversion results in considerable cost to airlines (e.g. extra fuel consumption and hotel accommodation for the passengers). However, generating accurate visibility forecasts from the NWP models remains a challenge, especially its spatial coverage, due to the complex interaction between the physical processes during the life cycle of such low visibility conditions.

As an alternative, Data mining is emerging as a suitable method for extracting patterns from extensive sets of heterogeneous data related to detection and prediction of meteorological phenomena. Bankert and Hadjimichael (2014) have demonstrated of the usefulness of data-mining methods in developing cloud-ceiling forecast algorithms from NWP model output. Other research studies have focused on visibility forecasting using data mining methods at single station, particularly at airports (Bartokova et al., 2015; Bari and EL Khelifi, 2015; Cornejo-Bueno et al., 2017).

The main objective of this study is to evaluate the potential of Data Mining methods in estimating the 2m-visibility from the operational NWP model AROME outputs. This study takes part from the Moroccan Data mining meteorological project undertaken by Maroc Météo which aims to develop many tools for helping forecasters in decision making. The first phase of this project has focused on fog and low clouds detection and estimation of visibility and cloud ceiling height from a combination of conventional meteorological observations from synoptic stations and MSG satellite data (Bari and Lemkhenter, 2017).

2 Data and Methods

To achieve the main objective of this study, hourly forecasts from AROME (Cyc38t1, 2.5km) midnight run for some meteorological parameters in the atmospheric boundary layer and observed horizontal visibility from 37 synoptic stations, have been used. The created database covers two years from March 2015 to March 2017. The study domain covers the northern part of Morocco. This region is a fog-prone area (Bari et al. 2016) and contains many airports.

The KDD-produced algorithms consist of algorithms for estimating visibility based on regression decision trees. To develop the boosted trees, XGBoost (Extreme Gradient Boosting), which is a scalable machine learning system for tree boosting, has been used (Chen and Guestrin, 2016). In the tree ensemble methods, we are learning functions (trees) instead of learning numerical weights by additive training (boosting). To learn the set of functions used in the developed model, we minimize a regularized learning objective:

$$\text{Objective} = \text{Training Loss} + \text{Regularization}$$

Where training loss term measures how well model fit on training data and the additional regularization term measures complexity of the model and helps to smooth the final learnt weights to avoid over-fitting. This approach aims to have predictive and simple functions. In this work, XGBoost is used for supervised learning problems, where we use the training data (with multiple features) x_i to predict a target variable y_i . The training (75% of all data) and testing (25% of all data) sets have been created by a random split of all available data for all locations together.

3 Results

An estimated visibility product over the north of Morocco, from AROME Cy38t1 outputs using machine learning-regression, has been developed. The performance of the developed model has been assessed, over the continental part only, based on real data collected at 37 synoptic stations over 2 years (march 2015 – march 2017).

Results analysis points out that the performance of the developed model for estimating visibility does not depend on daytime or night-time; thus, it is sufficient to develop one model based on data covering the whole day. Besides, it is found that this model has shown a strong ability to differentiate between visibilities occurring during daytime and night-time. However, the KDD-developed model have shown low performance of generality across time. The performance evaluation indicates a bias of -9m, a mean absolute error of 1349m with 0.87 correlation and a root mean-square error of 2150m.

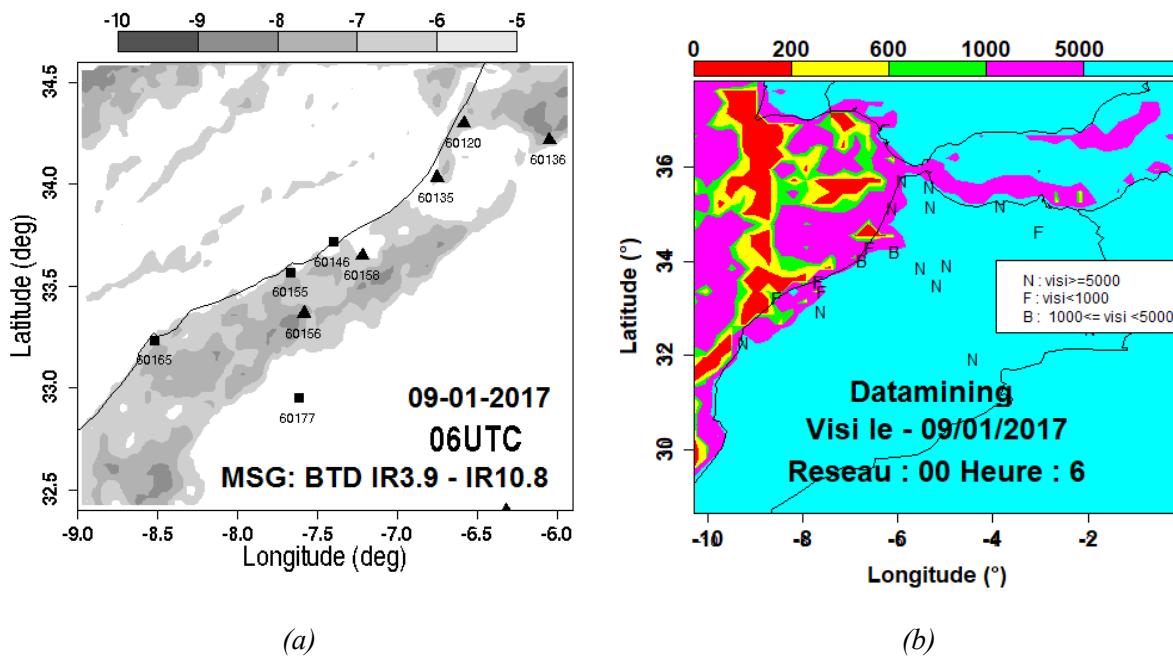


Figure. (a) Brightness temperature difference (BTD in K) images (shaded in grey scale) between the infrared channels IR3.9 and IR10.8 μm at 0600UTC on 09 January 2017. Triangles refer to airports. (b) KDD-developed model output for estimating visibility 6 hours later from run of midnight of NWP model on 09 January 2017. "F" refers to observed foggy conditions (visibility below 1km). "B" refers to observed mist (visibility between 1km and 5km). "N" refers to observed visibilities above 5km. The positions of all these symbols represents the locations of the synoptic stations.

4 References

Bankert, R. L., and Hadjimichael, M. (2007). **Data mining numerical model output for single-station cloud-ceiling forecast algorithms.** *Weather and Forecasting*, 22(5), 1123-1131.

Bari D., T. Bergot, and M. El Khlifi. (2016). **Local meteorological and large-scale weather characteristics of fog over the grand Casablanca region, Morocco.** *Journal of Applied Meteorology and Climatology*, 55(8):1731–1745.

Bari D. and M. El Khlifi. (2015). **LVP conditions at Mohamed V airport, Morocco: Local characteristics and prediction using neural networks.** *International Journal of Basic and Applied Sciences*, 4(4):354.

Bari D. and A. Lemkhenter. (2017). **Remote-Ground based observations Merging Method for Visibility and Cloud Ceiling Assessment During the Night Using Data-Mining Algorithms.** In *Proceeding of Aeronautical Meteorology Scientific Conference (AeroMetSci-2017, AeM SERIES No. 2)*, Toulouse, France, 6-10 november 2017. p128-133

Bartoková, I., Bott, A., Bartok, J., and Gera, M. (2015). **Fog prediction for road traffic safety in a coastal desert region: Improvement of nowcasting skills by the machine-learning approach.** *Boundary-layer meteorology*, 157(3), 501-516.

Chen T. and C. Guestrin. (2016). **Xgboost: A scalable tree boosting system.** In *Proceedings of the 22nd ACM SIGKDD International Conference on Knowledge Discovery and Data Mining*, pages 785–794.

Cornejo-Bueno, L., Casanova-Mateo, C., Sanz-Justo, J., Cerro-Prada, E., and Salcedo-Sanz, S. (2017). **Efficient Prediction of Low-Visibility Events at Airports Using Machine-Learning Regression.** *Boundary-Layer Meteorology*, 165(2), 349-370.

Background-error covariances for AROME-Morocco 3D-Var

Fatima Zahra HDIDOU

1. Introduction

AROME-Morocco is a convective-scale numerical weather system which has been running with data assimilation since the end of 2016. A 3D-Var assimilation scheme is used with 3h cycling. The horizontal and vertical resolutions of AROME-Morocco are 2.5km and 90 levels respectively. The variational methods require the knowledge of the uncertainty of both sources of information; the observations and model. Thus, the background error covariances, which represent the difference between the background state and the true atmospheric state, must be determined. This article deals with the computation of the background error covariances for AROME Morocco model.

2. Computation of background-error covariances for AROME Morocco

Background error covariances for AROME-Morocco are computed using an ensemble assimilation based method (Fischer, 2003). The principle of this approach is that the dispersion error of an ensemble data assimilation system can be a good approximation of the real background error (Desroziers et al, 2008). The main benefit of this method compared to the former ones (e.g. NMC) is the ability to simulate the analysis effect in the error evolution (Berre et al, 2006).

The first background error covariances for AROME-Morocco were computed using an AROME forecast ensemble coupled to ARPEGE ensemble in spin-up mode (EXP_SU) over a period of 10 days (from 16 to 25 August 2016) twice a day (00 and 12UTC). Those first background error covariances were used to run AROME-Morocco ensemble assimilation (EXP_EDA). The EXP_EDA is an ensemble variational assimilation based on an ensemble of perturbed AROME 3D-Var analysis and took its own LBCs from the ARPEGE ensemble assimilation. The EXP_EDA was run over the same period as EXP_SU. The background error covariances for AROME-Morocco were computed using differences between pairs of 3h range EXP_EDA forecasts from the six members twice a day (00 and 12 UTC).

3. Background error covariances diagnostics

To compare background error covariances computed using both EXP_SU and EXP_EDA, several diagnostics are studied. Figure 1 shows the vertical correlations of specific humidity and vorticity forecast errors; it represents the correlations of each level of the model of a given parameter with all other levels of the same parameter. High values are found on the diagonal (correlation of a level with itself), and we note also that, for all parameters, the vertical correlations for the low levels layers are more pronounced than in the higher levels. The vertical correlations for EXP_EDA are sharper than EXP_SU.

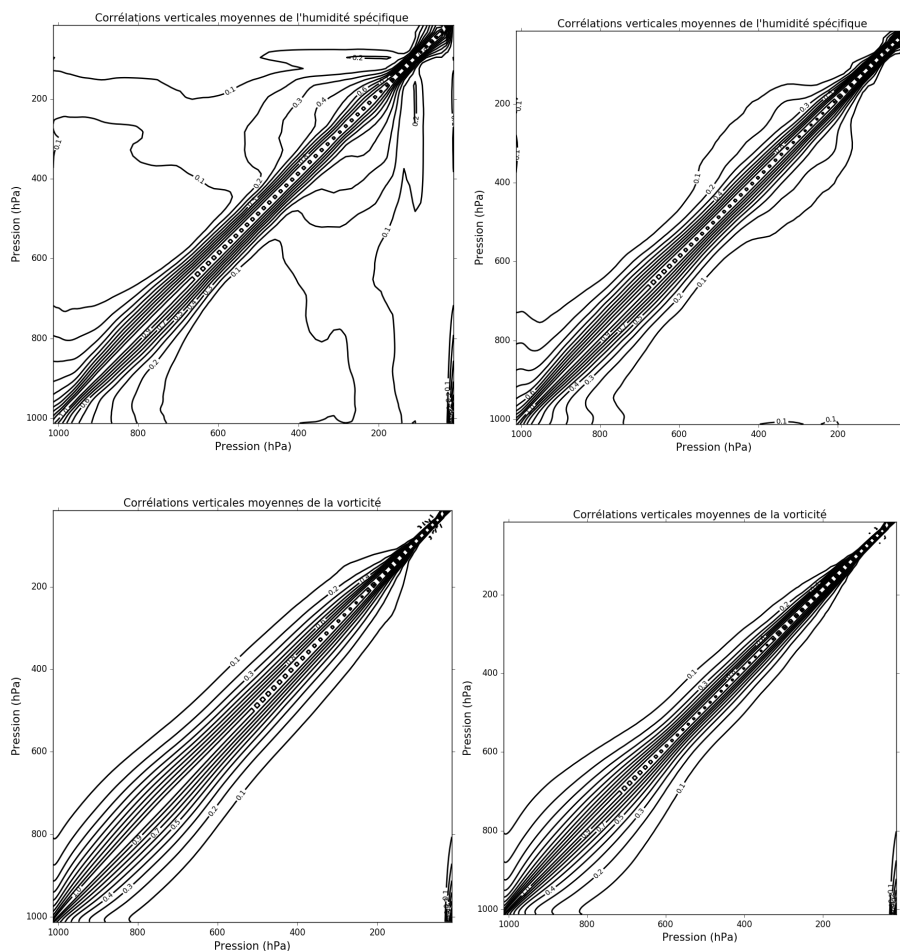


Figure. Vertical correlations of specific humidity (upper panels) and vorticity (lower panels) forecast errors for EXP_SU (left panels) and EXP_EDA (right panels).

4. Conclusion

This study concerns the computation of background error covariances for AROME Morocco using the ensemble assimilation technique. Those covariances are compared with ones computed using a spin-up method. The comparison of several diagnosis (not shown) shows that statistics computed with EXP_EDA represent better the small scale features than EXP_SU. This is a first attempt to compute background error statistics for AROME-Morocco, the next step will be the computation of this statistics over longer period in both summer and winter.

5. References

Berre, L., S.E., Stefanescu, and M. Belo Pereira, 2006: **The representation of the analysis effect in three error simulation techniques**. Tellus, 58A, 196-209.

Gérald Desroziers, Loïc Berre, Olivier Pannekoucke, Simona Ștefanescu, Pierre Brousseau, Ludovic Auger, Bernad Chapnik, and Laure Raynaud. **Flow-dependent error covariances from variational assimilation ensembles on global and regional domains**. Hirlam Technical ReportY, 2008.

Fischer M. 2003. **Background-error covariance modeling**. In ECMWF Seminar on recent Developments in Data Assimilation for Atmosphere and Ocean. ECMWF: Reading, UK, pp 45-63.

IGB, the Upgrade to the Joint Operational HARMONIE by DMI and IMO in 2018

Xiaohua Yang¹, Bolli Palmason², Kai Sattler¹, Sigurdur Thorsteinsson², Bjarne Amstrup¹, Mats Dahlbom¹, Bent Hansen Sass¹, Kristian Pagn Nielsen¹, Guðrún Nína Petersen²

1. Danish Meteorological Institute
2. Icelandic Met Office

1. Introduction

In March 2018, Danish Meteorological Institute (DMI) and the Icelandic Met Office (IMO) jointly launches new operational suite, Harmonie-IGB (Iceland Greenland domain B), for high resolution short range weather forecast of Iceland-Greenland areas. IGB is an upgrade to the existing operational model IGA (Iceland Greenland domain A) launched in Dec 2016. IGB is run on a horizontal mesh of 1280x1080 points, with grid distance at 2.5 km and 65 levels in the vertical. In terms of domain coverage, IGB is 72% larger than IGA (Figure 1), providing an unprecedented forecast capability with very high resolution for an extensive geographic area in the Arctic region. Extension of the Harmonie model domain for the area also enables complete outphasing of the operational Hirlam-K05 for routine Greenland weather forecast.

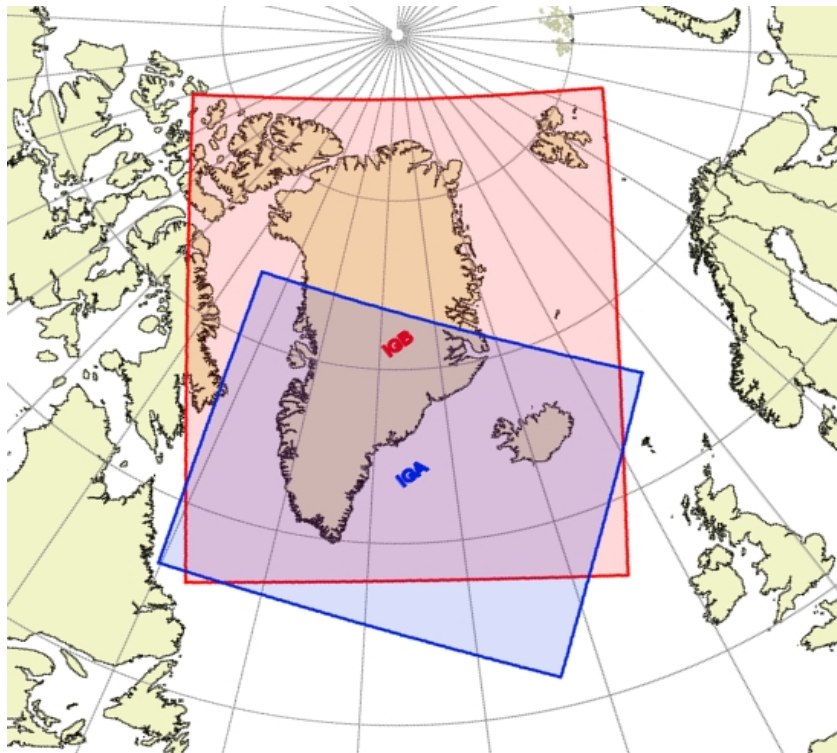


Figure 1. Domain coverage of the new operational HARMONIE-IGB (in red) in comparison to the previous operational one IGA (in blue). IGB runs with 3-hourly 3D-VAR assimilation and makes 66h forecast every 6 hours at 00, 06, 12 and 18 UTC.

Besides a significant domain expansion, another significant feature in this upgrade is the application of upper air data assimilation with 3D-VAR method, in which satellite remote sensing data from microwave radiance (brightness temperature), atmospheric motion vector (AMV wind), radio occultation data (RO bending angle) as well as conventional observations from radio sonde, aircraft, and surface observations over land stations, ship and drift buoys, are assimilated. This also marks the first time that advanced data assimilation scheme is used in high resolution Harmonie model for the observation sparse area of Greenland and Iceland, taking advantage of an improved capability with Harmonie system to utilise remote sensing data in addition to the in-situ observation network. For lateral boundary, ECMWF 9 km HRES forecast is used, latter also includes analysis of sea surface temperature and ice fraction within the model domain.

2. Model configurations

Systemwise the operational Harmonie-IGB is built upon a special Subversion code branch IGB40H11, which is a modification to the code branch behind the operational IGA, IGA40H11. The latter is in turn adapted from the reference HARMONIE-40h1.1 with a number of deviations in configuration as detailed in Yang et al (2017). For IGB, a cubic grid has been selected for benefit of an improved stability and computational efficiency. IGB runs with a time stepping of 75 seconds.

IGB assimilates observation at 3-hourly interval, with a half hour observation data cutoff, targeting to track most recent weather at local scales. The background error structure function has been derived using Ensemble of Data Assimilation (EDA) runs with statistics computed using differences between ensemble forecasts with 6h lead-time. A 66-hour forecast is made every 6 hours at the synoptic times of 00, 06, 12 and 18 UTC, delivered within 2h after nominal analysis times. The forecast output data stream remains same as in IGA.

3. Operationalisation and forecast performance

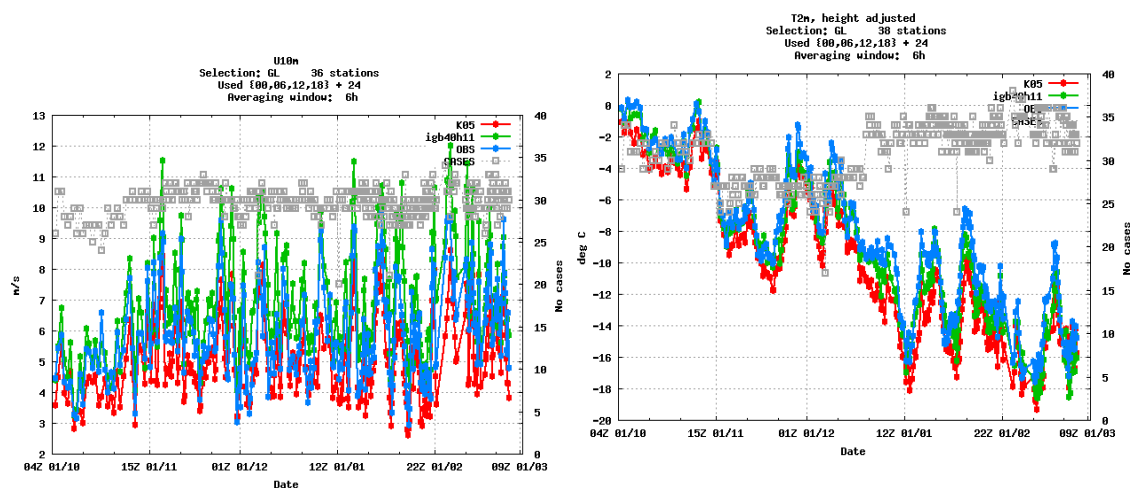


Figure 2: 24-h forecasted time series of surface wind speed (at 10m) and temperature (at 2 m) during Oct 2017 and Feb 2018 with Harmonie-IGB (in green), Hirlam-K05 (in red) as compared to verifying observation (in blue), averaged over 38 Greenland surface stations.

Real time IGB40H11 with 3D-VAR started on Jan 16 2017, thus with a year-long period of parallel run prior to operationalisation. The setup had gone through extensive tests, with monitoring and tuning during the period up to final operationalisation. As illustration of forecast quality, Figure 2

shows the averaged forecast time series of surface wind and temperature for Greenland stations during the latest winter period, including numerous windy episodes. As has been observed in previous high resolution versions of Harmonie, IGB, due to a higher resolution, is able to detect stronger wind events than with Hirlam K05. For temperature, IGB also shows a better fit to observation than K05, which appears to suffer stronger negative bias.

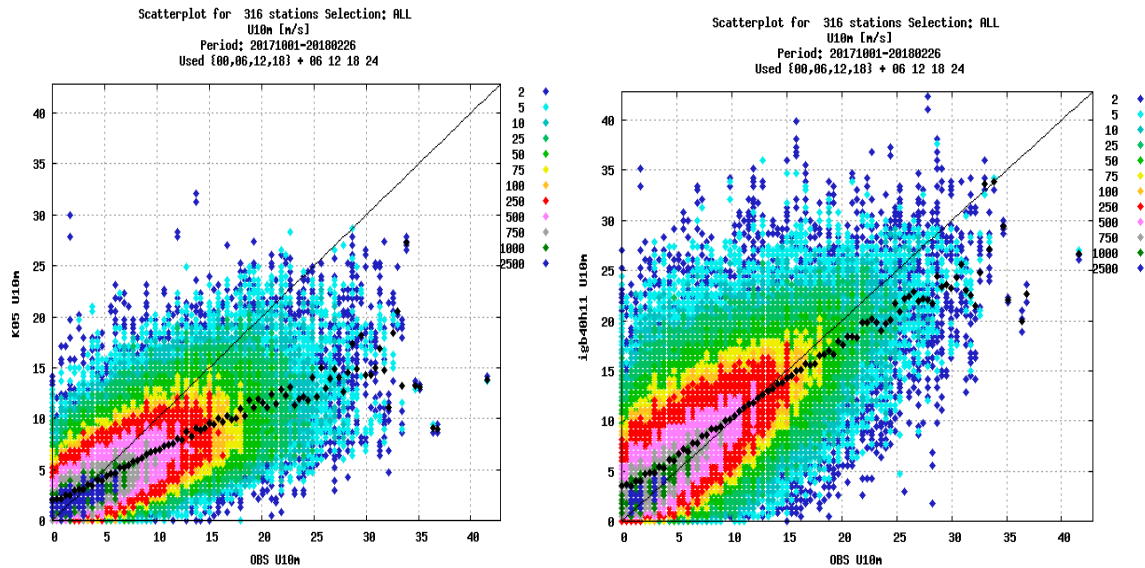


Figure 3: Scatterplot showing short range forecast of wind speed (y-axis) for Greenland and Iceland by Hirlam-K05 (left) vs Harmonie-IGB (right) in comparison to observed 10-m wind (x axis) during Oct 2017 and Feb 2018. Colors indicate size of samples. The comparison show that, while K05 often fail to forecast storm conditions (> 24.5 m/s), IGB is better able to forecast.

From verification statistics, precipitation forecast from IGB outperform also those of K05 for the area of Greenland and Iceland when compared to rain gauge measurement data.

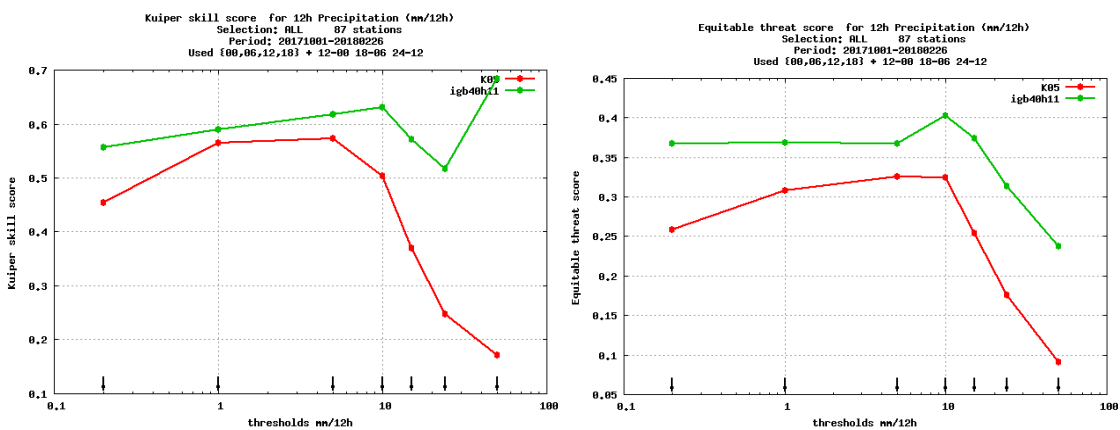


Figure 4: Observation verification with Kuiper Skill Score (left) and Equitable threat score (right) of 12-h accumulated precipitation for Greenland and Iceland stations comparing short range forecast from Hirlam-K05 (red) and Harmonie-IGB (green) for the latest winter period during Oct 2017 and Feb 2018, with observation data binned in thresh-hold from small to higher amount. The comparison indicate a generally high forecast skill by IGB for precipitation.

As an improvement to IGA, 3DVAR, a more advanced assimilation method utilising remote sensing data as well as traditional in-situ observation, are performed in IGB, with an improved potential to reflect weather reality, especially to adjust better to evolution of weather in rapid developing situations. From verification monitoring it has been found that, at same resolution, IGB maintains similar forecast quality as that of IGA for same verification area, and for screen level temperature, it tends to outperform IGA especially in bias behaviour, presumably thanks to a more frequent assimilation for synoptic data (every 3 h) in IGB than in IGA (every 6h).

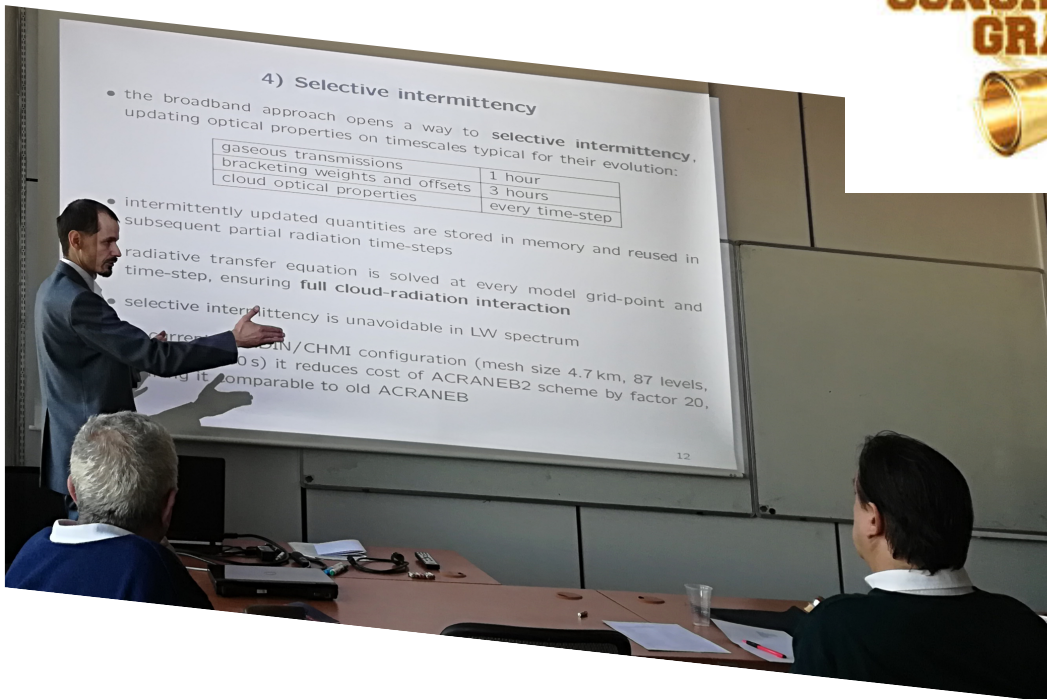
4. Near future outlook

In comparison to other areas in the world, arctic region, despite of its importance to global climate, is characterised with rather sparse observation network. Data assimilation in NWP has been a weak point, affecting the overall skill for the forecast system to track evolution of weather development in a timely manner. With IGB, Harmonie forecast system starts to assimilate remote sensing data with 3DVAR method, proving a much improved potential for forecasting of rapidly developing weather system. Much work still remain to improve data assimilation and use of remote sensing data from instruments onboard polar satellites. For Harmonie model, simulation of glacier ice has a huge potential for improvement, especially in connection with simulation of surface mass balance during melting seasons. To improve modelling of surface process over permafrost area, active dialogue has also been ongoing to enable collection and use of regular measurement data from the climate monitoring mission such as PROMICE network as maintained by the GEUS in Denmark. Efforts along these fronts will lead further improvement of Harmonie forecast in the coming years.

Greenland and Iceland experiences frequently storms especially during winter half year, with storms hitting parts of Greenland and Iceland often on weekly, sometimes even daily basis, many of which associated with acceleration due to orographic forcing. With the Harmonie model at 2.5 km grid resolution, the ability in storm detection and warning has been significantly improved. However, operational experiences have also revealed many cases of over-prediction for storm conditions, most likely associated with limitation in grid resolution. The tendency for such overprediction is more pronounced in some coastal sites with complex orography such as Tasiilaq, Nanortalic, Nuuk etc. , in which strongly varying flow patterns with rather small scales have been observed. E.g., for Tasiilaq, an important coastal town in east Greenland, while storms and hurricanes often hit the nearby area in connection with low pressure and cold air outbreak from Greenland high plateau, these do not hit directly that often the town, which sits on a well shielded lee side in most situations. As such type of local variability is strongly associated with orographic features of small scales, a grid resolution of 2.5 km as used in IGA and IGB tends to predict storms too often and too strong. Obviously, a further improvement in Harmonie model resolution would be desirable, although such poses strong requirement on computational capacity. For the near future, to meet the forecast needs with complex flow, a complementary setup with “harmonie-lite” has been proposed (Yang 2018), in which sub-km grid size Harmonie models can be run on a relatively small domain for selected regions with known complex in storm conditions. It is planned that in the near future that some of these setup will be launched for operational use for populated areas with frequent storms, whereas for those with less frequent ones, on-demand use can be considered.

References

- Yang, X., Palmason, B., Andersen, B. S., Hansen Sass, B., Amstrup, B., Dahlbom, M., Petersen, C., Pagh Nielsen, K., Mottram, R., Woetmann, N., Mahura, A. Thorsteinsson, S., Nawri, N., and Petersen, G. N.2017: IGA, the Joint Operational HARMONIE by DMI and IMO, ALADIN-HIRLAM Newsletter, No. 8, 87–94, 2017.
- Yang, X., 2018: Sub-km Harmonie and On-demand setup for storm forecast. ALADIN-HIRLAM Newsletter, No 10, 35-40, 2018.



13 December 2017

Jan MASEK

Charles University of Prague, Czech Rep.

22 March 2018

Julie BERCKMANS

University of Antwerp, Belgium



More information on the previous ALADIN PhDs on the aladin website :
<http://www.cnrm-game-meteo.fr/aladin/spip.php?article88>

Modelling land-atmosphere interactions: Impact of near future land use and climate change over Western Europe

Julie Berckmans, University of Antwerp, Faculty of Sciences
Promotors: Prof. dr. Reinhart Ceulemans and dr. Rafiq Hamdi

Summary

Climate models simulate interactions between different drivers of the climate. One of them is the land surface which has been documented to have a vast influence on the regional climate. However, this driver and its influence on the climate is usually not well represented by the current regional climate models. The objective of this doctoral thesis is to demonstrate the importance of modelling **interactions between the land surface and the atmosphere** in Western Europe. This is relevant to reduce the uncertainty of a climate change projection. This in its turn is relevant for policy makers to develop adaptation and mitigation strategies to protect humans and their environment for climate change.

In this doctoral thesis two models have been coupled and applied for validation and projection purposes. The model that represented the atmosphere component is **ALARO-0**. This model is initially used at the Royal Meteorological Institute of Belgium for providing the weather forecasts. Since recently, this model is also used for regional climate modelling. The model that represented the land surface component within this thesis is **SURFEXv5**. This model is a result of combining schemes for distinct land surfaces such as urban and natural. The coupling of both models has already been done for numerical weather prediction applications and has illustrated a good performance. A similar setup was applied in this thesis for regional climate modelling.

The purpose of this doctoral thesis was twofold. Firstly, we validated the regional climate model ALARO coupled to SURFEX for the simulation of land-atmosphere interactions by (i) testing the added value of SURFEX, (ii) testing different initial conditions, (iii) illustrating the performance of the model for water vapour, and (iv) investigating the urban scale. Secondly, we applied ALARO-SURFEX for climate change projections for the next few decades (i.e. near future) under scenarios of greenhouse gas emissions and land surface changes. A specific feature of SURFEX is the representation of the land surface as a patchwork of natural, impervious and water surfaces. This is called the tiling approach. This is beneficial for the simulation of processes that occur at a scale smaller than the grid size of the model. Especially in Western Europe the land surface is composed of large heterogeneities.

The first part of the thesis focused on the validation of ALARO-SURFEX. The input for the model at regional scale came from a reanalysis that assimilates observations at the global scale. The method for using the information at global scale to drive a regional climate model is called downscaling. More specifically, the method applied is dynamical downscaling as we preserve the physical laws of the model. We presented the **added value of using SURFEX** with respect to the initial setup of the atmosphere model with a simple representation of the land surface. Both minimum and maximum temperatures in summer showed an improvement when using SURFEX, while precipitation was not very sensitive to the choice of the land surface modelling. These results contributed to the hypothesis that the detailed land surface representation in SURFEX has improved the performance of ALARO-0.

Now that the coupled model ALARO-SURFEX showed a good performance for the climate of Western Europe, it was of interest to select the best method for performing the simulations. This method should be carefully chosen to use the full potential of the improved land surface representation and related land-atmosphere interactions. We studied this by updating the **initial conditions** of the model with different frequencies. This process was done during the downscaling. The common method of downscaling is one with the initialisation at the start of the simulation for both the atmosphere and the land surface conditions. We compared this method with two alternative methods: (i) the initialisation at each day for both the atmosphere and the land surface, and (ii) the initialisation at each day for the atmosphere, but only once at the start of the simulation for the land surface. The two alternative simulations demonstrated a better performance of the model for temperature and precipitation in comparison to observations than the common method. The last method allowed for a full interaction between the land surface and the atmosphere.

Climate change projections usually focus on the change in temperature and precipitation. However, the atmospheric **water vapour** plays a key role in the feedback process of a changing climate. Therefore, a good simulation of the water vapour by climate models is crucial. The water vapour was well represented by the model on a yearly and seasonal basis, except for summer when it was too dry. This could be explained by the cold temperature bias of the model that resulted in a too low evaporation rate in summer. This phenomenon was less dominant in the other seasons, as the coupling between the temperature and the water vapour is strongest in summer. These results confirmed that the model well represented the interaction between the land and the atmosphere.

The land surface of Western Europe is covered with large urban surfaces that show distinct characteristics than natural surfaces. Fortunately, SURFEX has been developed with the detailed scheme for the **urban scale**. Furthermore, SURFEX could be used separately at a high resolution of 1 km without the coupling to the atmosphere model. Only the atmospheric parameters were used as input to drive SURFEX at a high resolution. This state of the art simulation illustrated an enhancement of the Urban Heat Island (UHI) during heat waves for Brussels. Although 1 km horizontal resolution was too coarse in terms of the urban microscale features, it was able to correctly simulate the nocturnal UHI in the city of Ghent. We concluded that the urban scheme within SURFEX was able to realistically represent the climate on the urban scale of Belgian cities.

The second part of this doctoral thesis focused on the use of ALARO-SURFEX for climate change projections under two scenarios of greenhouse gas emissions and one scenario of land use changes. The scenarios for **greenhouse gas emissions** were developed during the Fifth Assessment Report of the Intergovernmental Panel on Climate Change (IPCC) and are called Representative Concentration Pathways (RCPs). The climate change for the near future is particularly interesting for decision makers. Therefore, we investigated the changes in the mean temperature and precipitation and their extremes in the 30-yr period of 2006 to 2035 with respect to the 30-yr period of 1976 to 2005. Both temperature and precipitation were simulated to increase in the near future, though the changes were relatively small. In contrast to the mean change, the daily variability increased larger. This resulted in more extreme events such as heat waves and extreme precipitation events.

Although greenhouse gas emissions play an important role, there are other human sources for climate change. One of them is **changes to the land surface**. To study this we selected a scenario for the changes in land surface for the near future based on policy-related land use changes. The land conversions that received particular interest are already taking place in reality and will likely to continue in the future. The urbanisation effect was largest of the three selected land surface conversions in the present climate. Mainly minimum temperature was enhanced and extreme temperature because of an increase in impervious surfaces that resulted in a larger sensible heat flux. In the near future, the effect of the land surface changes on the near-surface parameters were more heterogeneous than the effect of the changes in greenhouse gas emissions. The urbanisation in Flanders was simulated to lead to a doubling of the temperature effect caused by greenhouse gas

emissions. Moreover, heat waves were longer lasting and more intense because of the urbanisation in Flanders. On the other hand, afforestation helped to reduce the maximum temperatures.

We concluded that the ALARO-SURFEX model was able to **improve the regional climate** of Western Europe due to a more detailed representation of the land surface and its related interactions with the atmosphere. The model was also **applicable for projections** of the **near future** climate changes of both temperature and precipitation. Furthermore, SURFEX was reliable for representing the **urban characteristics** of Belgian cities. This gives the model great potential for providing relevant information that can be used as forcing for **impact studies** on for example heat stress in cities.

Broadband radiation scheme fully interacting with clouds

Ján Mašek

Charles University of Prague, Faculty of Mathematics and Physics

Supervisor : Radmila Brožková

Abstract

The parameterization of radiative transfer is a part of numerical weather prediction and general circulation models that is both essential and computationally very expensive, and is therefore subject to never ending compromises between accuracy and computational cost. The present thesis offers an improvement to the existing broadband radiation scheme by revising its critical components – gaseous transmissions, cloud optical properties, and calculation of internal long wave exchanges. The accuracy of the full spectrum broadband approach is thus raised to the level required for the short range numerical weather forecast. The intermittent update of broadband gaseous transmissions is introduced as a new component, reducing computational cost while preserving the full cloud radiation interaction. The scalability of long wave computations is ensured by adopting the net exchanged rate decomposition with bracketing, improved by an intermittently applied self learning algorithm determining the interpolation weights. It has been demonstrated that under conditions of operational weather forecasting, this developed scheme is fully competitive with the mainstream approach, due to the improved error balance between the stand alone radiation scheme and the intermittency strategy.

The full thesis can be downloaded [here](#).

Previous issues of the joint ALADIN-HIRLAM NL



[No. 10. January 2018](#)



[No. 9. September 2017](#)



[No. 8. January 2017.](#)



[No. 7. September 2016](#)



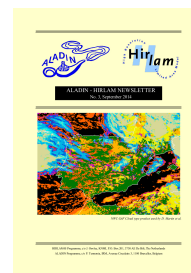
[No. 6. February 2016.](#)



[No. 5. August 2016](#)



[No. 4. February 2015](#)



[No. 3. September 2015](#)



[No. 2. April 2014](#)



[No. 1. September 2013](#)